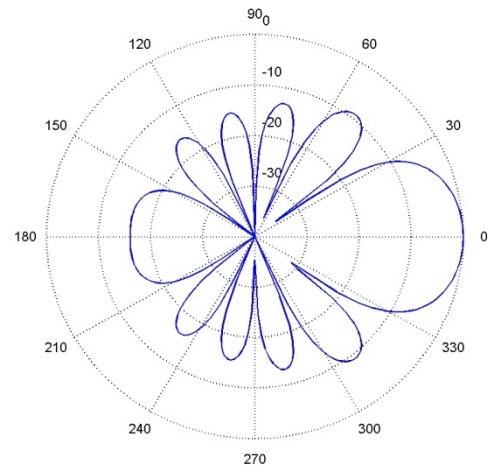
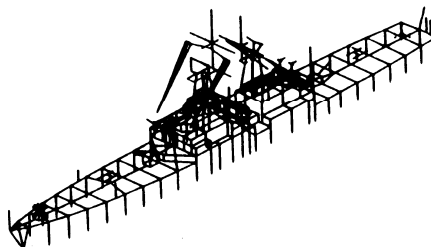
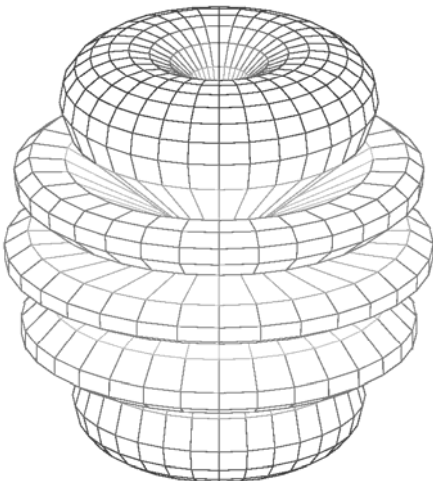
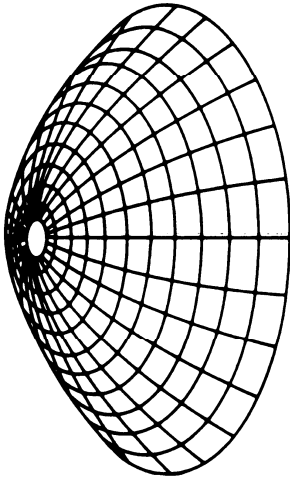
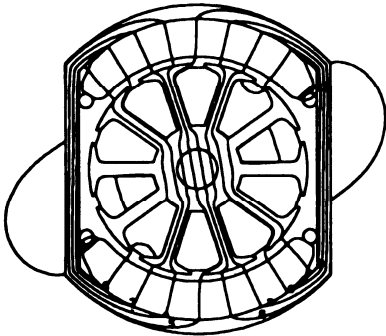
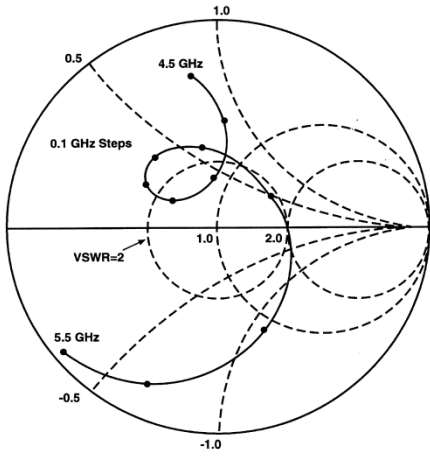


Applied Computational Electromagnetics Society Journal

Editor-in-Chief
Atef Z. Elsherbeni

September 2010
Vol. 25 No. 9
ISSN 1054-4887



GENERAL PURPOSE AND SCOPE: The Applied Computational Electromagnetics Society (*ACES*) Journal hereinafter known as the *ACES Journal* is devoted to the exchange of information in computational electromagnetics, to the advancement of the state-of-the art, and the promotion of related technical activities. A primary objective of the information exchange is the elimination of the need to “re-invent the wheel” to solve a previously-solved computational problem in electrical engineering, physics, or related fields of study. The technical activities promoted by this publication include code validation, performance analysis, and input/output standardization; code or technique optimization and error minimization; innovations in solution technique or in data input/output; identification of new applications for electromagnetics modeling codes and techniques; integration of computational electromagnetics techniques with new computer architectures; and correlation of computational parameters with physical mechanisms.

SUBMISSIONS: The *ACES Journal* welcomes original, previously unpublished papers, relating to applied computational electromagnetics. Typical papers will represent the computational electromagnetics aspects of research in electrical engineering, physics, or related disciplines. However, papers which represent research in applied computational electromagnetics itself are equally acceptable.

Manuscripts are to be submitted through the upload system of *ACES* web site <http://aces.ee.olemiss.edu> See “Information for Authors” on inside of back cover and at *ACES* web site. For additional information contact the Editor-in-Chief:

Dr. Atef Elsherbeni
Department of Electrical Engineering
The University of Mississippi
University, MS 386377 USA
Phone: 662-915-5382 Fax: 662-915-7231
Email: atef@olemiss.edu

SUBSCRIPTIONS: All members of the Applied Computational Electromagnetics Society who have paid their subscription fees are entitled to receive the *ACES Journal* with a minimum of three issues per calendar year and are entitled to download any published journal article available at <http://aces.ee.olemiss.edu>

Back issues, when available, are \$15 each. Subscriptions to *ACES* is through the web site. Orders for back issues of the *ACES Journal* and changes of addresses should be sent directly to *ACES*:

Dr. Allen W. Glisson
302 Anderson Hall
Dept. of Electrical Engineering
Fax: 662-915-7231
Email: aglisson@olemiss.edu

Allow four week’s advance notice for change of address. Claims for missing issues will not be honored because of insufficient notice or address change or loss in mail unless the Executive Officer is notified within 60 days for USA and Canadian subscribers or 90 days for subscribers in other countries, from the last day of the month of publication. For information regarding reprints of individual papers or other materials, see “Information for Authors”.

LIABILITY. Neither *ACES*, nor the *ACES Journal* editors, are responsible for any consequence of misinformation or claims, express or implied, in any published material in an *ACES Journal* issue. This also applies to advertising, for which only camera-ready copies are accepted. Authors are responsible for information contained in their papers. If any material submitted for publication includes material which has already been published elsewhere, it is the author’s responsibility to obtain written permission to reproduce such material.

APPLIED COMPUTATIONAL ELECTROMAGNETICS SOCIETY JOURNAL

Editor-in-Chief
Atef Z. Elsherbeni

September 2010
Vol. 25 No. 9
ISSN 1054-4887

The ACES Journal is abstracted in INSPEC, in Engineering Index, DTIC, Science Citation Index Expanded, the Research Alert, and to Current Contents/Engineering, Computing & Technology.

The first, fourth, and sixth illustrations on the front cover have been obtained from the Department of Electrical Engineering at the University of Mississippi.

The third and fifth illustrations on the front cover have been obtained from Lawrence Livermore National Laboratory.

The second illustration on the front cover has been obtained from FLUX2D software, CEDRAT S.S. France, MAGSOFT Corporation, New York.

THE APPLIED COMPUTATIONAL ELECTROMAGNETICS SOCIETY

<http://aces.ee.olemiss.edu>

ACES JOURNAL EDITOR-IN-CHIEF

Atef Elsherbeni

University of Mississippi, EE Dept.
University, MS 38677, USA

ACES JOURNAL ASSOCIATE EDITORS-IN-CHIEF

Sami Barmada

University of Pisa, EE Dept.
Pisa, Italy, 56126

Fan Yang

University of Mississippi, EE Dept.
University, MS 38677, USA

Mohamed Bakr

McMaster University, ECE Dept.
Hamilton, ON, L8S 4K1, Canada

ACES JOURNAL EDITORIAL ASSISTANTS

Matthew J. Inman

University of Mississippi, EE Dept.
University, MS 38677, USA

Mohamed Al Sharkawy

Arab Academy for Science and
Technology, ECE Dept.
Alexandria, Egypt

Christina Bonnington

University of Mississippi, EE Dept.
University, MS 38677, USA

Khaled ElMaghoub

University of Mississippi, EE Dept.
University, MS 38677, USA

Anne Graham

University of Mississippi, EE Dept.
University, MS 38677, USA

ACES JOURNAL EMERITUS EDITORS-IN-CHIEF

Duncan C. Baker

EE Dept. U. of Pretoria
0002 Pretoria, South Africa

Allen Glisson

University of Mississippi, EE Dept.
University, MS 38677, USA

David E. Stein

USAF Scientific Advisory Board
Washington, DC 20330, USA

Robert M. Bevensee

Box 812
Alamo, CA 94507-0516, USA

Ahmed Kishk

University of Mississippi, EE Dept.
University, MS 38677, USA

ACES JOURNAL EMERITUS ASSOCIATE EDITORS-IN-CHIEF

Alexander Yakovlev

University of Mississippi, EE Dept.
University, MS 38677, USA

Erdem Topsakal

Mississippi State University, EE Dept.
Mississippi State, MS 39762, USA

SEPTEMBER 2010 REVIEWERS

Iftikhar Ahmed

Rajeev Bansal

Sami Barmada

Felipe Catedra

Gerald DeJean

Yiming Deng

Alistar Duffy

Khaled El Mahgoub

Todd Hubing

Amalia Ivanyi

Darko Kajfez

Nikolaos Kantartzis

Fadi Khalil

Fernando Las-Heras

Francisco Medina

Krzysztof Michalski

Antonio Orlandi

Andrew Peterson

Dr. Pichon

C. J. Reddy

Luca Rienzo

Vince Rodriguez

Hal Sabbagh

Binay Sarkar

Zhenfei Song

Alan Taflove

Alexander Yakovlev

Fan Yang

Huapeng Zhao

THE APPLIED COMPUTATIONAL ELECTROMAGNETICS SOCIETY
JOURNAL

Vol. 25 No. 9

September 2010

TABLE OF CONTENTS

“The Joy of Computing with Volume Integrals: Foundations for Nondestructive Evaluation of Planar Layered Media”
H. A. Sabbagh, R. K. Murphy, E. H. Sabbagh, J. C. Aldrin, J. S. Knopp, and M. P. Blodgett.....723

“The Joy of Computing with Volume Integrals: Validation and Performance Comparison”
H. A. Sabbagh, R. K. Murphy, E. H. Sabbagh, J. C. Aldrin, J. S. Knopp, and M. P. Blodgett.....731

“Stable Partial Inductance Calculation for Partial Element Equivalent Circuit Modeling”
Z. Song, F. Duval, D. Su, and A. Louis.....738

“Complex Incomplete Cholesky Factorization Preconditioned Bi-conjugate Gradient Method”
Y. J. Zhang and Q. Sun.....750

“Efficient Analysis Technique for Modeling Periodic Structures Based on Finite Element Method using High-Order Multiscale Functions”
A. B. Ali, E. A. Hajlaoui, and A. Gharsallah.....755

“Equivalent Circuits for Nonuniform Transmission Line Simulation”
J. Izydorczyk.....764

“High-Isolation and Low-Loss RF MEMS Shunt Switches”
H. Jaafar, O. Sidek, A. Miskam, and R. Abdul-Rahman.....780

“A New UWB Slot Antenna with Rejection of WiMax and WLAN Bands”
J. William and R. Nakkeeran.....787

“Microstrip Inductor Design and Implementation”
A. Eroglu.....794

“Analysis of Dual-Mode Microstrip Patch Filter using Multiscale Wave Concept Iterative Process”
T. I. E. Brahim, H. Zairi, A. Gharsallah, A. Gharbi, and H. Baudrand.....801

The Joy of Computing with Volume Integrals: Foundations for Nondestructive Evaluation of Planar Layered Media

Harold A. Sabbagh¹, R. Kim Murphy¹, Elias H. Sabbagh¹,
John C. Aldrin², Jeremy S. Knopp³, and Mark P. Blodgett³

¹ Victor Technologies LLC
Bloomington, IN 47401, USA
has@sabbagh.com, kimmurphy1@aristotle.net, ehs@sabbagh.com,

² Computational Tools
Gurnee, IL 60031, USA
aldrin@computationaltools.com,

³ Air Force Research Laboratory (AFRL/RXLP)
Wright-Patterson AFB, OH 45433, USA
jeremy.knopp@wpafb.af.mil, mark.blodgett@wpafb.af.mil

Abstract — As an alternative to the finite-difference time-domain (FDTD), the finite-element method (FEM), and the method of moments (MoM) based on the surface integral equation (SIE), a volume-integral equation (VIE) approach using the method of moments and conjugate-gradient methods is presented to address a wide variety of complex problems in computational electromagnetics. A formulation of the volume integral method is presented to efficiently address inhomogeneous regions in multi-layered media. Since volume element discretization is limited to local inhomogeneous regions, numerical solutions for many complex problems can be achieved more efficiently than FDTD, FEM, and MoM/SIE. This is the first of a series of papers dealing with volume-integral equations; in subsequent papers of this series we will apply volume-integrals to problems in the field on nondestructive evaluation.

Index Terms — Aircraft structures, computational electromagnetics, electromagnetic nondestructive evaluation, volume-integral equations.

I. INTRODUCTION

The authors of a recent paper [1] claim that a surface integral equation formulation that utilizes method of moments (MoM) with higher-order

basis functions may be the ‘best weapon’ for solving complex problems in electromagnetics. Following [2], only methods based upon finite-elements (FEM), finite-difference time-domain (FDTD), or MoM seem to have been considered as candidate techniques. Furthermore, certain conclusions are drawn in [2] that suggest that MoM is suited only for problems with homogeneous materials, or that finite methods are better suited to handle arbitrary bodies. By MoM, it is clear that both papers’ authors have in mind surface-integral equations. In this paper, we apply computational electromagnetics in the arena of quantitative nondestructive evaluation (NDE), and show errors with the conclusions in [1] and [2] when volume-integral equations are considered.

Even though earlier work in formulating scattering problems by integral equations [3] existed, the emergence of integral equations into the arena of contemporary computational electromagnetic was through the notion of ‘moment methods’ in 1968 [4]. Since that time, volume-integral equations (in which the unknowns are currents distributed throughout a finite volume of space) have been applied to scattering problems in free-space [5, 6], and even to biomedical studies [7]. One reason for the success of volume-integral equations in solving these scattering problems is that the very large linear systems that are obtained

by discretization of these equations can be solved with very modest computer resources using conjugate-gradient search methods, coupled with fast-Fourier transforms (FFT).

In applying volume-integral equations to electromagnetic (eddy-current) nondestructive evaluation, we are once again faced with a scattering problem, but now the scatterer is generally buried within a conducting host, which may have a number of layers of different electrical properties. Furthermore, the host may be anisotropic and magnetic. Even for isotropic layered media, the Green's functions that appear in the kernels of the functionals (the integral operators) will be considerably more complex than those in free-space. Furthermore, there will be terms in the volume-integral equation that do not appear in free-space. These will be discussed briefly in Section II; but for details, the reader is invited to study [8] and [9]. By extending the ideas of previous researchers to include new kernels and functionals for layered media, we have developed VIC-3D[©] [10], a volume-integral code for eddy-current nondestructive evaluation (NDE), and have obtained very good results for a wide range of problems using it [8-22]. Validation of the model and code against benchmark experiments is described in [19-22].

II. BACKGROUND

A. Volume-integral equations for ferromagnetic workpieces [8-9]

We start with Maxwell's equations:

$$\begin{aligned}\nabla \times \mathbf{E} &= -j\omega \mathbf{B} \\ \nabla \times \mathbf{H} &= -j\omega \mathbf{D} + \mathbf{J}^{(e)}.\end{aligned}\quad (1)$$

Now, $\mathbf{H} = \mathbf{B}/\mu(\mathbf{r}) = \mathbf{B}/\mu_h + \mathbf{B}/\mu(\mathbf{r}) - \mathbf{B}/\mu_h = \mathbf{B}/\mu_h - \mathbf{M}_a$, where μ_h is the host permeability, and \mathbf{M}_a is the anomalous magnetization vector. Thus, the second of Maxwell's equations may be written

$$\nabla \times \mathbf{B}/\mu_h = -j\omega \mathbf{D} + \mathbf{J}^{(e)} + \nabla \times \mathbf{M}_a, \quad (2)$$

which makes clear that the Amperian current, $\nabla \times \mathbf{M}_a$, is an equivalent anomalous electric current that arises because of the departures of the magnetic permeability of the workpiece from the host permeability, μ_h . $\mathbf{J}^{(e)}$, on the other hand, is an electric current that includes the anomalous current that arises due to differences in electrical conductivity; $\mathbf{J}^{(e)} = \sigma_h \mathbf{E} + (\sigma(\mathbf{r}) - \sigma_h) \mathbf{E} = \sigma_h \mathbf{E} + \mathbf{J}_a$.

Because the host conductivity and permeability are constant within each plane-parallel layer, they can be accounted for by means of Green functions. This leaves us with only the anomalous electric and magnetic sources to be determined. Even though the Amperian current is electrical (because it appears as a source term in the second Maxwell equation (Ampere's law)), we will refer to it as $\mathbf{J}^{(m)}$, to remind us that it is of magnetic origin, and to distinguish it from $\mathbf{J}^{(e)}$ (which now stands for the anomalous electric current, \mathbf{J}_a). The important point, however, is that because the Amperian current behaves as an electrical current, we need only use electric-electric Green functions in the formulation of the problem.

In establishing the volume-integral equations, we simply make use of the fact that the total electric field and magnetic flux density at a point is the sum of the fields due to the probe coil, which we call the incident fields, and those due to the anomalous currents, $\mathbf{J}^{(e)}$ and $\mathbf{J}^{(m)}$.

Hence, we write

$$\begin{aligned}\mathbf{E}^{(i)}(\mathbf{r}) &= \frac{\mathbf{J}^{(e)}(\mathbf{r})}{\sigma_a(\mathbf{r})} - \mathbf{E}^{(0)}(\mathbf{r})[\mathbf{J}^{(e)}] \\ &\quad - \mathbf{E}^{(s)}(\mathbf{r})[\mathbf{J}^{(e)}] - \mathbf{E}^{(0)}(\mathbf{r})[\mathbf{J}^{(m)}] \\ &\quad - \mathbf{E}^{(s)}(\mathbf{r})[\mathbf{J}^{(m)}], \\ \mathbf{B}^{(i)}(\mathbf{r}) &= \frac{\mu(\mathbf{r})\mu_h}{\mu(\mathbf{r}) - \mu_h} \mathbf{M}_a + \frac{1}{j\omega} \nabla \times \mathbf{E}^{(i)}(\mathbf{r})[\mathbf{J}^{(e)}] \\ &\quad + \frac{1}{j\omega} \nabla \times \mathbf{E}^{(s)}(\mathbf{r})[\mathbf{J}^{(e)}] \\ &\quad + \frac{1}{j\omega} \nabla \times \mathbf{E}^{(0)}(\mathbf{r})[\mathbf{J}^{(m)}] \\ &\quad + \frac{1}{j\omega} \nabla \times \mathbf{E}^{(s)}(\mathbf{r})[\mathbf{J}^{(m)}].\end{aligned}\quad (3)$$

In arriving at the second equation, we have used the fact that $\mathbf{B} = -(1/j\omega) \nabla \times \mathbf{E}$, and $\mathbf{M}_a = ((\mu(\mathbf{r}) - \mu_h)/\mu(\mathbf{r})\mu_h) \mathbf{B}$.

The first part of the first equation in (3) is the electric-electric (ee) interaction, and the second part is the electric-magnetic (em) interaction. The two parts of the second equation are, respectively, the magnetic-electric (me) and the magnetic-magnetic (mm) interactions. We decompose the various interactions into the 'infinite-space' part, designated by the superscript, (0), and the 'layered-space' part, designated by the superscript, (s). This is done for convenience in coding and problem solving.

The electric-electric interaction terms are given by:

$$\begin{aligned}
\mathbf{E}^{(0)}(\mathbf{r})[\mathbf{J}^{(e)}] &= \int \Phi^{(e)}(\mathbf{r}-\mathbf{r}')\mathbf{J}^{(e)}(\mathbf{r}')d\mathbf{r}' \\
&+ \frac{1}{k_0^2}\nabla\int\Phi^{(e)}(\mathbf{r}-\mathbf{r}')\nabla'\cdot\mathbf{J}^{(e)}(\mathbf{r}')d\mathbf{r}' \\
\mathbf{E}^{(s)}(\mathbf{r})[\mathbf{J}^{(e)}] &= \int G_{xx}^{(1)(a)}(\mathbf{r}-\mathbf{r}')\mathbf{J}_t^{(e)}(\mathbf{r}')d\mathbf{r}' \\
&+ a_z\int G_{xz}^{(a)}(\mathbf{r}-\mathbf{r}')\mathbf{J}_z^{(e)}(\mathbf{r}')d\mathbf{r}' \\
&+ \int G_{xx}^{(1)(b)}(\mathbf{r}-\mathbf{r}')\mathbf{J}_t^{(e)}(\mathbf{r}')d\mathbf{r}' \\
&+ a_z\int G_{xz}^{(b)}(\mathbf{r}-\mathbf{r}')\mathbf{J}_z^{(e)}(\mathbf{r}')d\mathbf{r}' \\
&+ \nabla_t\int G_{xx}^{(2)(a)'}(\mathbf{r}-\mathbf{r}')\nabla_t'\cdot\mathbf{J}_t^{(e)}(\mathbf{r}')d\mathbf{r}' \\
&+ \nabla_t\int G_{xx}^{(2)(b)'}(\mathbf{r}-\mathbf{r}')\nabla_t'\cdot\mathbf{J}_t^{(e)}(\mathbf{r}')d\mathbf{r}' \\
&+ \frac{1}{k_0^2}\nabla\int G_{xz}^{(a)}(\mathbf{r}-\mathbf{r}')\nabla_t'\cdot\mathbf{J}_t^{(e)}(\mathbf{r}')d\mathbf{r}' \\
&- \frac{1}{k_0^2}\nabla\int G_{xz}^{(b)}(\mathbf{r}-\mathbf{r}')\nabla_t'\cdot\mathbf{J}_t^{(e)}(\mathbf{r}')d\mathbf{r}',
\end{aligned} \tag{4}$$

where $\nabla_t = a_x\frac{\partial}{\partial x} + a_y\frac{\partial}{\partial y}$; $\nabla_t\cdot\mathbf{J} = \frac{\partial J_x}{\partial x} + \frac{\partial J_y}{\partial y}$;

$\mathbf{J}_t = a_x J_x + a_y J_y$, and

$$\begin{aligned}
\Phi^{(e)}(\mathbf{r}-\mathbf{r}') &= -j\omega\mu_0\frac{e^{-jk_0|\mathbf{r}-\mathbf{r}'|}}{4\pi|\mathbf{r}-\mathbf{r}'|} \\
&= \frac{-j\omega\mu_0}{2\pi}\int_0^\infty\frac{e^{-\lambda_0|z-z'|}}{2\lambda_0}J_0(\lambda l)dl.
\end{aligned} \tag{5}$$

In the Bessel transform, $r = [(x-x')^2 + (y-y')^2]^{1/2}$. Integral expressions for the various layered-space Green functions are given in [8]. Note that the terms with the superscript (a) are convolutional (Töplitz) in all three spatial variables; whereas, those with (b) are convolutional in $(x-x')$ and $(y-y')$, but are correlational (Hankel) in $(z-z')$, where z is normal to the layers of the workpiece (see Figure 1). This decomposition is of great importance when solving large systems of equations, as we shall see later.

The Töplitz structure, as shown in the top of Fig. 1, arises when the path between the source point, z' , and field point, z , includes reflections from both boundaries. The total z -directed path length between z' and z is $z-z'+2T$ for path A, and $z'-z+2T$ for path B. In each case, the length includes the difference between the z -coordinate of the source and field points. The Hankel structure, as shown in the bottom of Figure 1, arises when the path between source and field points includes reflections from only one of the

boundaries. The total path length between z' and z is $2Z_0 - (z+z')$ for path A, and $z+z'-2Z_{-1}$ for path B. In each case, the length includes the sum of the source and field z -coordinates.

The electric-magnetic interaction terms are given by substituting $\mathbf{J}^{(m)}$ for $\mathbf{J}^{(e)}$ in (4), and making use of the fact that $\mathbf{J}^{(m)}$ has zero divergence. We will not derive them here. Likewise, the magnetic-electric operators follow directly by taking the curl of (4) [8].

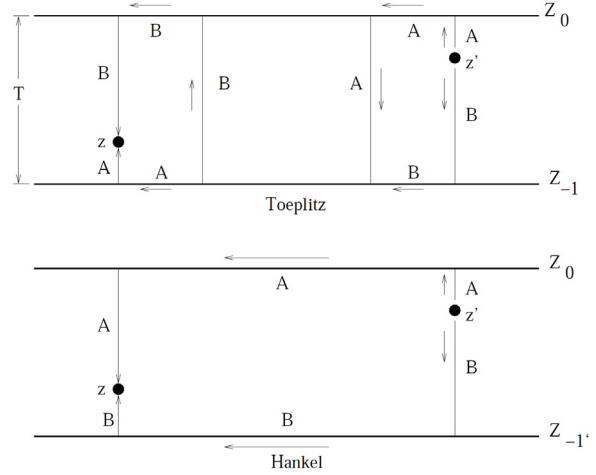


Fig. 1. Illustrating the difference between Töplitz (top) and Hankel (bottom) Green's functions.

B. Discretization via the method of moments (Galerkin)

Define a regular grid in three-dimensional space, with grid spacing δx , δy , δz . Relative to this grid we define $\pi(x)$ to be the unit pulse

$$\pi(x) = \begin{cases} 1, & \text{if } 0 \leq x \leq 1, \\ 0, & \text{otherwise,} \end{cases} \tag{6}$$

and $\pi_{m+1}(x)$ to be the m th-order convolution of $\pi(x)$ (we define $\pi_1(x) = \pi(x)$).

Next, expand the electric current vector as:

$$\begin{aligned}
J_x^{(e)}(\mathbf{r}) &= \sum_{KLM} J_{KLM}^{(x)} T_{KLM}^{(x)(e)}(\mathbf{r}) \\
J_y^{(e)}(\mathbf{r}) &= \sum_{KLM} J_{KLM}^{(y)} T_{KLM}^{(y)(e)}(\mathbf{r}) \\
J_z^{(e)}(\mathbf{r}) &= \sum_{KLM} J_{KLM}^{(z)} T_{KLM}^{(z)(e)}(\mathbf{r});
\end{aligned} \tag{7}$$

the expressions for $T_{KLM}^{(q)(e)}$ are:

$$\begin{aligned}
T_{KLM}^{(x)(e)}(\mathbf{r}) &= \pi_{2K}(x/\delta x)\pi_{1L}(y/\delta y)\pi_{1M}(z/\delta z) \\
T_{KLM}^{(y)(e)}(\mathbf{r}) &= \pi_{1K}(x/\delta x)\pi_{2L}(y/\delta y)\pi_{1M}(z/\delta z) \\
T_{KLM}^{(z)(e)}(\mathbf{r}) &= \pi_{1K}(x/\delta x)\pi_{1L}(y/\delta y)\pi_{2M}(z/\delta z) \\
(K, L, M) &= (0, 0, 0), \dots, (N_x, N_y, N_z),
\end{aligned} \quad (8)$$

where $\pi_{1M}(y/\delta y)$ is the M th unit pulse function, and $\pi_{2K}(x/\delta x)$ is the K th tent function, which is the convolution of $\pi_{1K}(x/\delta x)$ with itself.

The $T^{(q)(e)}(\mathbf{r})$ are called facet elements, because the q th element is constant over the q th facet of the KLM th cell. They are often referred to as ‘divergence-conforming,’ because the divergence of the current density is bounded. Facet elements have been called ‘volumetric rooftop’ functions in [5]. Volumetric rooftop functions have, also, been used in [7] and [6].

We assume that the conductivity is constant, with the value

$$\sigma_{\text{cell}} = \sigma_{\text{max}} + V_c(\sigma_{\text{min}} - \sigma_{\text{max}}), \quad (9)$$

within each cell of dimension $\delta x \times \delta y \times \delta z$. σ_{max} and σ_{min} are, respectively, the maximum and minimum conductivities in the problem, and V_c is the *conductivity volume-fraction*.

Because $\mathbf{J}^{(m)}(\mathbf{r}) = \nabla \times \mathbf{M}_a(\mathbf{r})$, we expand $\mathbf{M}_a(\mathbf{r})$ in ‘curl-conforming’ edge-elements, which have the required differentiability of the curl operation

$$\begin{aligned}
M_x(\mathbf{r}) &= \sum_{KLM} M_{KLM}^{(x)} T_{KLM}^{(x)(m)}(\mathbf{r}) \\
M_y(\mathbf{r}) &= \sum_{KLM} M_{KLM}^{(y)} T_{KLM}^{(y)(m)}(\mathbf{r}) \\
M_z(\mathbf{r}) &= \sum_{KLM} M_{KLM}^{(z)} T_{KLM}^{(z)(m)}(\mathbf{r}),
\end{aligned} \quad (10)$$

where

$$\begin{aligned}
T_{KLM}^{(x)(m)}(\mathbf{r}) &= \pi_{1K}(x/\delta x)\pi_{2L}(y/\delta y)\pi_{2M}(z/\delta z) \\
T_{KLM}^{(y)(m)}(\mathbf{r}) &= \pi_{2K}(x/\delta x)\pi_{1L}(y/\delta y)\pi_{2M}(z/\delta z) \\
T_{KLM}^{(z)(m)}(\mathbf{r}) &= \pi_{2K}(x/\delta x)\pi_{2L}(y/\delta y)\pi_{1M}(z/\delta z).
\end{aligned} \quad (11)$$

These functions are called edge-elements because the expansion coefficient, $M_{KLM}^{(x)}$, is the (constant) value of M_x along the x -directed edge, ($y = (L + 1)\delta y$, $z = (M + 1)\delta z$). There are similar interpretations for $M_{KLM}^{(y)}$ and $M_{KLM}^{(z)}$.

We assume that the magnetic permeability is constant, with the value

$$\mu_{\text{cell}} = \mu_{\text{max}} + V_p(\mu_{\text{min}} - \mu_{\text{max}}), \quad (12)$$

within each cell of dimension $\delta x \times \delta y \times \delta z$. μ_{min} and μ_{max} are, respectively, the maximum and minimum permeabilities in the problem, and V_p is the *permeability volume-fraction*.

We discretize (3) by employing Galerkin’s method, which uses the same vector functions for expansion and testing. The spatial derivatives that could cause problems are removed by the testing process. The procedure for discretization is to first substitute (7) and (10) into (3), and then take moments of each of the first three equations of (3) with the corresponding facet element, and of the second three equations with the corresponding edge element. The result for the electric equation is

$$\begin{aligned}
\begin{bmatrix} \mathbf{E}^{(ix)} \\ \mathbf{E}^{(iy)} \\ \mathbf{E}^{(iz)} \end{bmatrix} &= \begin{bmatrix} \mathbf{Q}^{(x)} & 0 & 0 \\ 0 & \mathbf{Q}^{(y)} & 0 \\ 0 & 0 & \mathbf{Q}^{(z)} \end{bmatrix} \begin{bmatrix} \mathbf{J}^{(x)} \\ \mathbf{J}^{(y)} \\ \mathbf{J}^{(z)} \end{bmatrix} \\
&+ \begin{bmatrix} \mathbf{G}_{(0)}^{(xx)} & \mathbf{G}_{(0)}^{(xy)} & \mathbf{G}_{(0)}^{(xz)} \\ \mathbf{G}_{(0)}^{(yx)} & \mathbf{G}_{(0)}^{(yy)} & \mathbf{G}_{(0)}^{(yz)} \\ \mathbf{G}_{(0)}^{(zx)} & \mathbf{G}_{(0)}^{(zy)} & \mathbf{G}_{(0)}^{(zz)} \end{bmatrix} \begin{bmatrix} \mathbf{J}^{(x)} \\ \mathbf{J}^{(y)} \\ \mathbf{J}^{(z)} \end{bmatrix} \\
&+ \begin{bmatrix} \mathbf{G}_{(a)}^{(xx)} & \mathbf{G}_{(a)}^{(xy)} & \mathbf{G}_{(a)}^{(xz)} \\ \mathbf{G}_{(a)}^{(yx)} & \mathbf{G}_{(a)}^{(yy)} & \mathbf{G}_{(a)}^{(yz)} \\ \mathbf{G}_{(a)}^{(zx)} & \mathbf{G}_{(a)}^{(zy)} & \mathbf{G}_{(a)}^{(zz)} \end{bmatrix} \begin{bmatrix} \mathbf{J}^{(x)} \\ \mathbf{J}^{(y)} \\ \mathbf{J}^{(z)} \end{bmatrix} \\
&+ \begin{bmatrix} \mathbf{G}_{(b)}^{(xx)} & \mathbf{G}_{(b)}^{(xy)} & \mathbf{G}_{(b)}^{(xz)} \\ \mathbf{G}_{(b)}^{(yx)} & \mathbf{G}_{(b)}^{(yy)} & \mathbf{G}_{(b)}^{(yz)} \\ \mathbf{G}_{(b)}^{(zx)} & \mathbf{G}_{(b)}^{(zy)} & \mathbf{G}_{(b)}^{(zz)} \end{bmatrix} \begin{bmatrix} \mathbf{J}^{(x)} \\ \mathbf{J}^{(y)} \\ \mathbf{J}^{(z)} \end{bmatrix} \\
&+ \begin{bmatrix} \mathbf{G}_{(0)} & \mathbf{G}_{(a)} & \mathbf{G}_{(b)} \end{bmatrix} \begin{bmatrix} \mathbf{M}^{(x)} \\ \mathbf{M}^{(y)} \\ \mathbf{M}^{(z)} \end{bmatrix},
\end{aligned} \quad (13)$$

where the \mathbf{Q} ’s are tri-diagonal matrices, the $\mathbf{G}_{(0)}$ ’s the infinite-space matrices, the $\mathbf{G}_{(a)}$ ’s the convolutional layered-space matrices, and the $\mathbf{G}_{(b)}$ ’s the correlational layered-space matrices. The infinite-space matrices are convolutional, also. The superscript (ee) denotes electric-electric matrices, and (em) denotes electric-magnetic matrices. The \mathbf{J} ’s are the unknown electric currents, and the \mathbf{M} ’s are the unknown magnetic polarization vectors. The last block in (13) is simply a short-hand representation of the three blocks above it, except that it represents electric-magnetic interactions.

The magnetic equation is similar to (13), and is given by:

$$\begin{aligned}
\begin{bmatrix} \mathbf{B}^{(ix)} \\ \mathbf{B}^{(iy)} \\ \mathbf{B}^{(iz)} \end{bmatrix} &= \begin{bmatrix} \mathbf{Q}^{(x)} & 0 & 0 \\ 0 & \mathbf{Q}^{(y)} & 0 \\ 0 & 0 & \mathbf{Q}^{(z)} \end{bmatrix}^{(mm)} \begin{bmatrix} \mathbf{M}^{(x)} \\ \mathbf{M}^{(y)} \\ \mathbf{M}^{(z)} \end{bmatrix} \\
&+ \begin{bmatrix} \mathbf{G}_{(0)}^{(xx)} & \mathbf{G}_{(0)}^{(xy)} & \mathbf{G}_{(0)}^{(xz)} \\ \mathbf{G}_{(0)}^{(yx)} & \mathbf{G}_{(0)}^{(yy)} & \mathbf{G}_{(0)}^{(yz)} \\ \mathbf{G}_{(0)}^{(zx)} & \mathbf{G}_{(0)}^{(zy)} & \mathbf{G}_{(0)}^{(zz)} \end{bmatrix}^{(mm)} \begin{bmatrix} \mathbf{M}^{(x)} \\ \mathbf{M}^{(y)} \\ \mathbf{M}^{(z)} \end{bmatrix} \\
&+ \begin{bmatrix} \mathbf{G}_{(a)}^{(xx)} & \mathbf{G}_{(a)}^{(xy)} & \mathbf{G}_{(a)}^{(xz)} \\ \mathbf{G}_{(a)}^{(yx)} & \mathbf{G}_{(a)}^{(yy)} & \mathbf{G}_{(a)}^{(yz)} \\ \mathbf{G}_{(a)}^{(zx)} & \mathbf{G}_{(a)}^{(zy)} & \mathbf{G}_{(a)}^{(zz)} \end{bmatrix}^{(mm)} \begin{bmatrix} \mathbf{M}^{(x)} \\ \mathbf{M}^{(y)} \\ \mathbf{M}^{(z)} \end{bmatrix} \quad (14) \\
&+ \begin{bmatrix} \mathbf{G}_{(b)}^{(xx)} & \mathbf{G}_{(b)}^{(xy)} & \mathbf{G}_{(b)}^{(xz)} \\ \mathbf{G}_{(b)}^{(yx)} & \mathbf{G}_{(b)}^{(yy)} & \mathbf{G}_{(b)}^{(yz)} \\ \mathbf{G}_{(b)}^{(zx)} & \mathbf{G}_{(b)}^{(zy)} & \mathbf{G}_{(b)}^{(zz)} \end{bmatrix}^{(mm)} \begin{bmatrix} \mathbf{M}^{(x)} \\ \mathbf{M}^{(y)} \\ \mathbf{M}^{(z)} \end{bmatrix} \\
&+ \begin{bmatrix} \mathbf{G}_{(0)} & \mathbf{G}_{(a)} & \mathbf{G}_{(b)} \end{bmatrix}^{(me)} \begin{bmatrix} \mathbf{J}^{(x)} \\ \mathbf{J}^{(y)} \\ \mathbf{J}^{(z)} \end{bmatrix},
\end{aligned}$$

where $\mathbf{B}^{(i)}$ is the incident magnetic flux density due to the coil, the superscript (mm) stands for magnetic-magnetic interactions, and (me) stands for magnetic-electric interactions. The magnetic-magnetic \mathbf{Q} matrices are a little more complicated than the electric-electric ones. The important point is that the electric-magnetic, magnetic-electric, and magnetic-magnetic matrices can be computed from the electric-electric.

C. Solution strategies

The discretized equations that are obtained by applying the method of moments to integral equations involve dense matrices; hence, it is important to develop efficient algorithms for solving the discretized equations. For relatively small problems (~ 3000 unknowns), we use the LU factorization (direct method) of the system matrix, but if the problem is too large to accommodate the LU factorization, we employ the iterative conjugate gradient algorithm [23]. All of the examples that will be shown in subsequent papers in this series will use the conjugate gradient algorithm. One advantage that accrues to the direct method, when it is feasible, occurs when (13) and (14) have multiple left-hand sides, as occurs when the probe coil is scanned past a flaw. The solution is then computed serially for each incident field vector after the factorization step.

We take advantage of the convolutional and correlational structure of the matrices of (13) and (14) by using three-dimensional FFT's [9] to evaluate the vector-matrix products. The use of FFT's drastically alters the conclusions reached in an analysis like that in [26], reducing $\sim N^3$ operations to $\sim N^2 \log(N)$. This is obviously important when we have multiple left-hand sides in (13) and (14).

D. Calculating the change in impedance due to flaws in ferromagnetic bodies

The development of the equations relies on the reaction and reciprocity theorems [24], as described in [8].

E. Spatial decomposition via volume-integral equations [25]

If the flaw extends over two or more layers with different electrical constitutive properties, as in Figure 2, then (13) and (14) still hold in each layer (with different matrices), but now $[\mathbf{E}^{(ix)}, \mathbf{E}^{(iy)}, \mathbf{E}^{(iz)}]$ depend upon the coil current plus anomalous currents in other layers. This leads us to consider the volume-integral relation for transfer between region 0 ('source') and region q ('field')

$$\begin{aligned}
\mathbf{E}_x(\mathbf{r}) &= \int G^{(q0)(1)}(x-x', y-y', z, z') \mathbf{J}_x^{(e)}(\mathbf{r}') d\mathbf{r}' \\
&+ \int G^{(q0)(1)}(x-x', y-y', z, z') \mathbf{J}_x^{(m)}(\mathbf{r}') d\mathbf{r}' \\
&+ \frac{\partial}{\partial x} \int G^{(q0)(2)}(x-x', y-y', z, z') \nabla'_i \cdot \mathbf{J}_i^{(e)}(\mathbf{r}') d\mathbf{r}' \\
&+ \frac{\partial}{\partial x} \int G^{(q0)(2)}(x-x', y-y', z, z') \nabla'_i \cdot \mathbf{J}_i^{(m)}(\mathbf{r}') d\mathbf{r}' \\
&+ \frac{1}{k_0^2} \frac{\partial}{\partial x} \int G^{(q0)(3)}(x-x', y-y', z, z') \nabla' \cdot \mathbf{J}^{(e)}(\mathbf{r}') d\mathbf{r}' \\
\mathbf{E}_y(\mathbf{r}) &= \int G^{(q0)(1)}(x-x', y-y', z, z') \mathbf{J}_y^{(e)}(\mathbf{r}') d\mathbf{r}' \\
&+ \int G^{(q0)(1)}(x-x', y-y', z, z') \mathbf{J}_y^{(m)}(\mathbf{r}') d\mathbf{r}' \quad (15) \\
&+ \frac{\partial}{\partial y} \int G^{(q0)(2)}(x-x', y-y', z, z') \nabla'_i \cdot \mathbf{J}_i^{(e)}(\mathbf{r}') d\mathbf{r}' \\
&+ \frac{\partial}{\partial y} \int G^{(q0)(2)}(x-x', y-y', z, z') \nabla'_i \cdot \mathbf{J}_i^{(m)}(\mathbf{r}') d\mathbf{r}' \\
&+ \frac{1}{k_0^2} \frac{\partial}{\partial y} \int G^{(q0)(3)}(x-x', y-y', z, z') \nabla' \cdot \mathbf{J}^{(e)}(\mathbf{r}') d\mathbf{r}' \\
\mathbf{E}_z(\mathbf{r}) &= \int G^{(q0)(4)}(x-x', y-y', z, z') \mathbf{J}_z^{(e)}(\mathbf{r}') d\mathbf{r}' \\
&+ \int G^{(q0)(4)}(x-x', y-y', z, z') \mathbf{J}_z^{(m)}(\mathbf{r}') d\mathbf{r}' \\
&+ \frac{1}{k_0^2} \frac{\partial}{\partial z} \int G^{(q0)(5)}(x-x', y-y', z, z') \nabla' \cdot \mathbf{J}^{(e)}(\mathbf{r}') d\mathbf{r}',
\end{aligned}$$

where $\mathbf{r} \in q$ and $\mathbf{r}' \in 0$. The superscript (e) denotes electrical anomalous currents and (m) denote

magnetic anomalous currents that arise from the presence of permeable material. The numerical superscripts on the various Green's functions refer to certain properties of these functions, and are not important to the discussion.

Taking moments of (15), using the same testing functions described above (with lower-case indices), yields

$$\begin{aligned}
 E_{KLM}^{(x)} &= \sum_{KLM} T_{klm,KLM}^{(ee)(xx)(q^0)} J_{KLM}^{(x)(e)} + \sum_{KLM} T_{klm,KLM}^{(ee)(xy)(q^0)} J_{KLM}^{(y)(e)} \\
 &\quad + \sum_{KLM} T_{klm,KLM}^{(ee)(xz)(q^0)} J_{KLM}^{(z)(e)} \\
 E_{KLM}^{(y)} &= \sum_{KLM} T_{klm,KLM}^{(ee)(yx)(q^0)} J_{KLM}^{(x)(e)} + \sum_{KLM} T_{klm,KLM}^{(ee)(yy)(q^0)} J_{KLM}^{(y)(e)} \\
 &\quad + \sum_{KLM} T_{klm,KLM}^{(ee)(yz)(q^0)} J_{KLM}^{(z)(e)} \\
 E_{KLM}^{(z)} &= \sum_{KLM} T_{klm,KLM}^{(ee)(zx)(q^0)} J_{KLM}^{(x)(e)} + \sum_{KLM} T_{klm,KLM}^{(ee)(zy)(q^0)} J_{KLM}^{(y)(e)} \\
 &\quad + \sum_{KLM} T_{klm,KLM}^{(ee)(zz)(q^0)} J_{KLM}^{(z)(e)},
 \end{aligned} \tag{16}$$

where the transfer matrices satisfy $T_{klm,KLM}^{(q^0)} = T_{k-K,l-L,m-M}^{(q^0)}$; i.e., they are Töplitz (2D-convolution) in (X, Y) . Thus, one can still use two-dimensional FFTs to efficiently execute the computations. The superscript (ee) on the transfer matrices denotes 'electric-electric,' which means that these matrices 'transfer' an electric current in region 0 into an electric field in region q . Similar transfer matrices exist for transferring a magnetic current in region 0 into an electric field in region q , as well as transferring an electric current into a magnetic field and a magnetic current into a magnetic field. All of these other transfer matrices

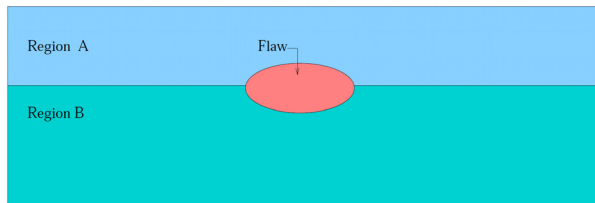


Fig. 2. A flaw in multiple layers.

can be deduced from the electric-electric ones, but the development is lengthy and will not be included here.

III. COMMENTS AND CONCLUSIONS

We have formulated the volume-integral approach in terms of the Galerkin variant of the method of moments, in which the unknown

anomalous currents and the testing functions are expressed in terms of basis functions that are defined on a regular grid. This results in operators that have very special structures; they are either three-dimensional convolutions, or two-dimensional convolutions and one-dimensional correlations, which means that we can use three-dimensional FFTs to accelerate the matrix-vector operations occurring within a conjugate-gradient search algorithm. The use of a highly irregular mesh in the finite-element technique does not allow a similar advantage in the solution process. In the next paper and the remaining ones in this series, we will show how this formulation produces extremely efficient solutions of complex problems.

We have not gone into certain technical details, such as comparing operation counts for a direct matrix-vector multiply versus an FFT-assisted operation. Recent texts, such as [27-29], deal with these issues in more generality, while [30] deals with other fast algorithms for computational electromagnetics.

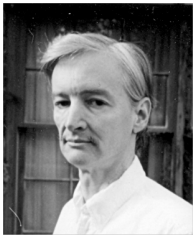
REFERENCES

- [1] M. Yuan, T. K. Sarkar, and B. Kolundzija, "Solution of large complex problems in computational electromagnetics using higher-basis in MoM with out-of-core solvers," *IEEE Antennas and Propagation Magazine*, vol. 48, no. 2, pp. 55-62, April 2006.
- [2] R. Mittra, "A look at some challenging problems in computational electromagnetic," *IEEE Antennas and Propagation Magazine*, vol. 46, no. 5, pp. 18-32, October 2004.
- [3] J. H. Richmond, "Scattering by a dielectric cylinder of arbitrary cross section shape," *IEEE Trans. Antennas and Propagation*, vol. AP-13, pp. 334-341, May 1965.
- [4] R. F. Harrington, *Field Computation by Moment Methods*, The Macmillan Company, New York, 1968.
- [5] M. F. Catedra, E. Gago, and L. Nuño, "A numerical scheme to obtain the RCS of three-dimensional bodies of resonant size using the conjugate gradient method and the fast Fourier transform," *IEEE Trans. Antennas and Propagation*, vol. 37, no. 5, pp. 528-537, May 1989.
- [6] A. P. M. Zwamborn and P. M. van den Berg, "The three-dimensional weak form of the conjugate gradient FFT method for solving scattering problems," *IEEE Trans. Microwave*

- Theory and Techniques*, vol. 40, no. 9, pp. 1757-1766, September 1992.
- [7] A. P. M. Zwamborn, P. M. van den Berg, J. Mooibroek, and F. T. C. Koenis, "Computation of three-dimensional electromagnetic-field distributions in a human body using the weak form of the CGFFT method," *Applied Computational Electromagnetics Society Journal*, vol. 7, no. 2, pp. 26-42, Winter 1992.
- [8] R. K. Murphy, H. A. Sabbagh, J. C. Treece, and L. W. Woo, "A volume-integral code for electromagnetic nondestructive evaluation," *Proceedings 11th Annual Review of Progress in Applied Computational Electromagnetics*, March 1995.
- [9] J. R. Bowler, L. D. Sabbagh, and H. A. Sabbagh, "A theoretical and computational model of eddy-current probes incorporating volume integral and conjugate gradient methods," *IEEE Trans. Magnetics*, vol. 25, no. 3, pp. 2650-2664, May 1989.
- [10] <http://www.kiva.net/~sabbagh>.
- [11] R. K. Murphy, H. A. Sabbagh, A. Chan, and E. H. Sabbagh, "A volume-integral code for electromagnetic nondestructive evaluation," *Proceedings 13th Annual Review of Progress in Applied Computational Electromagnetics*, March 1997.
- [12] H. A. Sabbagh, "Splines and their reciprocal - bases in volume-integral equations," *IEEE Trans. Magnetics*, vol. 29, no. 6, pp. 4142-4152., November 1993.
- [13] H. A. Sabbagh, R. K. Murphy, and E. H. Sabbagh, "Advances in modeling eddy-current NDE of ferromagnetic bodies," *Review of Quantitative Nondestructive Evaluation, American Institute of Physics*, vol. 22A, pp. 383-389, 2003.
- [14] H. A. Sabbagh, L. D. Sabbagh, and J. R. Bowler, "A volume-integral code for eddy-current nondestructive evaluation," *COMPEL*, vol. 9, Supplement A, pp. 67-70, 1990.
- [15] J. R. Bowler, L. D. Sabbagh, and H. A. Sabbagh, "Eddy-current probe impedance due to a surface slot in a conductor," *IEEE Trans. Magnetics*, vol. 26, no. 2, pp. 889-892, March 1990.
- [16] H. A. Sabbagh, J. R. Bowler, and L. D. Sabbagh, "A model of eddy-current probes with ferrite cores," *Nondestr. Test. Eval.*, vol. 5, pp. 67-79.
- [17] H. A. Sabbagh and L. D. Sabbagh, "An eddy-current model for three-dimensional inversion," *IEEE Trans. Magnetics*, vol. MAG-22, no. 4, pp. 282-291, July 1986.
- [18] H. A. Sabbagh, L. D. Sabbagh, and S. N. Vernon, "Verification of an eddy-current flaw inversion algorithm," *IEEE Trans. Magnetics*, vol. MAG-22, no. 6, pp. 1881-1886, November 1986.
- [19] H. A. Sabbagh, E. H. Sabbagh, and R. K. Murphy, "Validation of a volume-integral eddy-current code by benchmark experiments," *Review of Progress in Quantitative Nondestructive Evaluation, American Institute of Physics*, vol. 21, pp. 396-402, 2002.
- [20] H. A. Sabbagh, E. H. Sabbagh, and R. K. Murphy, "Recent advances in modeling eddy-current probes," *Review of Progress in Quantitative Nondestructive Evaluation, American Institute of Physics*, vol. 21, pp. 423-429, 2002.
- [21] H. A. Sabbagh, E. H. Sabbagh, and R. K. Murphy, "Reconstruction of semielliptical and epicyclic cracks by eddy-current inversion," *Review of Progress in Quantitative Nondestructive Evaluation, American Institute of Physics*, vol. 21, pp. 715-721, 2002.
- [22] H. A. Sabbagh, E. H. Sabbagh, R. K. Murphy, and J. Nyenhuis, "Assessing thermal barrier coatings by eddy-current inversion," *Review of Progress in Quantitative Nondestructive Evaluation, American Institute of Physics*, vol. 21, pp. 722-727, 2002.
- [23] M. Hestenes, *Conjugate Direction Methods in Optimization*, New York: Springer Verlag, 1980.
- [24] R. F. Harrington, *Time-Harmonic Electromagnetic Fields*, McGraw-Hill Book Company, New York, 1961.
- [25] J. S. Knopp, H. A. Sabbagh, J. C. Aldrin, R. K. Murphy, E.H. Sabbagh, J. Hoffmann, and G.J. Steffes, "Efficient solution of electromagnetic scattering problems using spatial decomposition algorithms," *Review of Progress in Quantitative Nondestructive Evaluation, AIP*, vol. 25A, pp. 299-306, 2006.
- [26] B. M. Kolundzija and V. V. Petrovic, "Comparison of MoM/SIE, Mom/VIE and FEM based on topological analysis of two canonical problems," *IEEE Antennas and Propagation International Symposium*, vol. 1, pp. 274-277, June 1998.
- [27] T. P. Sarkar, *Application of the Conjugate Gradient Method in Electromagnetics and Signal Processing*, Elsevier, New York, 1991.
- [28] M. F. Catedra, R. P. Torres, J. Basterrechea, and E. Gago, *The CG-FFT Method: Application of Signal Processing Techniques to Electromagnetics*, Artech House, Boston, 1995.
- [29] A. Peterson, S. Ray, and R. Mittra, *Computational Methods for Electromagnetics*, IEEE, New York, 1998.
- [30] W. C. Chew, J. M. Jin, E. Michielssen, and J. M. Song, *Fast and Efficient Algorithms in Computational Electromagnetics*, Artech House, Boston, 2001.



Harold A. Sabbagh, received his BSEE and MSEE from Purdue University in 1958, and his Ph.D. from Purdue in 1964. In 1980, he formed Sabbagh Associates, Inc., and did research in the application of computational electromagnetics to nondestructive evaluation (NDE). This research evolved into the commercial volume-integral code, VIC-3D. In 1998, he formed Victor Technologies, LLC, in order to continue this research and further development of VIC-3D. His past professional activities have included a stint as president of ACES, and in 2010, he was elected to the grade of FELLOW in ACES.



R. Kim Murphy received his B.A. in physics from Rice University in 1978 and his Ph.D. in physics from Duke University in 1984. Since 1989, he has worked as a Senior Physicist for Sabbagh Associates Inc., and Victor Technologies, LLC. Dr. Murphy has been active in formulating models and coding in VIC-3D®, performing validation numerical experiments, and solving one-dimensional and three-dimensional inverse problems.



Elias H. Sabbagh received the B.Sc. in Electrical Engineering and the B.Sc. in Economics from Purdue University in 1990 and 1991. He has worked as system administrator, software engineer, and researcher for Victor Technologies since its inception. His interests include object-oriented programming, database administration, system architecture, scientific programming, and distributed programming.



John C. Aldrin received B.Sc. and M.Sc. degrees in mechanical engineering from Purdue University, West Lafayette, IN, USA, in 1994 and 1996 and the Ph. D. degree in theoretical and applied mechanics from Northwestern University,

Evanston, IL, USA in 2001. Since 2001, he has worked as the principal of Computational Tools. His research interests include computational methods: modeling, data analysis and inverse methods, in ultrasonic and eddy current nondestructive evaluation.



Jeremy Knopp received the B. Sc. degree in engineering physics, M.Sc. degree in electrical engineering, and M. Sc. in applied statistics from Wright State University, Dayton, OH, USA, in 2001, 2005, and 2009, respectively. Since 2002, he has worked as a researcher at the nondestructive evaluation (NDE) branch of the Air Force Research Laboratory (AFRL). His research interests include eddy current NDE, computational electromagnetics, inverse problems, and model-assisted probability of detection. In 2009, he won the Charles J. Cleary award for basic research at AFRL.



Mark Blodgett received the B. Sc. in metallurgical engineering from Iowa State University, Ames, Iowa, USA in 1985 and M.Sc. and Ph.D. degrees in materials engineering from University of Dayton, Dayton Ohio, USA in 1992 and 2000, respectively. Since 1986, he has worked as materials research engineer in the Nondestructive Evaluation Branch at the Air Force Research Laboratory. His research interests include developing electromagnetic and multi-modal NDE approaches for materials characterization.

The Joy of Computing with Volume Integrals: Validation and Performance Comparison

Harold A. Sabbagh¹, R. Kim Murphy¹, Elias H. Sabbagh¹,
John C. Aldrin², Jeremy S. Knopp³, and Mark P. Blodgett³

¹ Victor Technologies LLC
Bloomington, IN 47401, USA
has@sabbagh.com, kimmurphy1@aristotle.net, ehs@sabbagh.com,

² Computational Tools
Gurnee, IL 60031, USA
aldrin@computationaltools.com

³ Air Force Research Laboratory (AFRL/RXLP)
Wright-Patterson AFB, OH 45433, USA
jeremy.knopp@wpafb.af.mil, mark.blodgett@wpafb.af.mil

Abstract — This is the second paper in a series dealing with the application of computational electromagnetics to nondestructive evaluation, using the vehicle of volume-integral equations, as developed in the preceding paper in this volume. A challenge-problem in the field of nondestructive evaluation is the inspection of fastener sites for fatigue cracks in multilayer structures. Using the volume-integral equation approach, problems comprising multilayer structures, ferromagnetic fastener sites, gaps between materials interfaces, and the presence of fatigue cracks are accurately modeled. Simulated studies are presented with VIC-3D[®], a proprietary volume-integral code, and comparisons are made with FEM highlighting performance advantages of the VIE approach. Further, the role that volume-integral equations play in the context of other well-known computational-electromagnetic algorithms is discussed.

Index Terms — Aircraft structures, computational electromagnetics, electromagnetic nondestructive evaluation, volume-integral equations.

I. INTRODUCTION

A problem of particular interest in the field of nondestructive evaluation is the inspection of fastener sites in aircraft structures for fatigue cracks. An important class of structures comprises plane-parallel layered media representing joints in

both fuselage and wing locations. The layer stackup typically consists of two to four panels and often includes thin layers of a non-conducting sealant or adhesive between the panels. Additional complexity for computational electromagnetics concerns the fastener shape (countersunk or buttonhead fastener) and material type (where ferrous materials are prevalent). Also, fatigue cracks of complex morphology provide a particular challenge for representation using numerical methods. Prior work has investigated the problem of modeling an eddy current inspection of fastener sites in multilayer structures for fatigue cracks using a volume-integral equation approach [1]. Although good agreement was achieved with experimental results, simplifications in the model representation were used. In this paper, the capability of the volume-integral equation approach with spatial decomposition algorithms is demonstrated to fully address the problem of ferromagnetic fastener sites in multilayer structures with gaps between the layers and cracks emanating from the holes.

II. VALIDATION STUDIES

A. The Cessna sandwich

To demonstrate the capability of the volume-integral equation method, the ‘Cessna sandwich’ example is presented [2]. Figure 1 illustrates the geometry of the Cessna-sandwich, which consists

of three layers of aluminum comprising two different aluminum alloys (conductivities), two ‘air gaps’ representing the non-conducting sealant layers, and a titanium rivet-insert with a countersunk head and a shank connecting all layers [1]. In the model, the layers and gaps make up a uniform background or host (in x and y directions) with the fastener being an ‘anomaly’ requiring a local volume element mesh. Because the anomaly extends through several layers of material with different electromagnetic properties, we must use VIC-3D[®] that has been augmented with the spatial-decomposition algorithm (SDA) of Section II E of the preceding paper to solve the problem.

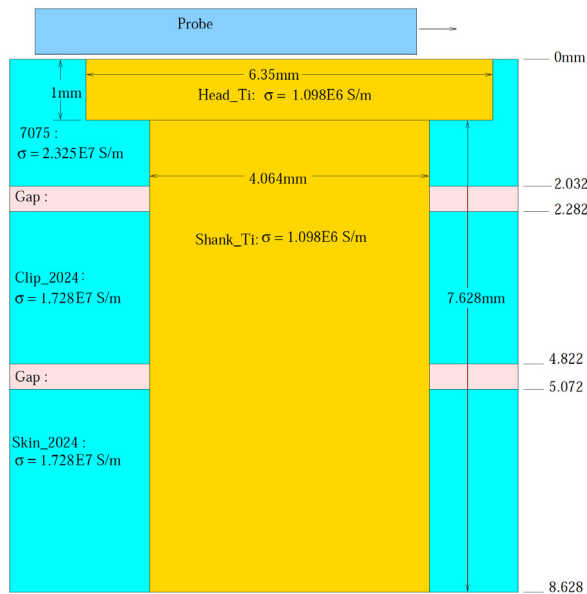


Fig. 1. The Cessna-sandwich problem.

Two model calculations were run based upon Fig. 1, the first with both gaps filled with air, and the second with the top gap filled with 7075-aluminum ($\sigma = 2.325 \times 10^7$), and the other gap filled with 2024-aluminum ($\sigma = 1.728 \times 10^7$). The probe was a simple air-core coil with inner and outer radii of 3.02 mm and 5.14 mm respectively and a height of 2.48 mm. Both model calculations were run with a coil lift-off of 1.0 mm, and a frequency of 2500 Hz. Five spatial-decomposition grids were used to represent the ‘anomaly’ regions, each with $8 \times 8 \times 2$ cells, yielding a total of 1920 unknowns. The plot labeled ‘Gap’ corresponds to the air-filled gaps of Fig. 1, and the plot labeled ‘No Gap’ corresponds to the case in

which the gaps are filled with aluminum. The solution time for the ‘Gap’ run with twenty-six probe scan points is about 6 minutes on an AMD/Athlon machine, whereas the ‘No Gap’ run took about 2 minutes.

For the VIC-3D[®] calculations shown in Fig. 2, it is clear that the effect of the air-filled gaps is to increase somewhat the peak magnitude of the impedance response when compared to the system with aluminum-filled gaps. The results in Fig. 2 are changes in the driving-point impedance of the coil due to the presence of the anomaly, in this case the rivet, compared to the ‘host-only’ impedance in the absence of the anomaly. As such, it is not unusual to have negative values of resistance. Consider, for example, the results at a probe position of -4.0 mm, for which $\delta Z_{\text{gap}} = -0.22 + j0.41 \Omega$ and $\delta Z_{\text{no gap}} = -0.195 + j0.35 \Omega$. In the former, the presence of the rivet insert reduces the resistance of the host structure with the gap, compared to the situation with aluminum filling the original gaps. On the other hand, the presence of the gaps increases the stored magnetic energy, which is manifested in the slightly larger value of reactance. Future work is planned to explore the physics of this model-calculation by showing the anomalous currents within the rivet, as well as the scattered field produced by those currents.

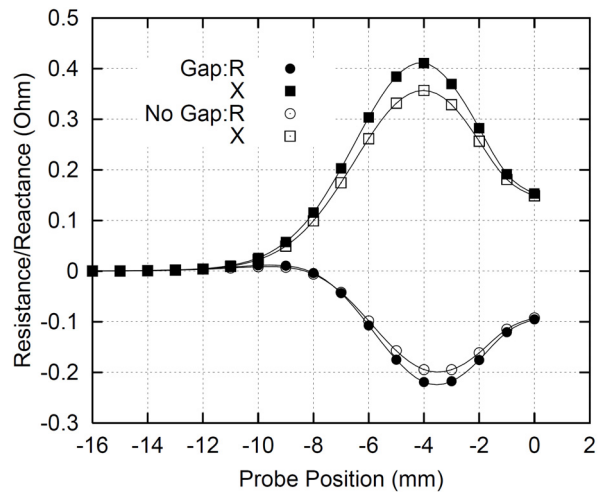


Fig. 2. Model results for the Cessna double sandwich of Fig. 1.

B. Comparison with finite-element method results

To provide a baseline for this challenge-problem concerning the performance of the

volume-integral equation method, an FEM model for the Cessna sandwich problem was implemented in the Opera-3D[®] software package (V9.0)[3]. The numerical formulation of FEM is well established in the literature [4]. A diagram of the model is shown in Fig. 3. Irregular meshes of tetrahedral elements were used with the finite-element formulation to generally represent the complex geometries. The mesh for the model required at least two elements per skin depth in the fastener site region. The lateral dimensions of the plates in the model were extended well beyond the field generated by the eddy current coil to minimize the effect of the part or model domain edges on the measurement response. Continuity conditions were maintained between all part/air interfaces in the model. Far from the coil and fastener site, the boundary conditions at the FEM model boundary were defined with the tangential magnetic field equal to zero. The output of this model is the electric and magnetic field intensities. Change in impedance can then be calculated using the change in resistance associated with dissipated energy in the region of the conductor and the change in inductance related to the stored energy in the whole solution domain. More information on constructing eddy current models in Opera-3D[®] can be found in [3].

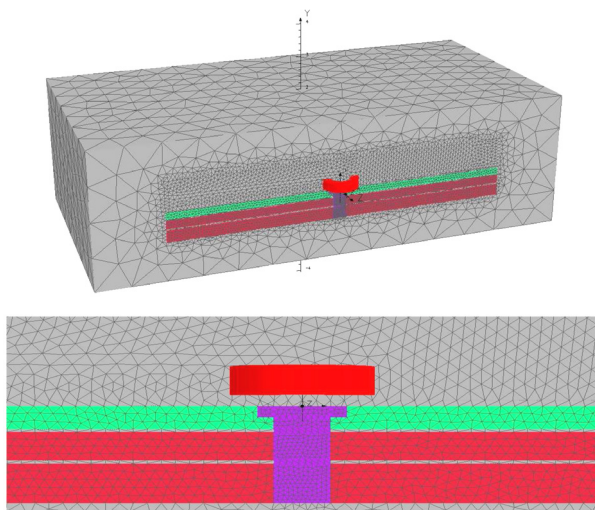


Fig. 3. Diagrams of fastener site FEM model with two gap layers between three aluminum panels.

Figure 4 displays the model results for the Cessna sandwich problem with both airgaps, and compares these results with the VIC-3D[®] results of

Fig. 2 labeled 'Gap'. Clearly, the FEM response shows the same characteristics as does the VIC-3D[®] generated solution. Some differences found in the magnitude of the calculations are likely due to mesh-related error present in the models. Prior work has shown very good agreement between FEM and VIE for this class of problem [1]. Computation of the FEM model required 60 hours on a 3.02 GHz Pentium 4 with 1 GB of memory. For this complex problem, the advantage of the compact formulation with volume-integrals (1920 unknowns) over FEM is obvious.

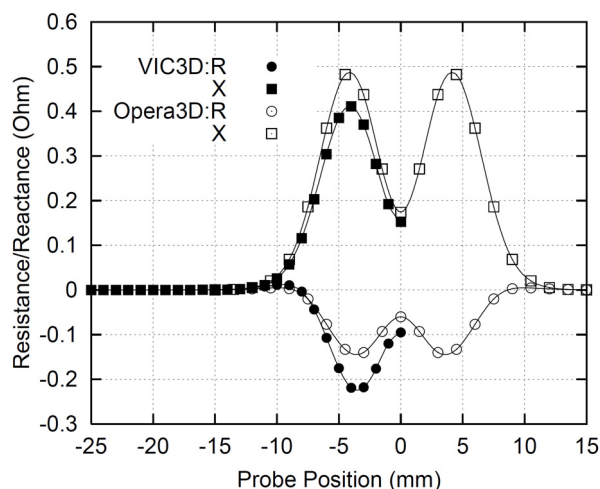


Fig. 4. FEM and VIC-3D[®] model results for the Cessna sandwich with two airgaps.

C. Simulated studies on crack characteristics

From the perspective of nondestructive evaluation, the critical requirement of a NDE model is an accurate representation of the eddy current measurement associated with crack detection. Thus, the model must accurately represent the measurement sensitivity to the crack condition with respect to features such as the fastener site and gaps between layers. To explore the sensitivity of the numerical model to varying crack conditions such as crack length and location, simulated studies were performed using VIC-3D[®]. Again, a class of problems based on setup standards for Cessna (the 'Cessna setups') was simulated in this study. (Future work will thoroughly explore validation of the simulated results with experimental measurements.) The Cessna setups comprise the complex ring probe shown in Fig. 5, the 'hi-lock' pin rivet of Fig. 6, and the various test setups shown in Fig. 7(a) to

Fig. 7(e). Test setup 0 is the root of the other setups, with each of the others differing by the placement of the crack (shown in brown). It should be observed that the setups contain both electrically conducting (lossy) media and ferromagnetic steels. The cracks are modeled as empty slots.

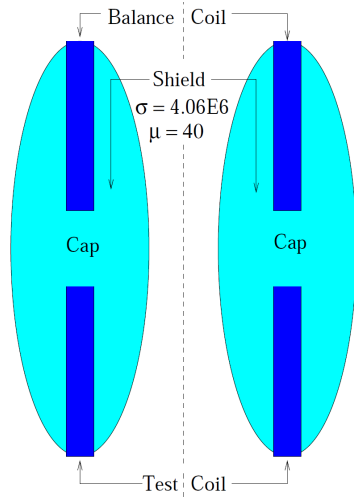


Fig. 5. The ring probe.

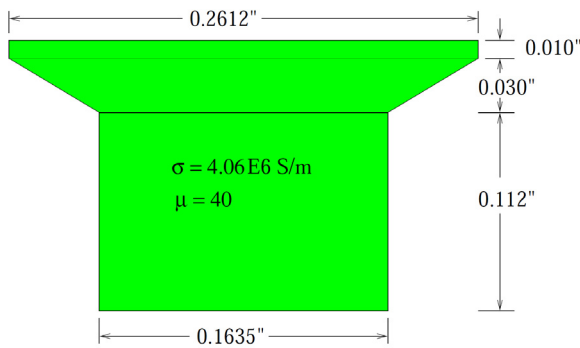


Fig. 6. The hi-lock pin rivet.

In modeling the setups, we use the spatial-decomposition algorithm with five grids, two above the air gap, and two below, with one within the gap. Each grid has $16 \times 16 \times 2$ cells, yielding a total of 15,360 electric and magnetic currents to be determined. The ring probe core was modeled with 12,288 electric and magnetic currents, so that the entire package of unknowns for each setup is 27,648. The models were run at a frequency of 1.0 kHz. Data for determining the presence of a flaw are obtained by varying the lift-off of the ring probe over the range 0, 0.25, 0.7493, and 0.9398

mm. By ‘lift-off’ we mean the position of the bottom of the probe above the workpiece. The solution of the problem with 27,648 unknowns takes about 35 minutes for each lift-off, giving a total solution time of about 2.3 hours for each setup. About 1 Gb of storage for auxiliary files was required.

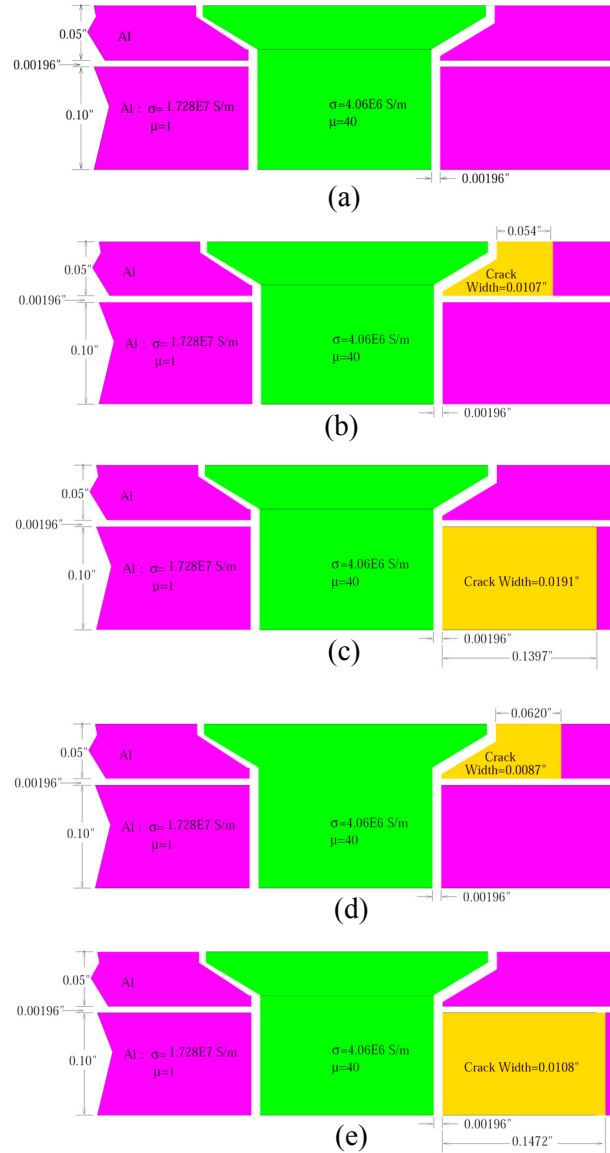


Fig. 7. Test setup (a) 0, (b) 1, (c) 2, (d) 3, (e) 4.

VIC-3D[®] computes impedances, but the industry typically uses analog instruments to measure data, so the final results of the computation are transformed into ‘instrument volts,’ as shown in Fig. 8. Prior work demonstrates

how impedance calculations can be transformed into voltage measurements using calibration data with known samples [1]. Setup 0 is the reference, so it is zero for each lift-off along the negative real axis. The remaining curves indicate the presence of a flaw, and yield information that can be used in an inversion procedure. That will be the subject of another paper in this series.

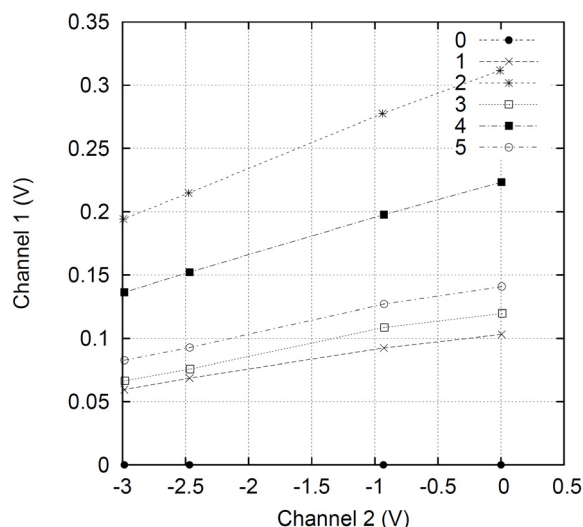


Fig. 8. Final scaled model results for setups 0-5, using setup 0 as the reference. The horizontal and vertical axes are both measured in instrument volts, V. The parametric points on the curves are lift-off values of 0, 0.25, 0.7493, and 0.9398 mm (right to left).

It is clear that setup 2 produces the largest signal, even though the flaw is in the second layer. This is due to the fact that the flaw in this setup has a larger volume than any of the other flaws. Furthermore, it is clear that the flaws in setups 1 and 3, even though they are in the upper layer, are more difficult to distinguish than the other two flaws. This is due to the fact that these two flaws have a smaller volume than those in setups 2 and 4. Setup 5 is the same as setup 4, except that the length of the crack is 0.0986 inch, instead of 0.1472 inch. The response of setup 5 is about 0.67 times the response of setup 4, which is consistent with the fact that the response is roughly proportional to the volume of the defect.

III. COMMENTS AND CONCLUSIONS

We have shown that the volume-integral approach has significant advantages over other

numerical methods, such as the finite-element method, in that the formulation of the numerical model is much simpler in the former than in the latter. Furthermore, the solution time for VIC-3D[®] is extremely short for many problems in NDE, because the formulation in terms of the Galerkin variant of the method of moments on a regular grid results in operators that have very special structures; they are either three-dimensional convolutions, or two-dimensional convolutions and one-dimensional correlations, which means that we can use three-dimensional FFT's to evaluate them in a conjugate-gradient search algorithm. The use of a highly irregular mesh in the finite-element technique does not allow a similar advantage in the solution process.

This advantage accrues from the very different nature of the physics that goes into the formulation of the mathematical models. In volume-integral equations, as well as boundary-integral equations, the unknowns are anomalous currents that are supported in a compact domain, namely the domain of the anomaly; in the example of the Cessna series, the anomaly is the rivet or rivet and crack. In finite-element or finite-difference methods, the unknowns are the electric and magnetic fields, which extend to infinity. This has two disadvantages; it increases the number of unknowns, and requires some method of approximating the 'boundary-at-infinity' in order to truncate the problem domain. This increases the complexity in simply defining the model, and presents an extreme challenge to prospective users who are not skilled in computational electromagnetics.

Furthermore, the FEM method is not particularly well-suited to solve typical problems in NDE, because the anomalies, such as rivets or cracks, require a very complicated mesh, with a large number of very irregular cells. Finally, we conclude from the model calculations of the Cessna series that the spatial decomposition algorithm is a very efficient method of solving problems in which an anomaly extends through layers with different electric and magnetic properties. The spatial decomposition algorithm formulation was, also, demonstrated to be valid for cases where a conducting anomaly is present in a non-conducting layer, such as air. This approach greatly expands the capability of volume-integral equation methods for complex problems in

computational electromagnetics, and in particular nondestructive evaluation. Lastly, rapid solution of the forward problem for computational electromagnetics will, also, be beneficial for the practical application of advanced inverse method techniques for quantitative nondestructive evaluation of material discontinuities.

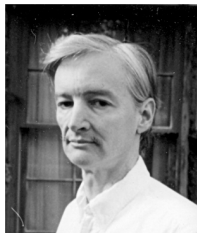
REFERENCES

- [1] J. S. Knopp, J. C. Aldrin, and P. Misra, "Considerations in the validation and application of models for eddy current inspection of cracks around fastener holes," *Journal of Nondestructive Evaluation*, vol. 25, no. 3, pp. 123-138, 2006.
- [2] J. Amos, V. Pendse, and A. Shashikiran, Cessna Aircraft Co., private communication.
- [3] D. C. Carpenter, "Use of the finite element method in simulation and visualization of electromagnetic nondestructive testing applications," *Materials Evaluation*, vol. 58, no.7, pp. 877-881, 2000.
- [4] R. Palanisamy and W. Lord, "Prediction of eddy current probe signal trajectories," *IEEE Transactions on Magnetics*, vol. 16, no. 5, pp. 1083-1085, 1980.



Harold A. Sabbagh, received his BSEE and MSEE from Purdue University in 1958, and his Ph.D. from Purdue in 1964. In 1980, he formed Sabbagh Associates, Inc., and did research in the application of computational electromagnetics

to nondestructive evaluation (NDE). This research evolved into the commercial volume-integral code, VIC-3D. In 1998, he formed Victor Technologies, LLC, in order to continue this research and further development of VIC-3D. His past professional activities have included a stint as president of ACES, and in 2010, he was elected to the grade of FELLOW in ACES.



R. Kim Murphy received his B.A. in physics from Rice University in 1978 and his Ph.D. in physics from Duke University in 1984. Since 1989, he has worked as a Senior Physicist for Sabbagh Associates Inc., and Victor Technologies, LLC. Dr. Murphy has been active in

formulating models and coding in VIC-3D®, performing validation numerical experiments, and solving one-dimensional and three-dimensional inverse problems.



Elias H. Sabbagh received the B.Sc. in Electrical Engineering and the B.Sc. in Economics from Purdue University in 1990 and 1991. He has worked as system administrator, software engineer, and researcher for Victor Technologies since its inception. His interests include object-oriented programming, database administration, system architecture, scientific programming, and distributed programming.



John C. Aldrin received B.Sc. and M.Sc. degrees in mechanical engineering from Purdue University, West Lafayette, IN, USA, in 1994 and 1996 and the Ph.D. degree in theoretical and applied mechanics from Northwestern

University, Evanston, IL, USA in 2001. Since 2001, he has worked as the principal of Computational Tools. His research interests include computational methods: modeling, data analysis and inverse methods, in ultrasonic and eddy current nondestructive evaluation.



Jeremy Knopp received the B.Sc. degree in engineering physics, M.Sc. degree in electrical engineering, and M.Sc. in applied statistics from Wright State University, Dayton, OH, USA, in 2001, 2005, and 2009, respectively. Since 2002, he has worked as a researcher at the nondestructive evaluation (NDE) branch of the Air Force Research Laboratory (AFRL). His research interests include eddy current NDE, computational electromagnetics, inverse problems, and model-assisted probability of detection. In 2009, he won the Charles J. Cleary award for basic research at AFRL.



Mark Blodgett received the B.Sc. in metallurgical engineering from Iowa State University, Ames, Iowa, USA in 1985 and M.Sc. and Ph.D. degrees in materials engineering from University of Dayton, Dayton Ohio, USA in 1992 and 2000, respectively. Since 1986, he has worked as materials research engineer in the Nondestructive Evaluation Branch at the Air Force Research Laboratory. His research interests include developing electromagnetic and multi-modal NDE approaches for materials characterization.

Stable Partial Inductance Calculation for Partial Element Equivalent Circuit Modeling

Zhenfei Song^{1,2}, Fabrice Duval², Donglin Su¹, and Anne Louis²

¹EMC Laboratory

Beihang University, Beijing, 100191, China
songzhenfei@ee.buaa.edu.cn, sdl@buaa.edu.cn

²IRSEEM/ESIGELEC

Saint-Etienne du Rouvray Cedex, 76801, France
zhenfei-song@esigelec.fr, fabrice.duval@esigelec.fr, anne.louis@esigelec.fr

Abstract — Accurate and stable analytical solutions for partial element calculation in partial element equivalent circuit (PEEC) modeling are desirable due to fast and simple usage. Conventional analytical formulae based on integral Neumann formula may give miscalculations when we compute the partial inductance of three-dimensional structures with large spacing. In this paper, a novel model-order reduction (MOR) method is presented for mutual inductance calculation in order to improve its accuracy and stability. Mutual inductances of higher order models are represented by relatively lower order models. The criteria for MOR are revealed and a code implementation routine is described. The numerical accuracy, stability and calculation cost are investigated comparing with conventional procedures. Numerical experiments show that the MOR method can guarantee numerical stability and reduce calculation complexity simultaneously, and it has advantages to be implemented in PEEC modeling for large complex electronic systems.

Index Terms — Model-order reduction (MOR), numerical stability, partial element equivalent circuit (PEEC), partial inductance.

I. INTRODUCTION

A multitude of mixed electromagnetic and circuit problems of ever-increasing frequencies in complex electronic systems make electromagnetic compatibility (EMC) an increasingly troublesome issue, and numerical modeling techniques provide cost effective solutions. The partial element equivalent circuit (PEEC) method was first

introduced by Ruehli in the 1970s [1] and now is a promising numerical method for electromagnetic (EM) modeling of various engineering problems, e.g., EMC, EM interference (EMI), and signal integrity (SI) of high-speed digital circuits [2-4]. The main advantage of PEEC is its ability to provide a circuit interpretation of the electric field integral equation in terms of partial elements, namely resistances, partial inductances, and coefficients of potential [3]. It is especially suitable for mixed electromagnetic and circuit problems for its ease to integrate the field solver with real circuit elements [5]. Different from other integral equation (IE) based EM modeling methodologies, PEEC is a full spectrum method valid from dc to the maximum frequency determined by the meshing [6].

The impact of partial element accuracy on quasi-static PEEC model stability has been discussed in [6], and the major sources of inaccurate partial element values were found to be the utilization of unsuitable calculation routines and poor geometrical meshing. The instabilities associated with a full-wave PEEC model is an important and complicated issue, and reasons for its instabilities have been revealed in [7-11] and several full-wave PEEC models attempts to improve the stability of time domain solutions have been proposed [8-13] in recent years. In this paper, we mainly focus on the stability and accuracy of partial mutual inductance calculation by analytical routines for quasi-static PEEC modeling.

Closed-form formulae for mutual inductance calculations were first presented in Grover's book [14], and Ruehli improved it for better computer

implementation. Ruehli used filament approximation to calculate mutual inductance of three-dimensional multi-conductor interconnection structures [15]. This approximation represented a conductor in terms of a set of filaments in the direction of current flow. Following this procedure, Ruey-Beei Wu further developed his approach later by quadrature formulae [16]. Hoer and Love derived a closed-form formula for the mutual inductance of any pair of parallel rectangular conductors [17]. However, the accuracy of these formulae depends much on the ratio of cross sectional size to segment distance and the aspect ratio of each conductor.

A closed-form mutual inductance equation developed by Zhong and Koh [18] draws attention to the numerical stability. In the following discourse, we use “Zhong’s procedure” to refer strictly to this method. In their procedure, the mutual inductance between two parallel rectangular conductors was expressed as a weighted sum of the self inductances of 64 virtual conductors which are defined by one corner point of the first conductor and one corner point of the second conductor. This formula is numerically more stable than any others before, especially for large-aspect-ratio structures. Unfortunately, it still suffers from numerical stability problems in some particular cases, e.g., the two conductors with large spacing.

The proposed method concerns the EMI modeling for large complex electronic systems with PEEC method, e.g., cable-cable and cable-component coupling behaviors in automotives. High accuracy and stable analytical solutions for partial element calculation in PEEC modeling are desirable due to fast and simple usage. Normally interfering sources and susceptible parts sometimes are localized far away (e.g., one or two meters) in the large systems, and the conventional mutual inductance formulae may give inaccurate values (see Fig. 3). In this paper, a model-order reduction (MOR) scheme is developed to improve the numerical stability of mutual inductance with analytical procedures. Mutual inductance of higher order models are represented by relatively lower order models according to compact MOR criteria. Reduced-order models can guarantee accuracy and reduce calculation complexity simultaneously.

This paper is organized as follows. Analytical formulae for mutual inductance calculation of various structures are derived in Section II. Mathematic preliminary and the MOR criteria together with the working flow of a code implementation are described in Section III. Numerical experiments are discussed in Section IV. In this section, we represent the miscalculation phenomenon, and stable values obtained by our MOR method are, also, presented as a contrast. The numerical accuracy, stability and calculation cost are analyzed in this section, as well. Finally, Section V ends with conclusions and discussions.

II. FORMULATIONS

A. Mutual inductance of a primary PEEC cell

Conventional discretization cells for large-scale PEEC modeling are three dimensional structures [19]. Figure 1 illustrates a calculation model of two rectangular conductors with relevant geometrical parameters. This is a general configuration without any restrictions on the alignment of the two conductors and we can calculate the mutual inductance by a closed-form analytical formula (1).

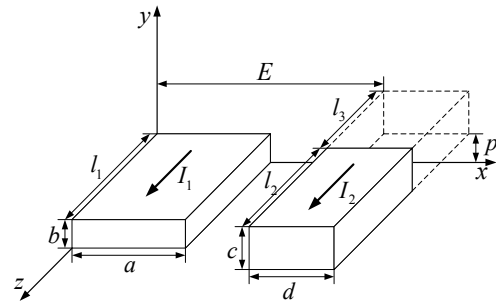


Fig. 1. Two rectangular conductors.

$$M = \frac{\mu}{4\pi} \frac{1}{abcd} \quad (1a)$$

$$\cdot [[[f(X, Y, Z)]_{E+d, E-a}^{E+d, E-a} (X)]_{p+c-b, p}^{p+c, p-b} (Y)]_{l_3+l_2, l_3-l_1}^{l_3+l_2, l_3-l_1} (Z),$$

where

$$\begin{aligned} & [[[f(X, Y, Z)]_{Q_2, Q_4}^{Q_1, Q_3} (X)]_{R_2, R_4}^{R_1, R_3} (Y)]_{S_2, S_4}^{S_1, S_3} (Z) \\ & = \sum_{i=1}^4 \sum_{j=1}^4 \sum_{k=1}^4 (-1)^{i+j+k+1} f(Q_i, R_j, S_k) \end{aligned} \quad (1b)$$

$$\begin{aligned}
 f(X, Y, Z) = & \left(\frac{Y^2 Z^2}{4} - \frac{Y^4}{24} - \frac{Z^4}{24} \right) X \ln(X + \sqrt{X^2 + Y^2 + Z^2}) \\
 & \left(\frac{X^2 Z^2}{4} - \frac{X^4}{24} - \frac{Z^4}{24} \right) Y \ln(Y + \sqrt{X^2 + Y^2 + Z^2}) \\
 & \left(\frac{X^2 Y^2}{4} - \frac{Y^4}{24} - \frac{X^4}{24} \right) Z \ln(Z + \sqrt{X^2 + Y^2 + Z^2}) \\
 & + \frac{1}{60} (X^4 + Y^4 + Z^4 - 3X^2 Y^2 - 3Y^2 Z^2 - 3X^2 Z^2) \sqrt{X^2 + Y^2 + Z^2} \\
 & - \frac{X^3 Y Z}{6} \arctan \frac{YZ}{X \sqrt{X^2 + Y^2 + Z^2}} \\
 & - \frac{X Y^3 Z}{2} \arctan \frac{XZ}{Y \sqrt{X^2 + Y^2 + Z^2}} \\
 & - \frac{X Y Z^3}{6} \arctan \frac{XY}{Z \sqrt{X^2 + Y^2 + Z^2}}.
 \end{aligned} \tag{1c}$$

B. Mutual inductance of various structures

Using primitive integral Neumann formula (2) [20], we can deduce closed-form mutual inductance formulae for various structures as Table 1 shows by the integration technique. In (2), a denotes the cross section which is perpendicular to the direction of current flow, and l means the length of cell. In Table 1, we express the multiple summations in the similar way as (1b)

$$L_{p_{km}} = \frac{\mu}{4\pi} \frac{1}{a_k a_m} \int \int \int \int \frac{dl_k \cdot dl_m}{r_{km}} da_k da_m \tag{2}$$

The model complexity can be measured by its degree of freedom, for example, the degree of freedom of two three-dimensional rectangular conductors is six, and is two for two filaments. In the following discussion, we use the notation nD to refer to the models with n degrees of freedom.

It was shown in [6, 11] that the major source of errors in partial inductance calculation is the numerical dispersion due to high-order terms creating large numbers while the values of other lower-order terms are relatively small. From the expressions in Table 1, we see that the formulae corresponding to lower order models are more stable, and simpler inductance expressions usually result in less calculation cost. The main idea of our MOR method is to present the mutual inductance of a higher order model with a relatively lower order model.

Table 1: Partial mutual inductance formulae of various structures

Order	Configurations	Formulae
0D		$M = \frac{\mu}{4\pi} \frac{1}{l_3}$
1D		$M = \frac{\mu}{4\pi} [f(Z)]_{l_3-l_1}^{l_3} (Z)$ $f(Z) = \ln(Z + \sqrt{Z^2 + P^2})$
2D-1		$M = \frac{\mu}{4\pi} \frac{1}{a} [[f(X, Z)]_{E-a}^E (X)]_{l_2-l_1}^{l_2} (Z)$ $f(X, Z) = X \ln(Z + \sqrt{X^2 + P^2 + Z^2}) + Z \ln(X + \sqrt{X^2 + P^2 + Z^2})$ $- P \arctan \left(\frac{XZ}{P \sqrt{X^2 + P^2 + Z^2}} \right)$

Table 1: Partial mutual inductance formulae of various structures (continued)

<p>2D-2</p>		$M = \frac{\mu}{4\pi} [f(Z)]_{l_1+l_2-l_1, l_1}^{l_1-l_1, l_1+l_2} (Z)$ $f(Z) = Z \ln(Z + \sqrt{Z^2 + P^2}) - \sqrt{Z^2 + P^2}$
<p>3D-1</p>		$M = \frac{\mu}{4\pi} \frac{1}{a} [[f(X, Z)]_{E-a}^E (X)]_{l_1+l_2-l_1, l_1}^{l_1-l_1, l_1+l_2} (Z)$ $f(X, Z) = \frac{Z^2 - P^2}{2} \ln(X + \sqrt{X^2 + P^2 + Z^2}) - \frac{X}{2} \sqrt{X^2 + P^2 + Z^2}$ $- ZP \arctan\left(\frac{XZ}{P\sqrt{X^2 + P^2 + Z^2}}\right) + XZ \ln(Z + \sqrt{X^2 + P^2 + Z^2})$
<p>3D-2</p>		$M = \frac{\mu}{4\pi} \frac{1}{ab} [[f(X, Y, Z)]_{E-a}^E (X)]_{p-b}^p (Y)]_{l_1-l_1}^{l_1-l_1, l_1+l_2} (Z)$ $f(X, Y, Z) = YZ \ln(X + \sqrt{X^2 + P^2 + Z^2}) + XZ \ln(Y + \sqrt{X^2 + P^2 + Z^2})$ $+ XY \ln(Z + \sqrt{X^2 + P^2 + Z^2}) - \frac{X^2}{2} \arctan\left(\frac{YZ}{X\sqrt{X^2 + P^2 + Z^2}}\right)$ $- \frac{Y^2}{2} \arctan\left(\frac{XZ}{Y\sqrt{X^2 + P^2 + Z^2}}\right) - \frac{Z^2}{2} \arctan\left(\frac{XY}{Z\sqrt{X^2 + P^2 + Z^2}}\right)$
<p>4D-1</p>		$M = \frac{\mu}{4\pi} \frac{1}{ad} [[f(X, Z)]_{E+d, E-a}^{E+d, E-a} (X)]_{l_1+l_2-l_1, l_1}^{l_1-l_1, l_1+l_2} (Z)$ $f(X, Z) = \frac{X^2 - P^2}{2} Z \ln(Z + \sqrt{X^2 + P^2 + Z^2}) - X P Z \arctan\left(\frac{XZ}{P\sqrt{X^2 + P^2 + Z^2}}\right)$ $+ \frac{Z^2 - P^2}{2} X \ln(X + \sqrt{X^2 + P^2 + Z^2}) - \frac{X^2 - 2P^2 + Z^2}{6} \sqrt{X^2 + P^2 + Z^2}$
<p>4D-2</p>		$M = \frac{\mu_0}{4\pi} \frac{1}{ac} [[f(X, Y, Z)]_{E-a}^E (X)]_c^{p+c} (Y)]_{l_1+l_2-l_1, l_1}^{l_1-l_1, l_1+l_2} (Z)$ $f(X, Y, Z) = \left(\frac{Z^2}{2} - \frac{Y^2}{6}\right) Y \ln(X + \sqrt{X^2 + Y^2 + Z^2})$ $+ \left(\frac{Z^2}{2} - \frac{X^2}{6}\right) X \ln(Y + \sqrt{X^2 + Y^2 + Z^2}) + XYZ \ln(Z + \sqrt{X^2 + Y^2 + Z^2})$ $- \frac{XY}{3} \sqrt{X^2 + Y^2 + Z^2} - \frac{Z^3}{6} \arctan\left(\frac{XY}{Z\sqrt{X^2 + Y^2 + Z^2}}\right)$ $- \frac{X^2 Z}{2} \arctan\left(\frac{YZ}{X\sqrt{X^2 + Y^2 + Z^2}}\right) - \frac{Y^2 Z}{2} \arctan\left(\frac{XZ}{Y\sqrt{X^2 + Y^2 + Z^2}}\right)$

Table 1: Partial mutual inductance formulae of various structures (continued)

<p>4D-3</p>		$M = \frac{\mu_0}{4\pi ab} [[f(X, Y, Z)]_{E-a}^E (X)]_{p-b}^p (Y)]_{l_1+l_2-l_1}^{l_1+l_2-l_1} (Z)$ <p>$f(X, Y, Z)$ is as above 4D-2 model (perpendicular thin tapes)</p>
<p>5D</p>		$M = \frac{\mu}{4\pi abd} [[f(X, Y, Z)]_{E+d-a, E}^{E+d, E-a} (X)]_{p-b}^p (Y)]_{l_1+l_2-l_1}^{l_1+l_2-l_1} (Z)$ $f(X, Y, Z) = \left(\frac{X^2}{2} - \frac{Y^2}{6}\right) YZ \ln(Z + \sqrt{X^2 + Y^2 + Z^2}) - \frac{X^3 Z}{6} \arctan \frac{YZ}{X\sqrt{X^2 + Y^2 + Z^2}}$ $+ \left(\frac{Z^2}{2} - \frac{Y^2}{6}\right) XY \ln(X + \sqrt{X^2 + Y^2 + Z^2}) - \frac{XZ^3}{6} \arctan \frac{XY}{Z\sqrt{X^2 + Y^2 + Z^2}}$ $- \frac{XY^2 Z}{2} \arctan \frac{XZ}{Y\sqrt{X^2 + Y^2 + Z^2}} - \frac{3X^2 - 2Y^2 + 3Z^2}{24} Y\sqrt{X^2 + Y^2 + Z^2}$ $+ \frac{1}{24} (6X^2 Z^2 - X^4 - Z^4) \ln(Y + \sqrt{X^2 + Y^2 + Z^2})$

III. MODEL-ORDER REDUCTION METHOD

A. Criteria for MOR method

The lemma for order reduction in the appendix is the mathematical foundation of our MOR method. Regarding the mutual inductance calculation, a specific MOR criterion in one dimension with the size of a is as (3) describes according to the lemma.

$$a \left| \frac{d}{dX_1} \int_E^{E+d} \int_0^b \int_p^{p+c} \int_0^{l_1} \int_{l_3}^{l_3+l_2} \frac{1}{R} dX_2 dY_1 dY_2 dZ_1 dZ_2 \right| \leq \epsilon \quad (3)$$

where $R = \sqrt{(X_1 - X_2)^2 + (Y_1 - Y_2)^2 + (Z_1 - Z_2)^2}$.

As a result of (4), the criterion (3) is equivalent with (5a).

$$a \left| \frac{d}{dX_1} \int_E^{E+d} \int_0^b \int_p^{p+c} \int_0^{l_1} \int_{l_3}^{l_3+l_2} \frac{1}{R} dX_2 dY_1 dY_2 dZ_1 dZ_2 \right| \leq abcdl_1 l_2 \cdot \max(|(X_1 - X_2) dX_1| / R^3) \quad (4)$$

$$V_1 V_2 \cdot \max |Q| \cdot a / (\min R)^3 \leq \epsilon. \quad (5a)$$

Here, V_1 and V_2 denote the volumes of two rectangular cells ($V_1 = a \cdot b \cdot l_1$, $V_2 = c \cdot d \cdot l_2$). Following this procedure, the quantified MOR criteria in the other five dimensions (i.e., with sizes of b , l_1 , d , c , l_2 in Fig. 1) are obtained as (5b) - (5f) describe.

$$V_1 V_2 \cdot \max |R| \cdot b / (\min R)^3 \leq \epsilon \quad (5b)$$

$$V_1 V_2 \cdot \max |S| \cdot l_1 / (\min R)^3 \leq \epsilon \quad (5c)$$

$$V_1 V_2 \cdot \max |Q| \cdot d / (\min R)^3 \leq \epsilon \quad (5d)$$

$$V_1 V_2 \cdot \max |R| \cdot c / (\min R)^3 \leq \epsilon \quad (5e)$$

$$V_1 V_2 \cdot \max |S| \cdot l_2 / (\min R)^3 \leq \epsilon. \quad (5f)$$

The value of ϵ depends on the permitted error and will influence the adoption of reduced-order models. Normally, smaller values of ϵ will produce more rigorous reduced-order models, while larger values will generate approximate model-order reduction.

In the previous formulae (5), elements of the arrays Q , R , and S are summation limits of X , Y , and Z variables in (1), respectively, e.g., $Q = [E + d, E + d - a, E - a, E]$. The $\min R$ means the minimum distance of two cells which can be calculated by an arithmetic expression (6).

$$\min R = \sqrt{\min_x^2 + \min_y^2 + \min_z^2} \quad (6)$$

where

$$\min_x = \begin{cases} \min |Q| & Q = |Q|, \text{ or } Q = -|Q| \\ 0 & \text{otherwise} \end{cases}$$

$$\min_y = \begin{cases} \min |R| & R = |R|, \text{ or } R = -|R| \\ 0 & \text{otherwise} \end{cases}$$

$$\min_z = \begin{cases} \min |S| & S = |S|, \text{ or } S = -|S| \\ 0 & \text{otherwise} \end{cases}$$

In practical applications, when the dimensions in the direction of current (i.e., l_1 or l_2 in Fig. 1) are eliminated according to the MOR criteria, the inductance value is equal to the value obtained by the simplified model multiplied by the eliminated length; otherwise, the inductance value of the primitive model is equivalent with the reduced-order model.

B. Code implementation

In this section, we propose a scheme of the working flow of our MOR procedure, which can be easily implemented in MATLAB or other computation environments. We assume the meshing or spatial discretization is carried out according to $\lambda_{\min}/20$ -rule [6]. The code implementation can be carried out, step by step, as follows:

1. Evaluation of the following quantities:
 - a) Find the minimum distance of two cells (i.e., $\min R$) according to (6);
 - b) Find the LHS terms of (5) using matrix approach simultaneously and denote them as $ratio(i)$ ($i=1, 2, 3, 4, 5, 6$, corresponding to dimensions of a, b, l_1, d, c, l_2);
2. Determination of model-order reduction basing on the MOR criteria

An array $flag$ is used to record a binary decision of MOR for corresponding dimensions; i.e., we compare $ratio(i)$ of each dimension with the user-set threshold value ϵ .

$if(ratio(i) \leq \epsilon) \text{ then } flag(i) = 0 \text{ else } flag(i) = 1;$

Then, a fast hierarchical decision algorithm is applied to choose the suitable reduced-order calculation model. The sum of all elements of the array $flag$ is equal to the order of the reduced-order model; e.g., if $sum(flag[]) = 4$, then the primitive model can be represented by a 4D model.

3. Coordinate transformation

A certain model-order value usually corresponds to several primary structures. For instance, there are 15 different 2D models, and all of them can be categorized as two primitive models (see the 2D-1 model and 2D-2 model in Table 1) with some coordinate transformation. We

take a specific case ($flag = [0 \ 0 \ 0 \ 0 \ 1 \ 1]$) to illustrate three procedures of the coordinate transformation.

- a) Determination of specific reduced-order model;

The sum of $flag$ indicates that the reduced-order model is a 2D model which is composed of a point and a thin tape as Fig. 2(a) shows, so it can be categorized to the primitive 2D-1 model illustrated in Table 1 using coordinate transformation.

- b) Matching cells;

The point in Fig. 2(a) is localized at the origin of coordinates which is different from 2D-1 model in Table 1; hence, we need to exchange all the dimensional parameters of the two cells to obtain a model as Fig. 2(b).

- c) Matching coordinates;

The thin tape in primitive 2D-1 model in Table 1 is perpendicular to Y-axis, In order to use the related formula we need to exchange X and Y coordinates of cell with current I_2 .

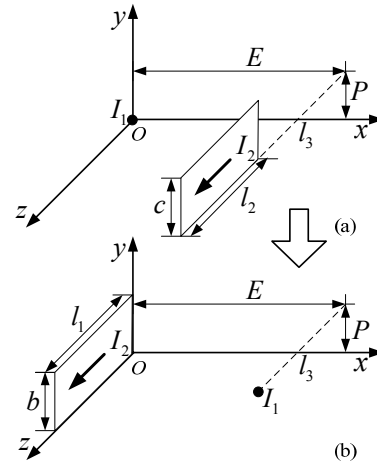


Fig. 2. A coordinate transformation example.

4. Correction of inductance values

In the above case, since the dimension l_1 in the direction of current I_1 is eliminated according to the MOR criteria, the inductance value is equal to the value obtained by the reduced-order model (see 2D-1 model in Table 1) multiplied by the eliminated length l_1 .

IV. NUMERICAL RESULTS

In the following experiments, the cross-sectional dimensions of two rectangular cells are fixed at 0.5 mm×0.5 mm and 0.8

mm \times 0.8 mm. The two cells are aligned at one terminal and their lengths are 4 mm and 6 mm, respectively. We set the threshold value ϵ of 1e-21 in the numerical experiments. Double precision is used in the following results, and all the numerical experiments are conducted under the hardware condition of an ordinary 64-bit computer with a 2.4GHz processor and a 3GB RAM (DDR 3).

To represent the miscalculation phenomenon, mutual inductance values are extracted using the primitive formula (1) and our MOR approach. The inductance values and reduced-orders of adopted models respect to different lateral separation are shown in Fig. 3. The mutual inductance should decrease smoothly as the distance increases; nevertheless, from the data in Fig. 3, it is evident that the primitive formula (1) produces totally wrong inductance values, including even negative results. On the contrary, the proposed MOR method is numerically stable.

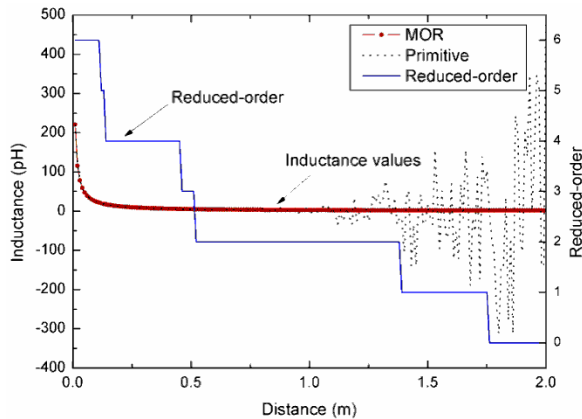


Fig. 3. Mutual inductance values and reduced-orders respect to varying distance.

A. Accuracy

The fast multipole method (FMM) is applied in general PEEC framework to calculate partial elements in a more efficient way without compromising the accuracy [5]. A widely-used tool FastHenry uses a specific multipole-accelerated generalized minimal residual (GMRES) algorithm to compute inductance matrix [21]. To investigate the accuracy of our procedure, mutual inductance values are calculated using our MOR method and FastHenry. The geometrical parameters in the above case are maintained in this study. Figure 4 shows the results.

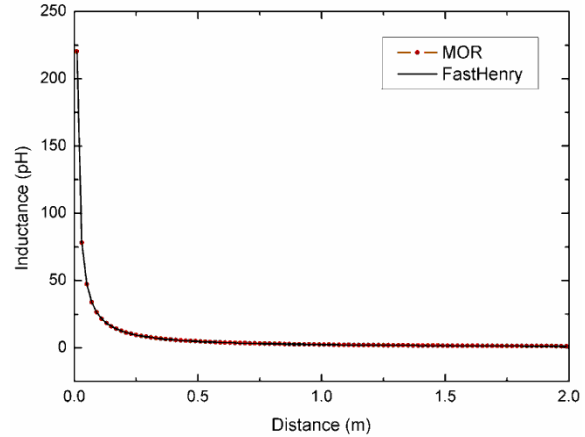


Fig. 4. Mutual inductance values by MOR method and FastHenry.

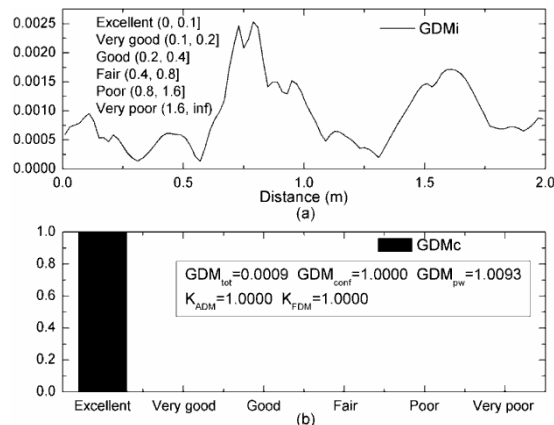


Fig. 5. Feature selective validation of mutual inductance values by MOR method and FastHenry.

The feature selective validation (FSV) [22-24] technique is an effective algorithm that can be used to validate computational electromagnetics (CEM). We use the FSV technique to compare details of the two inductance datasets. Figure 5(a) shows point-by-point comparisons for a global difference measure (GDM). Figure 5(b) illustrates the proportion of the point-by-point analyses that falls into the six natural language descriptor categories (i.e., excellent, very good, good, fair, poor, very poor). Other synthetic FSV parameters are also given in Fig. 5(b). The feature selective validation indicates that our MOR method has an excellent agreement with FastHenry.

B. Stability

Zhong's procedure is numerically more stable than the conventional formulae in [15-17].

Mutual inductance values are extracted by our MOR method and Zhong's procedure in case that the lateral separation between two cells varies up to five meters. Figure 6 shows the computation results. It is evident that our MOR method is numerically more stable than Zhong's procedure for the structures with large spacing.

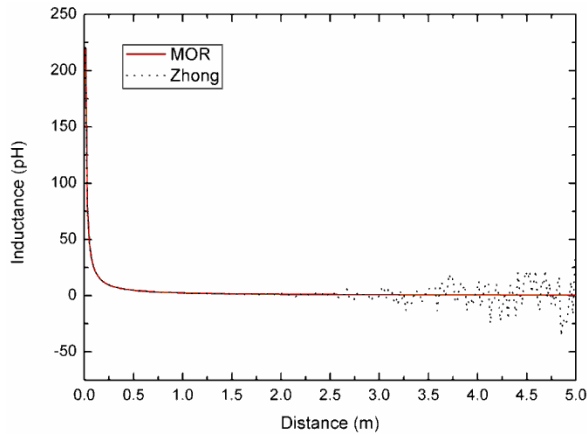


Fig. 6. Mutual inductance values by MOR method and Zhong's procedure.

C. Calculation cost

Table 2 shows the total consumed time of various models in 100,000 independent experiments. The number of summation loops of a 0D model's formula is only 1/64 of a 6D model's formula. Since a particular matrix approach is used to accelerate 64 summation loops in our Matlab code, the realistic consumed time of the 0D model is 43.45% of the 6D model. As a conclusion from Table 2, our MOR procedure not only improves the accuracy and stability, but also reduces the calculation complexity.

Zhong's formula consumes nearly the same time as the primitive 6D model; because it is actually a result of 64 expressions of self inductance [15, 16] which is as complex as the primitive function (1c). That is to say, our MOR

method is, also, faster than Zhong's procedure.

Table 2: Consumed time of various models

Model	Cost time (s)	Normalized percent
6D	26.763	100.00%
5D	22.432	83.82%
4D-1	22.341	83.48%
4D-2	26.345	98.44%
4D-3	26.015	97.21%
3D-1	22.939	85.71%
3D-2	25.336	94.67%
2D-1	16.565	61.90%
2D-2	13.895	51.92%
1D	12.189	45.54%
0D	11.629	43.45%

D. A transmission line structure experiment

In the following, we present a two-conductor transmission line structure to show the influence of inductance values on the accuracy of PEEC modeling. The dimensions of the structure are illustrated in Fig. 7. The two conductors are with the same dimensions, and a common reference ground provides the possibility of generating interference due to crosstalk. An excitation source consisting of a source resistance R_S (50 ohms) and a source voltage V_S (1 volt) is connected to a load R_L (50 ohms) via a generator conductor and a reference ground. A receptor conductor connects the other two terminations, represented by resistors R_{NE} (50 ohms) and R_{FE} (50 ohms).

The crosstalk can be viewed as a transfer function between the input V_S and the outputs V_{NE} and V_{FE} (induced voltages at two ends of the receptor conductor). The frequency domain response of the crosstalk transfer ratio at the near-end (i.e., $20 \times \log_{10}(V_{NE}/V_S)$) was calculated by both MTL theory [25] and PEEC method.

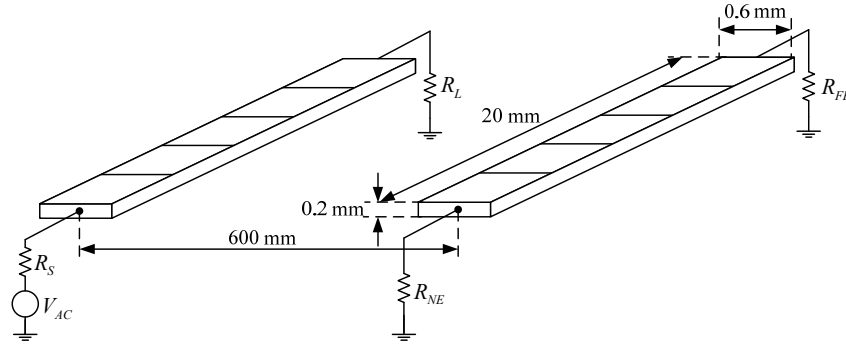


Fig. 7. A two-conductor transmission line structure.

$$L_1 = \begin{bmatrix} 2283.7737 & 532.9164 & 209.1607 & 135.8845 & 101.0547 & 2.6667 & 2.6666 & 2.6664 & 2.6661 & 2.6657 \\ 532.9164 & 2283.7737 & 532.9164 & 209.1607 & 135.8845 & 2.6666 & 2.6667 & 2.6666 & 2.6664 & 2.6661 \\ 209.1607 & 532.9164 & 2283.7737 & 532.9164 & 209.1607 & 2.6664 & 2.6666 & 2.6667 & 2.6666 & 2.6664 \\ 135.8845 & 209.1607 & 532.9164 & 2283.7737 & 532.9164 & 2.6661 & 2.6664 & 2.6666 & 2.6667 & 2.6666 \\ 101.0547 & 135.8845 & 209.1607 & 532.9164 & 2283.7737 & 2.6657 & 2.6661 & 2.6664 & 2.6666 & 2.6667 \\ 2.6667 & 2.6666 & 2.6664 & 2.6661 & 2.6657 & 2283.7737 & 532.9164 & 209.1607 & 135.8845 & 101.0547 \\ 2.6666 & 2.6667 & 2.6666 & 2.6664 & 2.6661 & 532.9164 & 2283.7737 & 532.9164 & 209.1607 & 135.8845 \\ 2.6664 & 2.6666 & 2.6667 & 2.6666 & 2.6664 & 209.1607 & 532.9164 & 2283.7737 & 532.9164 & 209.1607 \\ 2.6661 & 2.6664 & 2.6666 & 2.6667 & 2.6666 & 135.8845 & 209.1607 & 532.9164 & 2283.7737 & 532.9164 \\ 2.6657 & 2.6661 & 2.6664 & 2.6666 & 2.6667 & 101.0547 & 135.8845 & 209.1607 & 532.9164 & 2283.7737 \end{bmatrix} [pH] \quad (7)$$

$$L_2 = \begin{bmatrix} 2283.7737 & 532.9164 & 209.1607 & 135.8845 & 101.0547 & 9.0350 & -7.5292 & 16.5642 & 3.0117 & -6.0233 \\ 532.9164 & 2283.7737 & 532.9164 & 209.1607 & 135.8845 & 3.0117 & 9.0350 & -7.5292 & 16.5642 & 3.0117 \\ 209.1607 & 532.9164 & 2283.7737 & 532.9164 & 209.1607 & 15.0584 & 3.0117 & 9.0350 & -7.5292 & 16.5642 \\ 135.8845 & 209.1607 & 532.9164 & 2283.7737 & 532.9164 & -10.5409 & 15.0584 & 3.0117 & 9.0350 & -7.5292 \\ 101.0547 & 135.8845 & 209.1607 & 532.9164 & 2283.7737 & 10.5409 & -10.5409 & 15.0584 & 3.0117 & 9.0350 \\ 9.0350 & 3.0117 & 15.0584 & -10.5409 & 10.5409 & 2283.7737 & 532.9164 & 209.1607 & 135.8845 & 101.0547 \\ -7.5292 & 9.0350 & 3.0117 & 15.0584 & -10.5409 & 532.9164 & 2283.7737 & 532.9164 & 209.1607 & 135.8845 \\ 16.5642 & -7.5292 & 9.0350 & 3.0117 & 15.0584 & 209.1607 & 532.9164 & 2283.7737 & 532.9164 & 209.1607 \\ 3.0117 & 16.5642 & -7.5292 & 9.0350 & 3.0117 & 135.8845 & 209.1607 & 532.9164 & 2283.7737 & 532.9164 \\ -6.0233 & 3.0117 & 16.5642 & -7.5292 & 9.0350 & 101.0547 & 135.8845 & 209.1607 & 532.9164 & 2283.7737 \end{bmatrix} [pH] \quad (8)$$

$$R + jL = \begin{bmatrix} 0.0027964 + 1.7682e - 008j & 6.3109e - 030 + 6.6661e - 011j \\ 6.3109e - 030 + 6.6661e - 011j & 0.0027964 + 1.7682e - 008j \end{bmatrix}$$

Impedance matrix ($R + jL$) used in the MTL model is computed by the method of moment (MoM).

In order not to introduce the influence of capacitance accuracy, we use a quasi-static PEEC (L_p, R) model [2], and the capacitive coupling is not considered in the transmission line model either.

In the PEEC procedure, each conductor is discretized into five even conductive cells along its length. The inductance matrices L_1 and L_2 are calculated by our MOR method and primitive formula (1) respectively. We see some differences in the mutual inductance values which are in the

off-diagonal terms. It is clear that the primitive formula (1) produce inaccurate inductances including even negative values.

Figure 8 shows the near-end crosstalk transfer function in frequency domain from 1 kHz to 1 MHz. Comparing with the MTL model, it is obvious that the inaccurate partial inductance values cause errors while good agreement is obtained by the MOR inductance calculation routine. This numerical experiment indicates that our MOR method can improve the stability and accuracy of partial inductance values and thus accurate PEEC results.

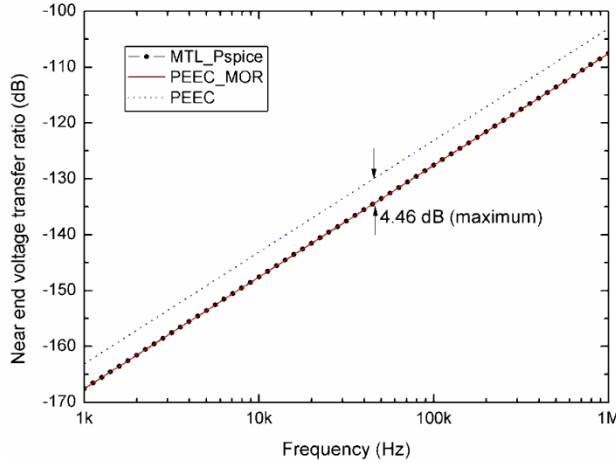


Fig. 8. Frequency-domain representation of the near-end crosstalk transfer function.

V. CONCLUSIONS AND DISCUSSIONS

The proposed novel model-order reduction (MOR) method concerns the stability and accuracy improvement of conventional analytical partial mutual inductance calculation routines. Compact analytical criteria of the MOR approach are presented in this paper and the working flow for a code implementation allows convenient utilization in PEEC modeling. Numerical experiments indicate that the MOR method has its advantages of improving the inductance calculation stability and reducing the calculation complexity, especially for three-dimensional structures with large spacing. This method is more appropriate for PEEC modeling for large complex electronic systems.

This paper only focuses on the analytical inductance calculation for the consideration of fast and simple utilization. Actually, combining analytical and numerical calculation routine (e.g., Gauss-Legendre numerical integration) can be thought of as one option.

APPENDIX

A. A lemma for order reduction

$F(x)$ is a primitive function of $f(x)$. Mathematically, the definite integral of $f(x)$ with limits a and b respect to x equals the difference of $F(x)$ evaluated at b and a , which can be described as (A-1). This implies that $f(x)$ is with respect to a lower order of x comparing with $F(x)$.

$$\int_a^b f(x)dx = F(b) - F(a) \quad (\text{A-1})$$

Suppose the conditions a) and b) can be satisfied simultaneously, it is easy to proof that $(b-a) \cdot f(x)$ is an approximation to $F(b) - F(a)$ for any value of x in the interval $[a, b]$; thus, a lower order formula $f(x)$ can represent the higher order formula $F(x)$.

- $f(x)$ is a continuous monotonic function in an interval $[a, b]$;
- $|(b-a)f'(x)| \leq \varepsilon$, ε is an extremely small positive value;

B. Brief proof of the lemma

From the view of the limitation theory, we can draw a conclusion as (A-2) if the conditions a) and b) can be satisfied simultaneously.

$$\lim_{x \in [a, b]} (b-a)f'(x) = 0 \quad (\text{A-2})$$

(A-2) implies two cases:

Case 1: $b-a \rightarrow 0$, this means the limitation of integral interval is zero;

$$\int_a^b f(x)dx = F(b) - F(a) \approx (b-a)f(x) \rightarrow 0 \quad (\text{A-3})$$

Case 2: $f'(x) \rightarrow 0$, that is, $f(x)$ is a constant function with respect to $x \in [a, b]$;

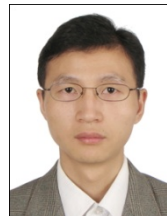
$$\int_a^b f(x)dx = F(b) - F(a) \approx (b-a)f(x) \quad (\text{A-4})$$

Considering (A-3) and (A-4), we can draw the conclusion as the lemma describes.

REFERENCES

- [1] A. E. Ruehli, "Equivalent circuit models for three dimensional multiconductor systems," *IEEE Trans. on Microwave Theory and Tech.*, vol. 22, 1974.
- [2] A. E. Ruehli and A. C. Cangrllaris, "Progress in the methodologies for the electrical modeling," *Proceedings of IEEE*, vol. 89, pp. 740-771, 2001.
- [3] G. Antonini, "The partial element equivalent circuit method for EMI, EMC and SI analysis," *ACES Newsletter*, vol. 21, pp. 8-32, 2006.
- [4] G. Antonini, G. Miscione, and J. Ekman, "PEEC modeling of automotive electromagnetic problems," *ACES Newsletter*, vol. 23, pp. 39-50, 2008.
- [5] G. Antonini, "Fast multipole formulation for PEEC frequency domain modeling," *ACES Newsletter*, vol. 17, 2002.

- [6] J. Ekman, G. Antonini, and A. E. Ruehli, "Impact of partial element accuracy on PEEC model stability," *IEEE Trans. on Electromagnetic Compatibility*, vol. 48, pp. 19-32, 2006.
- [7] S. V. Kochetov and G. Wollenberg, "Stability of full-wave PEEC models: reason for instabilities and approach for correction," *IEEE Trans. on Electromagnetic Compatibility*, vol. 47, pp. 738-748, 2005.
- [8] S. V. Kochetov and G. Wollenberg, "Stable and effective full-wave PEEC models by full-spectrum convolution macromodeling," *IEEE Trans. on Electromagnetic Compatibility*, vol. 49, pp. 25 - 34, 2007.
- [9] G. Antonini and P. Pepe, "Input-to-state stability analysis of partial-element equivalent-circuit models," *IEEE Trans. on Circuits and Systems I: Regular Papers*, vol. 56, pp. 673 - 684, 2009.
- [10] Q. Ha, D. Yue, and X. Ma, "Stability analysis for a partial element equivalent circuit (PEEC) model of neutral type," *Proceedings of the 2004 IEEE International Conference on Control Applications*, 2004, pp. 153 - 158.
- [11] A. E. Ruehli, U. Miekka, and H. Heeb, "Stability of discretized partial element equivalent EFIE circuit models," *IEEE Trans. on Antennas and Propagation*, vol. 43, pp. 553 - 559, 1995.
- [12] X. Zhang and Q. Han, "A new stability criterion for a partial element equivalent circuit model of neutral type," *IEEE Trans. on Circuits and Systems II: Express Briefs*, vol. 56, pp. 798 - 802, 2009.
- [13] J. E. Garrett, A. E. Ruehli, and C. R. Paul, "Accuracy and stability improvements of integral equation models using the partial element equivalent circuit (PEEC) approach," *IEEE Trans. on Antennas and Propagation*, vol. 46, pp. 1824 - 1832, 1998.
- [14] F. Grover, *Inductance Calculations: Working Formulas and Tables*. New York: Dover, 1962.
- [15] A. E. Ruehli, "Inductance calculations in a complex integrated circuit environment," *IBM J. Res. Develop.*, vol. 16, pp. 470-481, 1972.
- [16] R. Wu, C. Kuo, and K. K. Chang, "Inductance and resistance computations for three-dimensional multiconductor interconnect structures," *IEEE Trans. on Microwave Theory and Techniques*, vol. 40, pp. 263 - 270, 1992.
- [17] C. Hoer and C. Love, "Exact inductance equations for rectangular conductors with applications to more complicated geometries," *Journal of Research of the National Bureau of Standards*, vol. 69C, pp. 127-137, 1965.
- [18] G. Zhong and C. Koh, "Exact closed-form formula for partial mutual inductances of rectangular conductors," *IEEE Trans. on Circuits and Systems I: Fundamental Theory and Applications*, vol. 50, pp. 1349 - 1352, 2003.
- [19] F. Freschi and M. Repetto, "A general framework for mixed structured/unstructured PEEC modelling," *ACES Journal*, vol. 23, pp. 200 - 206, 2008.
- [20] J. D. Jackson, *Classical Electrodynamics, 3rd Edition*. New York: John Wiley & Sons, 1998.
- [21] M. Kamon, M. J. Tsuk, and J. K. White, "FASTHENRY: A multipole-accelerated 3-D inductance extraction program," *IEEE Trans. on Microwave Theory and Techniques*, vol. 42, pp. 1750-1758, 1994.
- [22] "Standard for validation of computational electromagnetics computer modeling and simulation," *IEEE Standard P1597*, 2008.
- [23] A. P. Duffy, A. J. M. Martin, A. Orlandi, G. Antonini, T. M. Benson, and M. S. Woolfson, "Feature Selective Validation (FSV) for validation of computational electromagnetics (CEM). Part I - The FSV method," *IEEE Trans. on Electromagn. Compatibility*, vol. 48, pp. 449 - 459, 2006.
- [24] A. Orlandi, A. P. Duffy, B. Archambeault, G. Antonini, D. E. Coleby, and S. Connor, "Feature Selective Validation (FSV) for validation of computational electromagnetics (CEM). Part II - Assessment of FSV performance," *IEEE Trans. On Electromagn. Compatibility*, vol. 48, pp. 460 - 467, 2006.
- [25] C. R. Paul, *Analysis of Multiconductor Transmission Lines*. New York: John Wiley & Sons, 1994.



Zhenfei Song was born in Jiangsu, China, in 1983. He received his B.S. degree in Physics from Shandong University, China, in 2006. He is now working directly towards the Ph.D. degree in EMC laboratory, Beihang University (BUAA), China. Sponsored by the China Scholarship Council, he is studying under a joint Ph.D. program (2009-2011) with IRSEEM/ESIGELEC in France.

His current research interests include electromagnetic modeling, as well as EMC diagnosis methodologies for system-level EMI problems.



Fabrice Duval was born in Rouen, France, in 1973. He received the Ph.D. degree in electronic engineering from the University of Paris XI, France, in 2007.

He is currently the Head of EMC laboratory of Research Institute for Embedded Systems (IRSEEM), the École Supérieure d'Ingénieurs Généralistes (ESIGELEC) in Rouen, France. His main research activity is EMC modeling for large systems (automotives and aeronautics) in order to produce new tools and models of wires, MOS, passive components.



Donglin Su was born in Beijing, China, in 1960. She received the B.S. degree, the M.S. degree and the Ph.D. degree in Electrical Engineering from Beihang University (BUAA), Beijing, China, in 1983, 1986, and 1999,

respectively.

She joined the faculty of the Department of Electrical Engineering, BUAA, in 1986, where she was first an assistant, then a lecturer, and later on, an associate professor, and she is currently a professor and the deputy dean of the School of Electronic and Information Engineering. From 1996 to 1998, she finished her Ph.D. researching under a BUAA-UCLA joint Ph.D. program in the University of California at Los Angeles (UCLA), USA. Her research interests include the numerical methods for microwave and millimeter-wave integrated circuits. Currently, she is involved in the research of “top to down, systemic, quantificational EMC design methodology” for various aircrafts. She is the author of more than 80 papers and the coauthor of several books.

Dr. Su is a senior member of the Chinese Institute of Electronics (CIE). Currently, she serves the Chair of Beijing Chapter, IEEE Antennas and Propagation Society; and the deputy chair of Antennas Society, CIE. She received a Chinese National Award for Science and Technology Progress in 2007.



Anne Louis was born in Chateauroux, France, in 1973. She received her M.S. degree in Electronics and Automatics from the University of Limoges, Limoges, France, in 1994.

In 1995, she joined the Institut de Recherche en Communications Optiques et Microondes (IRCOM) where she was involved in broadband active filters design methods. She received the Ph.D. degree in Microwave communications from IRCOM, University of Limoges, France in 1998. In 1999, she joined the École Supérieure d'Ingénieurs Généralistes (ESIGELEC), Rouen, France, where she is currently a lecturer in electromagnetism and microwaves. Since 2003, she is the Head of the Electronics and Systems department of Research Institute for Embedded Systems (IRSEEM), Rouen, France and in-charge of the “Engineering of electronic systems for telecommunications” specialization in ESIGELEC. In 2006, she was entitled to supervise research and she is the Director of Doctoral Training at ESIGELEC since 2008.

Complex Incomplete Cholesky Factorization Preconditioned Bi-conjugate Gradient Method

Y.J. Zhang and Q. Sun

School of Aeronautics
Northwestern Polytechnical University, Xi'an, 710072, P.R. China
zyj19191@nwpu.edu.cn

Abstract—Linear systems generated by finite element method (FEM) always have a symmetrical sparse system matrix, which requires a large amount of computation and memory effort to access its zero elements. To address this problem, a fully-sparse storing scheme is proposed to store only nonzero symmetrical elements of the sparse system matrix. Meanwhile, for some ill-conditioned system matrixes, conventional iterative solution methods may incur such problems as slow convergence and even failure of convergence. To solve this problem, we further develop a fast convergent preconditioned bi-conjugate gradient method (PBCG) based on a real incomplete Cholesky factorization preconditioner. Numerical experiments show that the proposed method accelerates the convergence and is applicable for the large-scale complex linear systems.

Index Terms—Bi-conjugate gradient method, complex sparse linear system, incomplete Cholesky factorization preconditioner.

iters number of iterations
time time of iterations, unit is second

I. INTRODUCTION

Many electromagnetic numerical evaluations are involved in solving large-scale complex linear systems. Direct methods generally require heavy storage and computation load. As alternative approaches, high-performance iterative methods have been attracting more and more attentions in solving the complex linear system in recent years. However, if the complex linear system is of very high dimension or its system matrix is ill-conditioned, iterative methods may incur such problems as slow convergence and even failure of convergence. Fortunately, these problems can be addressed by appropriate preconditioning methods [1-3]. One most frequently used preconditioned method is the incomplete Cholesky factorization algorithm. In this paper, a real incomplete Cholesky factorization algorithm is extended into the complex field, and a complex incomplete preconditioned bi-conjugate gradient method is proposed to solve the complex large scale linear systems.

The efficiency of solving large-scale sparse complex linear systems, also, depends on storing methods for system matrixes. In order to save storage space and access the elements conveniently, we introduce a fully-sparse storing scheme that stores only nonzero symmetrical elements of system matrix by a chain pattern. Compared with current popular storing methods, the proposed method has the least storing scale and is obviously advantageous for large-scale sparse matrixes especially.

The contents of this paper include the fully-sparse storing scheme, complex incomplete preconditioned bi-conjugate gradient method,

SYMBOLS

$C^{n \times n}$	$n \times n$ complex matrix
C^n	n complex vector
$R^{n \times n}$	$n \times n$ real matrix
R^n	n real vector
A^*	conjugate matrix
A^{-1}	inverse matrix
x^*	conjugate vector
α^*	conjugate complex number
ε	error
$\ \cdot \ $	Euclidean norm
$(; \cdot)$	Euclidean product

algorithmic implementation, and numerical experiments, which demonstrate both applicability and effectiveness of the proposed method.

II. FULLY-SPARSE STORING SCHEME

An efficient fully-sparse storing scheme is presented for storing the system matrix by exploiting its properties of sparsity and symmetry. In this fully-sparse database, only nonzero symmetrical elements of system matrix are stored by using a chain pattern. Both single chain and double chain are applicable in the dynamic database. In this section, the sparse storage scheme based on a single chain pattern is presented. Extension to double chain is straightforward.

For a symmetric sparse matrix $A \in C^{n \times n}$, four one-dimension arrays are necessary to store and manage its nonzero elements. These arrays are defined as follows:

(1) Real array named DATA stores nonzero elements of lower triangle part of matrix A , row by row.

(2) Integer array named JCOL stores column numbers of the nonzero elements in the array DATA.

(3) Integer array named LINK stores index numbers of the nonzero elements. For instance, in some row the index number of the i th nonzero element is the address of next nonzero element in the array DATA. If the i th nonzero element is the last element stored in this row, then $LINK(i)=0$.

(4) Integer array named HEAD stores address of first nonzero element of every row in the array DATA.

For example, if a symmetric sparse matrix $A \in C^{5 \times 5}$ is expressed in equation (1), the four storing arrays in the full-sparse database are shown in Table 1.

$$A = \begin{bmatrix} a_{11} & a_{12} & 0 & a_{14} & 0 \\ a_{21} & a_{22} & 0 & 0 & a_{25} \\ 0 & 0 & a_{33} & 0 & 0 \\ a_{41} & 0 & 0 & a_{44} & 0 \\ 0 & a_{52} & 0 & 0 & a_{55} \end{bmatrix} \quad (1)$$

Table 1: Full-sparse storing arrays

NE	1	2	3	4	5	6	7	8
DATA	a_{11}	a_{21}	a_{22}	a_{33}	a_{41}	a_{44}	a_{52}	a_{55}
JCOL	1	1	2	3	1	4	2	5
LINK	0	3	0	0	6	0	8	0
HEAD	1	2	4	5	7			

In this full-sparse database, all nonzero elements can be accessed conveniently. Basic dynamic operations are realized easily by simple searching, inserting, and deleting arithmetic. It is worth mentioning that the advantage of the proposed fully-sparse storing database is even significant for large-scale sparse matrix.

III. BI-CONJUGATE GRADIENT METHOD

Conventional iterative methods such as the conjugate gradient (CG) method [4] and the preconditioned conjugate gradient (PCG) method [5, 6] are based on real linear systems. When it comes to complex linear systems, new iterative methods are still open to be developed. In this section, a new method for solving symmetrical complex linear systems is proposed by regaining the basic concept of the bi-conjugate gradient method (BCG) for solving nonsymmetrical complex linear systems.

For symmetrical complex linear systems $Ax = b$, the modified BCG consists of the following steps:

Step 1: Set $i = 0$, input matrix $A \in C^{n \times n}$, vector $b \in C^n$, initial vector $x_i \in C^n$ and error criterion ε , compute $r_i = b - Ax_i$, $\hat{r}_i = r_i^*$, $p_i = r_i$, and $\hat{p}_i = \hat{r}_i$;

Step 2: Increase index i by 1 and calculate:

$$\begin{aligned} \alpha_i &= (\hat{r}_i, r_i) / (\hat{p}_i, Ap_i), \quad x_{i+1} = x_i + \alpha_i p_i, \\ r_{i+1} &= r_i - \alpha_i Ap_i, \quad \hat{r}_{i+1} = \hat{r}_i - \alpha_i^* A^* \hat{p}_i; \\ \beta_i &= (\hat{r}_{i+1}, r_{i+1}) / (\hat{r}_i, r_i), \quad p_{i+1} = r_{i+1} + \beta_i p_i, \\ \hat{p}_{i+1} &= \hat{r}_{i+1} + \beta_i^* \hat{p}_i; \end{aligned}$$

Step 3: Compare $\|r_{i+1}\| / \|b\|$ with ε , if $\|r_{i+1}\| / \|b\| < \varepsilon$, jump out from the loop and output x_{i+1} , otherwise, go to step 2.

Compared with the traditional CG method in the real number field, the modified BCG method has two advantages:

(1) It calculates only one matrix-vector product, not two like the CG method in each iteration.

(2) It converges about 5-6 times faster than the CG method.

IV. PRECONDITIONED BI-CONJUGATE GRADIENT METHOD

Preconditioned iterative methods [7] obtain the ability of solving linear systems accurately within a few iterations. For large-scale linear systems with symmetric system matrices, an efficient solving scheme is the preconditioned conjugate gradient (PCG) method. Traditional PCG methods are usually available for real linear systems, not for linear complex systems in FEM solution of electromagnetic scattering problems. Therefore, valid iterative methods for complex linear systems are needed. Based on a real preconditioned conjugate gradient algorithm, we design a complex preconditioned bi-conjugate gradient algorithm for solving complex linear systems. The details are as follows:

Step 1: Set $k = 0$, input complex matrix $A \in C^{n \times n}$, preconditioned matrix $M \in C^{n \times n}$, vector $b \in C^n$, initial vector $x_k \in C^n$ and error criterion ε , compute

$$r_k = b - Ax_k, z_k = M^{-1}r_k,$$

$$p_{k+1} = z_k, \hat{r}_k = r_k^*,$$

$$\hat{p}_{k+1} = p_{k+1}^*, \rho_k = (\hat{r}_k, z_k);$$

Step 2: Increase k by 1 and calculate:

$$w = Ap_k, \alpha_k = \rho_{k-1} / (\hat{p}_k, w),$$

$$x_k = x_{k-1} + \alpha_k p_k, r_k = r_{k-1} - \alpha_k w,$$

$$\hat{r}_k = r_{k-1}^* - \alpha_k^* A^* \hat{p}_k, z_k = M^{-1}r_k,$$

$$\rho_k = (\hat{r}_k, z_k), \beta_k = \rho_k / \rho_{k-1},$$

$$p_{k+1} = z_k + \beta_k p_k, \hat{p}_{k+1} = z_k^* + \beta_k^* \hat{p}_k;$$

Step 3: Compare $|\rho_k|$ with $|\rho_0|\varepsilon$, if $|\rho_k| > |\rho_0|\varepsilon$, jump out from the loop and output x_k , otherwise go to Step 2.

In iterations, the orthogonal vectors and Euclidean products are calculated with the preconditioned matrix M instead of matrix A because the preconditioned matrix M is well-conditioned and easy to be inverted.

V. A COMPLEX INCOMPLETE CHOLESKY FACTORIZATION PRECONDITIONER

The complex system matrix from FEM is always symmetric and sparse, so is the preconditioned matrix. In order that the preconditioned matrix M is easily inverted in simple storing structure, the sparse structure between matrix A and preconditioning matrix M should be the same or approximately the same. In some preconditioned methods [8-10], the sparse structure of preconditioning matrix M is designed by abandoning all possible non-diagonal filling elements (zero-filling mode) during the incomplete factorization. Considering that nonzero elements of preconditioning matrix M and matrix A can be stored in the same sparse database, the zero-filling Cholesky factorization method is used widely as an efficient preconditioner.

If a matrix $A \in C^{n \times n}$ is symmetric, its incomplete Cholesky factorization formula is written as

$$A = LL^T + R, \quad (2)$$

where the matrix L is a lower triangle matrix and matrix R is a residual matrix [11]. The matrix $M = LL^T$ is defined as a preconditioned matrix. During the incomplete Cholesky factorization, the filling elements of residual matrix R can be designed in advance, so it is easy to ensure the same sparse structure of matrix L as matrix A . As a well-condition approximate of matrix A , matrix M is the main driving factor for the rapid convergence of preconditioned iterative method.

Based on a real incomplete Cholesky factorization algorithm in [12], a complex incomplete Cholesky preconditioner is proposed by the zero-filling mode. During the complex incomplete Cholesky factorization, some diagonal elements are modified to possess the diagonal predomination of preconditioned matrix. The algorithm detail is expressed as follows.

Input system matrix $A = (a_{ij})_{n \times n} \in C^{n \times n}$ and output preconditioned matrix $M = LL^T$ (lower triangle matrix $L = (l_{ij})_{n \times n} \in C^{n \times n}$).

1. $l_{11} = \sqrt{a_{11}}$
2. For $i = 2$ to n do

3. If $|a_{i1}| \neq 0$ then $l_{i1} = a_{i1}/l_{11}$
4. End do
5. For $k = 2$ to n do
6. If $|a_{kk}| \geq \sum_{t=1}^{k-1} |g_{kt}|^2$ then $l_{kk} = \sqrt{a_{kk} - \sum_{t=1}^{k-1} |l_{kt}|^2}$,
 else $l_{kk} = a_{kk}$ (modifying diagonal elements)
7. For $i = k + 1$ to n do
8. If $|a_{ik}| \neq 0$ then $l_{ik} = \frac{1}{l_{kk}^*} (a_{ik} - \sum_{t=1}^{k-1} l_{it} l_{kt}^*)$
9. End do
10. End do

VI. NUMERICAL EXPERIMENTS

In this section, in order to verify the accuracy and efficiency of the proposed complex preconditioned bi-conjugate gradient algorithm, we implement the algorithm in eight classical experiments.

(1) 2-D scattering model of radar cover, 6-node curve triangle vector element, 6 unknowns in every element, 6532 unknowns in total.

(2) 2-D scattering model of aerofoil, 8-node curve quadrangle vector element, 8 unknowns in every element, 10442 unknowns in total.

(3) 3-D scattering model of nose, 10-node curve tetrahedron vector element, 20 unknowns in every element, 45228 unknowns in total.

(4) 3-D scattering model of rudder, 20-node curve hexahedron vector element, 54 unknowns in every element, 129812 unknowns in total.

(5) 3-D scattering model of elevator, 20-node curve hexahedron vector element, 54 unknowns in every element, 103236 unknowns in total.

(6) 3-D scattering model of leading edge, 8-node curve quadrangle shell vector element, 28 unknowns in every element, 51682 unknowns in total.

(7) 3-D scattering model of trailing edge, 8-node curve quadrangle shell vector element, 28 unknowns in every element, 46844 unknowns in total.

(8) 3-D penetrating model of radome, 20-node curve hexahedron vector element, 48 unknowns in every element, 87762 unknowns in total.

In Table 2, we show storing scales of system matrixes in the above numerical experiments by the fully-sparse storing scheme. The results suggest that the sparse proportion decreases

gradually with increasing the scale of system matrix. Therefore, the fully-sparse storing scheme profits the large-scale sparse matrix.

Table 2: Storage scale comparison

Ex	Unknowns	Nonzero elements stored	Sparse proportion (%)
1	6532	121430	2.846
2	10442	210874	1.934
3	45228	2544691	1.244
4	129812	11762106	0.698
5	103236	7684181	0.721
6	51682	2978082	1.115
7	46844	2701257	1.231
8	87762	6870334	0.892

Note: Sparse proportion is a ratio of nonzero elements stored in all elements.

In Table 3, we compare the computation efficiency of complex preconditioned bi-conjugate gradient (PBCG) method with other iterative methods. All complex linear systems are obtained from the above experiments. The results show that the proposed complex PBCG method converges with much fewer iterations and less time than other methods.

Table 3: Results of different methods ($\epsilon = 10^{-8}$)

Part I

Ex	CG		ILU		ICCG	
	iters	time	Iters	Time	iters	time
1	1711	27.63	1072	22.06	756	18.23
2	2048	39.45	1557	33.65	1369	30.28
3	7485	153.2	4555	119.3	3728	89.67
4	18772	526.3	11018	371.9	7952	250.4
5	15772	492.5	10774	327.8	6891	213.6
6	8764	177.1	5991	124.3	4012	101.3
7	8027	165.4	4799	121.1	3845	98.25
8	11344	346.8	8912	244.5	6679	194.5

Part II

Ex	BCG		PBCG	
	iters	time	iters	time
1	576	6.41	115	3.07
2	623	9.62	137	4.79
3	2564	28.77	208	6.25
4	6889	106.4	416	17.04
5	5742	98.82	389	15.88
6	2232	35.79	307	11.72
7	2116	33.14	295	10.98
8	4288	65.55	346	12.07

All results are computed with P4 3.0G CPU 512M-memory computer. All programs are developed in FORTRAN90 language.

VII. CONCLUSION

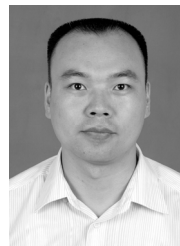
For the purposes of efficient data access and economic data storage in solving sparse linear systems, we proposed a fully-sparse storing scheme that stores only nonzero symmetrical elements. To accelerate the convergence of bi-conjugate gradient method, we developed the complex incomplete Cholesky factorization preconditioner that can improve the ill-condition system matrix. In view of its high efficiency on the large-scale complex linear systems, the complex PBCG method with fully-sparse storing scheme shows great promise as an ideal solver for large-scale electromagnetic computation.

ACKNOWLEDGMENT

This work was supported by Postdoctoral Science Foundation of China (W016312) and Science and Technology Innovation Foundation of Northwestern Polytechnical University (W016143).

REFERENCES

- [1] D. S. Kershaw, "The incomplete Cholesky conjugate gradient method for the iterative solution of systems of linear equation group," *J. of Comp. Phys.*, vol. 26, pp. 43-65, 1978.
- [2] I. S. Duff and G.A. Meurant, "The effect of ordering on preconditioned conjugate gradients," *BIT.*, vol. 29, no. 4, pp. 635-657, 1989.
- [3] J. W. Watts III., "A conjugate gradient truncated direct method for the iterative solution of the reservoir simulation pressure equation," *Society of Petroleum Engineer Journal*, vol. 21, no. 3, pp. 345-353, 1981.
- [4] Jin J M., *The Finite Element Method in Electromagnetics*, 2nd ed. Wiley, New York, 2002.
- [5] I. Arany, "Solving systems of elastic bar structures by preconditioned conjugate gradient method," *Computers Math. Applic.*, vol. 38, no. 9, pp. 125-134, 1999.
- [6] P. Saint-Georges, G. Warzee, R. Beauwens and Y. Notay, "High-performance PCG solvers for FEM structural analysis," *Int. J. for Numer. Meth. In Engng.*, vol. 39, pp. 1313-1340, 1996.
- [7] R. Beauwens and R. Wilmet, "Conditioning analysis of positive definite matrices by approximate factorizations," *J. Camp. and Appl. Math.*, vol. 26, no. 3, pp. 257-269, 1989.
- [8] R. Beauwens, "Modified incomplete factorization strategies," *Proceedings of a conference on Preconditioned conjugate gradient methods*, vol. 1, pp. 1-16. 1990.
- [9] Y. Notay, "DRIC: A dynamic version of RIC method. Numer," *Lin. Alg. with. Appl.*, vol. 1, no. 6, pp. 511-532, 1994.
- [10] R. Beauwens, "Iterative solution methods," *Applied numerical mathematics*, vol. 51, no. 4, pp. 437-450, 2004.
- [11] J. P. Wu and Z. H. Wang, "Problems and improvements to the incomplete Cholesky factorization with thresholds," *Journal on Numerical Methods and Computer Applications*, vol. 24, no. 3, pp. 207-214, 2003.
- [12] Y. J. Zhang and Q. Sun, "Improved ICCG method for large scale sparse linear equation group," *Journal of Computational Physics*, vol. 24, no. 4, pp. 581-584, 2007.



Y. J. Zhang received his degree in electromagnetics engineering and the Ph.D. degree from Northwestern Polytechnical University, Xi'an, China, in 2005 and 2009. Since 2006, he has been a senior lecturer at Aeronautics School of Northwestern Polytechnical University, China. He has coauthored more than 20 papers appearing in international journals and conferences. His current research interests include electromagnetic scattering computation and fast finite element methods.

Efficient Analysis Technique for Modeling Periodic Structures Based on Finite Element Method using High-Order Multiscale Functions

Adel Ben Ali, El Amjed Hajlaoui, and Ali Gharsallah

Unité de Recherche Circuits et Systèmes d'Electronique Haute Fréquence, Département de physique
Faculté des sciences de Tunis, 2092 El Manar, Tunis. Tunisia
adel.benali@laposte.net, hajlamjed@yahoo.fr, ali.gharsallah@fst.rnu.tn

Abstract- Periodic structures have a variety of important applications in electromagnetic engineering and modern technologies. Commonly used, periodic structures include frequency selective surfaces, optical gratings, phased array antennas and various metamaterials. A three-dimensional finite element method (FEM) with efficient boundaries conditions is presented to simulate the electromagnetic properties of homogeneous periodic material. In our approach, we describe an accurate and efficient numerical analysis based on high-order multiscale functions applied in vector edge FEM using new reduction meshing technique (MSRM-FEM) to characterize the electromagnetic properties of periodic structures. Here, we have achieved a factor of 4 in memory reduction and 7~11 in CPU speedup over the typical meshing. The FEM is applied to solve Maxwell's equation in the unit cell. The Floquet's theorem is used to take into account the periodicity of the boundaries conditions radiation for the unit cell. The numerical results are compared to published data and other simulation results. Good agreement is important to establish the validity and usefulness of the (MSRM-FEM) method given in this paper.

Index Terms- 3-D FEM, multiscale functions, periodic structures, reduction meshing.

I. INTRODUCTION

Periodic structures are important in the analysis of electromagnetics scattering and radiation for various engineering applications. The periodicity in geometry is often exploited to achieve some desired electromagnetic properties. Many microwave and optical devices, such as frequency selective structures (FSS) [1] and phased array antennas [2], fall into this category.

Analysis of periodic structures has been carried out using a variety of numerical methods, such as the finite difference time domain (FDTD), the moment method (MoM), the finite element method (FEM), the transmission line method (TLM), and iterative methods [3].

Among these methods, FEM excels the modelling of complex homogeneous and inhomogeneous structures geometries. The FEM is, also, able to incorporate different types of boundaries and different excitation modes without significantly affecting its formulation. The FEM modelling of periodic structures has been reported in literature for both scattering [4] and radiation analysis [5].

In our approach, we propose multiscale functions as basis functions to replace the traditional linear or higher order Lagrange, Hierarchical [6] interpolation shape functions in the finite-element formulation.

Since we employ multiscale functions in our modelling, a brief review is given here. More detailed theory and background of multiscale functions are presented in many references such as [7-8].

In this paper, we present a robust, higher-order multiscale functions combined with FEM method [9] to model infinitely periodic array-structures, by imposing appropriate radiation boundaries conditions and periodic boundaries conditions. The computational domain is confined to a single unit cell of the infinite array. The unit cell interior region is discretized with regular tetrahedral element to model its geometry.

When the structures contain many unit cells, the structure extends to infinity in the periodic direction as illustrated in Fig. 1.

This purpose is to greatly simplify the electromagnetic analysis and minimize the CPU time of simulation by enabling the characterization of the electromagnetic interaction with the entire structure. Here, we will use a new strategy meshing for the regular design applied in microwave structures when we use the edge element formulation.

A new mesh-truncated technique is introduced for the frequency domain solution of closed and open region scattering problems

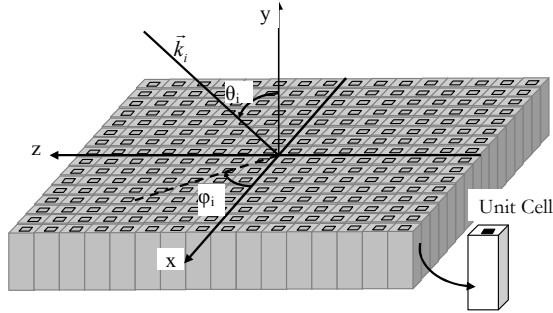


Fig. 1. Graphical representation of a plan wave incident on a generic 3-D periodic structure.

II. MULTISCALETS FUNCTIONS

Basic theory of orthogonal multiwavelets, multi-resolutions, and multiscalets can be found in many mathematical papers, e.g. [7] and [8].

The multiscalets $\phi_0(t), \phi_1(t) \dots \phi_{r-1}(t)$, are polynomials of degree $2r-1$ on $[0, 1]$ and zero elsewhere, with $r-1$ continuous derivatives. In electromagnetics, the order is usually ≤ 4 . They satisfy

$$\Phi(n) = \delta_{1,n} I, \quad (1)$$

where $\delta_{m,n}$ is the Kronecker delta, I is the identity matrix of size $r \times r$, r is the multiplicity coefficient, and

$$\Phi(t) = \begin{bmatrix} \phi_0(t) & \dots & \phi_0^{(r-1)}(t) \\ \vdots & \ddots & \vdots \\ \phi_{r-1}(t) & \dots & \phi_{r-1}^{(r-1)}(t) \end{bmatrix}. \quad (2)$$

The column vector

$$\varphi(t) = (\varphi_0(t) \dots \varphi_{r-1}(t))^T. \quad (3)$$

For all r , satisfies that $\phi_j(t) \neq 0$ only on two intervals $[0, 1]$ and $[1, 2]$. The function values and its $(r-1)$ derivatives are specified at each integer edge. If $\varphi_j(t)$ is defined on $[0, 2]$, then they are alternatively symmetric and anti-symmetric about $t = 1$.

The dilation equation may be written as

$$\begin{aligned} \phi(t) &= \sum_k C_k \phi(2t-k) \\ &= C_0 \phi(2t) + C_1 \phi(2t-1) + C_2 \phi(2t-2) \end{aligned} \quad (4)$$

Since the support is $[0, 2]$, the only nonzero coefficients are C_0, C_1 , and C_2 , there are r basis functions at each edge, and C_i are matrices of $r \times r$ ($i = 0, 1, 2$).

The polynomials of degree $2r-1$ on $[0, 1]$ and $[1, 2]$ are determined by:

$$\left(\frac{d}{dt}\right)^k \phi_j(1) = \delta_{k,j}, \quad k, j = 0, \dots, r-1 \quad (5)$$

$$\left(\frac{d}{dt}\right)^k \phi_j(0) = \left(\frac{d}{dt}\right)^k \phi_j(2) = 0, \quad k, j = 0, \dots, r-1$$

From (1), we define

$$\phi(1) = \begin{bmatrix} \phi_0(1) & \phi_0^{(1)}(1) & \dots & \phi_0^{(r-1)}(1) \\ \phi_1(1) & \phi_1^{(1)}(1) & \dots & \phi_1^{(r-1)}(1) \\ \vdots & \vdots & \ddots & \vdots \\ \phi_{r-1}(1) & \phi_{r-1}^{(1)}(1) & \dots & \phi_{r-1}^{(r-1)}(1) \end{bmatrix} = I. \quad (6)$$

Explicitly, it appears that $\phi_0(t)$ interpolates at the sampling point $t=1$, but assumes 0 at other sampling points $t=0$. The derivatives $\phi_0^{(k)}(t)$, $k=1, 2, \dots, r-1$ are zero at all integer sampling points. Similarly, interpolates at integer point, but assumes zero elsewhere for any derivatives other than 1.

In general,

$$\varphi_i^{(j)}(m) = \delta_{i,j} \delta_{1,m}, \quad i, j = 0, 1, \dots, r-1. \quad (7)$$

While spline interpolation fits a set of function values by solving a coupled linear system [8], the property (7) of the multiscalets provides interpolation that is completely uncoupled. Here, $\phi_i(t)$, $i=0, 1, \dots, r-1$ will be employed in the finite element as the shape functions.

The matrix coefficients in (4) can be derived by the following procedure:

$$\begin{aligned} C_0 &= \Phi\left(\frac{1}{2}\right)\Lambda, \\ C_1 &= \Phi(1)\Lambda = I\Lambda, \\ C_2 &= \Phi\left(\frac{3}{2}\right)\Lambda \end{aligned} \quad (8)$$

where

$$\Lambda = \text{diag}\left\{1, \frac{1}{2}, \left(\frac{1}{2}\right)^2, \dots, \left(\frac{1}{2}\right)^{r-1}\right\}. \quad (9)$$

Matrices C_0 and C_2 related by

$$C_0 = SC_2S^{-1}, \quad (10)$$

with

$$S = S^{-1} = \text{diag}\{1, (-1), \dots, (-1)^{r-1}\}. \quad (11)$$

The Matrix C_2 is given by

$$C_2 = U^{-1}\Gamma U \quad (12)$$

$$\Gamma = \text{diag}\left\{\left(\frac{1}{2}\right)^r, \left(\frac{1}{2}\right)^{r+1}, \dots, \left(\frac{1}{2}\right)^{2r-1}\right\}, \quad (13)$$

and

$$U_{mn} = (-1)^{r+m+n} \frac{(r+m-1)!}{(r+m-n)!}. \quad (14)$$

The multiscalets $\phi_0(t)$ and $\phi_1(t)$ are polynomials of degree $2r-1$ can be built by a simple iteration program or an eigenvalue algorithm called the cascade method from the dilatation matrices C_i [7]. In general multiscalets with arbitrary r have the form

$$\begin{cases} \phi_0(t) = a_{1,1}t^{2r-1} + a_{1,2}t^{2r-2} + \dots + a_{1,r}t^r \\ \dots = \dots \\ \dots = \dots \\ \phi_{r-1}(t) = a_{r,1}t^{2r-1} + a_{r,2}t^{2r-2} + \dots + a_{r,r}t^r \end{cases} \quad (15)$$

$$\{\varphi\} = [A]\{T\},$$

where the coefficient $a_{i,j}$ are obtained by inverting the matrix whose entries are

$$[B] \Rightarrow b(i,j) = \frac{(2r-i)!}{(2r-i-j+1)!}, \quad i, j = 1, 2, \dots, r \quad (16)$$

where

$$[A] = [B]^{-1}. \quad (17)$$

It was found that for $r=2$,

$$t \in [0,1] \begin{cases} \phi_0(t) = 3t^2 - 2t^3 \\ \phi_1(t) = t^3 - t^2 \end{cases}. \quad (18)$$

In case $r=3$, the explicit polynomial of $\phi_0(t)$, $\phi_1(t)$ and $\phi_2(t)$ are

$$\begin{cases} \phi_0(t) = 6t^5 - 15t^4 + 10t^3 \\ \phi_1(t) = -3t^5 + 7t^4 - 4t^3 \\ \phi_2(t) = \frac{1}{2}t^5 - t^4 + \frac{1}{2}t^3 \end{cases}. \quad (19)$$

III. FEM FORMULATION

A. Discretization

The boundary value problem in the full-wave analysis of an inhomogeneous field waveguide is defined by the vector wave equation in the 3-D waveguide problem, [9, 10].

Maxwell's equations for the electromagnetic fields inside the computation domain are:

$$\begin{aligned} \nabla \times E &= -j\omega\mu_0\varepsilon_r H \\ \nabla \times H &= j\omega\mu_0\varepsilon_r E + J \end{aligned} \quad (20)$$

Here, we eliminate H in the two equations above results in the wave equation for E :

$$\nabla \times \left(\frac{1}{\mu_r} \nabla \times E \right) - k_0^2 \varepsilon_r E = -jk_0 Z_0 J. \quad (21)$$

Assuming that E satisfies some boundaries conditions on the surface S enclosing the computation domain Ω , it can be shown that the original problem is equivalent to the following variational problem

$$\delta F(E) = 0, \quad (22)$$

where

$$\begin{aligned} F(E) &= \frac{1}{2} \iiint_V \left[\frac{1}{\mu_r} (\nabla \times E) \cdot (\nabla \times E) - k_0^2 \varepsilon_r E \cdot E \right] d\Omega \\ &+ jk_0 Z_0 \iiint_V E \cdot J d\Omega + \text{Surface Integral Terms}. \end{aligned} \quad (23)$$

The surface integral terms are the results of corresponding boundaries conditions [11].

To solve the variational problem (23), the entire computation domain Ω is divided into small elements. In the FEM discretization, commonly used elements are tetrahedral elements for 3-D problems.

The next step involves expanding the electromagnetic fields in terms of basis functions in each element. In the context of 3-D problems, it is more convenient to use vector basis functions instead of scalar basis functions.

For tetrahedral elements, the edge basis function associated with the i_{th} edge is given by

$$N_i^e = (L_i^e \nabla L_j^e - L_j^e \nabla L_i^e) / l_{ij} \quad (24)$$

$$L_i^e = \frac{1}{6V^e} (a_i^e + b_i^e x + c_i^e y + d_i^e z).$$

Further, L_k^e ($k = 1, 2, 3, 4$) are the basis node of basis functions associated with the four vertices of the tetrahedral, where a_i^e, b_i^e, c_i^e , and d_i^e are defined as in [9], and i_1 and i_2 denote the two vertices associated with the i_{th} edge and l_i^e is the length of the i_{th} edge.

In this paper, we will replace the traditional functions given in (24) by the multiscalets interpolation functions with multiplicity $r=3$

$$\begin{aligned} W_{i1}^e &= (-3N_1^5 + 7N_1^4 - 4N_1^3)^e l_1^e, \\ W_{i2}^e &= (-3N_2^5 + 7N_2^4 - 4N_2^3)^e l_2^e, \\ W_{i3}^e &= (-3N_3^5 + 7N_3^4 - 4N_3^3)^e l_3^e, \\ W_{i4}^e &= (-3N_4^5 + 7N_4^4 - 4N_4^3)^e l_4^e, \\ W_{i5}^e &= (-3N_5^5 + 7N_5^4 - 4N_5^3)^e l_5^e, \\ W_{i6}^e &= (-3N_6^5 + 7N_6^4 - 4N_6^3)^e l_6^e \end{aligned} \quad (25)$$

It can be demonstrated that W_i^e satisfies automatically the convergence condition.

Once the basis functions are determined, the electric (or magnetic) field within each element can be expanded as

$$E = \sum_{j=1}^m E_j^e W_j^e, \quad (26)$$

where m is the number of interpolating points (depending on the order of basis functions) within each element (in this case $m=6$). Substituting (26) into (23) and applying Galerkin's method, the following matrix equation for each tetrahedron is derived.

$$\{[K^e] - k_0^2 [M^e]\} \{E^e\} = -jk_0 Z_0 \{F^e\}, \quad (27)$$

where

$$\begin{aligned} K_{ij}^e &= \frac{1}{\mu_r} \iiint_{V^e} (\nabla \times W_i^e) \cdot (\nabla \times W_j^e) d\Omega \\ M_{ij}^e &= \varepsilon_r \iiint_{V^e} W_i^e \cdot W_j^e d\Omega \\ F_i^e &= \iiint_{V^e} W_i^e J d\Omega. \end{aligned} \quad (28)$$

Corresponding to all tetrahedral, a global matrix equation of the following form can be derived:

$$[A](E) = (F), \quad (29)$$

where

$$\begin{aligned} [A] &= \sum_{e=1}^M ([K^e] - k_0^2 [M^e]) \\ (E) &= \sum_{e=1}^M (E^e) \\ (F) &= -jk_0 Z_0 \sum_{e=1}^M (F^e), \end{aligned} \quad (30)$$

and M is the total number of tetrahedral. The FEM mass matrix $[A]$ is symmetric, positive with an order n , where n is the total number of edges in the whole domain Ω and (F) is an appropriate excitation vector which has non-zero elements only in the position of excitation edges.

The final matrix equation is of very large order but the corresponding square matrix is sparse. For that, we can use of appropriate iterative conjugate gradient (CG) techniques.

B. Boundaries conditions

Let us consider the unit cell in an infinite periodic structure, as shown in Figure 2; the interior volume, denoted here as V , is enclosed by four side surfaces: a top surface, and a bottom surface. It may contain arbitrary dielectric and conducting structures.

The four side surfaces S_{x1} , S_{x2} , S_{z1} , and S_{z2} are located at $x = 0$; $x = Dx$; $z = 0$, and $z = Dz$, respectively, where Dx and Dz are periodic lengths in the x and z directions. The top surface S_t is the interface between free-space and the unit cell region. The bottom surface S_b is usually a ground plane. It may also contain waveguide apertures S_w that provide excitation for the radiation case. In a general configuration, 4 kinds of boundaries conditions are involved. On the four side surfaces, periodic boundaries conditions are imposed, relating the fields on the opposite side surfaces. On the top surface, a periodic radiation boundary condition is imposed; it simulates the radiation towards the free space in the presence of an infinite array. If a waveguide is present in the structure, a waveguide port condition is imposed on S_w . Finally, on conducting surfaces, a perfectly electrically conducting (PEC) boundary condition is enforced explicitly as a homogeneous Dirichlet boundary condition.

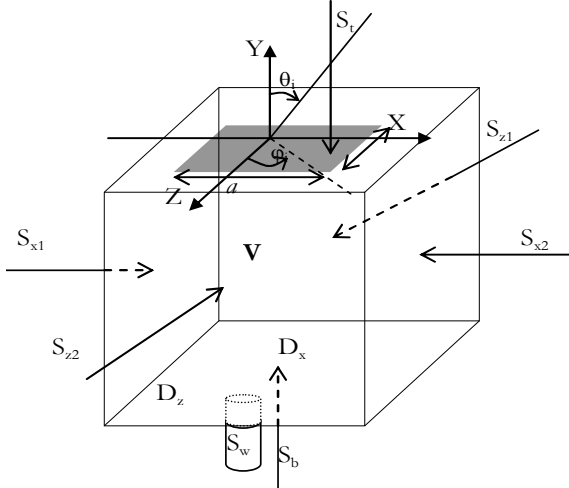


Fig. 2. The unit cell used for FEM calculations of periodic structures along with the locations of the various truncation boundaries where either absorbing or periodic boundaries conditions are imposed.

Periodic boundaries conditions can be derived directly from the Floquet theorem [13]. In accordance with the Floquet theorem, the electromagnetic fields inside and above the periodic media should satisfy

$$E(x + mD_x, z + nD_z) = E(x, z)e^{j(mk_x D_x + nk_z D_z)} \quad (31)$$

$$H(x + mD_x, z + nD_z) = H(x, z)e^{j(mk_x D_x + nk_z D_z)}, \quad (32)$$

where

$$k_{x_i} = k_0 \sin \theta_i \cos \varphi_i \quad (33)$$

$$k_{z_i} = k_0 \sin \theta_i \sin \varphi_i, \quad (34)$$

where (θ_i, φ_i) are the incident and scan angles. The periodicity forces the incident energy to propagate along certain directions. These propagation modes are defined analytically in the top surface S_t by the following equations:

$\Delta E_i - k_y^2 E_i = 0$ with $k_y = (\epsilon_h \mu_h)^{1/2} \omega$ with h is the correspondent space area.

To facilitate the implementation of periodic boundaries conditions, identical surface meshes are created on the opposite side surfaces. Then, for each unknown E_i on one side surface, a corresponding unknown E_j is identified on the opposite surface which has the same relative position as E_i .

By applying the Floquet theorem (31), we obtain the following relationship between E_i and E_j :

$$E_j = E_i e^{j\psi_{ij}}, \quad (35)$$

where ψ_{ij} is a phase shift term given by

$$\psi_{ij} \begin{cases} k_{x_i} D_x & \forall E_i \in S_{x1}, E_j \in S_{x2} \\ k_{z_i} D_z & \forall E_i \in S_{z1}, E_j \in S_{z2} \\ k_{x_i} D_x + k_{z_i} D_z & \forall E_i \in S_{x1} \cap S_{z1}, E_j \in S_{x2} \cap S_{z2} \end{cases} \quad (36)$$

In the matrix context, (35) is enforced explicitly as an inhomogeneous Dirichlet boundary condition. That's why, for each unknown pair $(E_i; E_j)$: E_j is eliminated; the matrix entries associated with E_i are modified as plane is placed on S_t .

$$K_{ii} = K_{ii} + K_{ji} e^{j\psi_{ij}}, \quad (37)$$

For all $E_i \notin S_{x2} \cup S_{z2}$, and

$$K_{ik} = K_{ik} + K_{jl} e^{j(\psi_{ij} - \psi_{kl})}, \quad (38)$$

For all $E_i \in S_{x2} \cup S_{z2}$ which is related to E_k by phase shift ψ_{kl} , and finally, the right-hand-side (RHS) vector entry associated with E_i is modified as

$$F_i = F_i + F_j e^{j\psi_{ij}}, \quad (39)$$

The function (23) contains a surface integral term over the top surface S_t with a form given by

$$S(E) = \iint_{S_t} \left[\frac{\gamma_e}{2} (\hat{n} \times E) \cdot (\hat{n} \times E) + E \cdot U \right] dS, \quad (40)$$

where U which may be expressed as

$$U = \frac{1}{\mu_r} \hat{n} (\nabla \times E) + \gamma_e \hat{n} \times (\hat{n} \times E). \quad (41)$$

γ_e is known parameter given by $\gamma_e = -\frac{jk_0 \mu_r}{\eta}$, with $\eta = \sqrt{\mu_r / \epsilon_r}$.

IV. REDUCTION MESHING

Our refinement scheme described in Fig. 3 and the coarse grid tetrahedron is split into four tetrahedral which are similar to their parent and one different tetrahedral in the center.

Hence, our refinement procedure results in only two classes of similar tetrahedral, assuming that mesh quality will never deteriorate. The idea is to eliminate four tetrahedral to surround with the cubic element and to leave only the central tetrahedral.

This technique of meshing used to adapt FEM method with other numerical method like the TLM method, iterative method etc. in case of a hybridization technique, where we convert the value of every edge elements to at point (Fig. 4. d). With this technique, we can superpose a

resulting matrix of these numerical methods with our of FEM matrix to obtain the value in inner waveguide.

In the next figure, we present the different steps to get our appropriate and desired meshing based on the strategy given by Fig. 3.

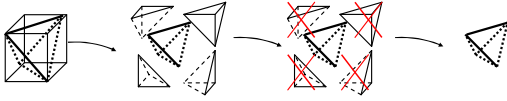


Fig. 3. Element Hexahedral subdivided into five tetrahedral with elimination of the secondary tetrahedral.

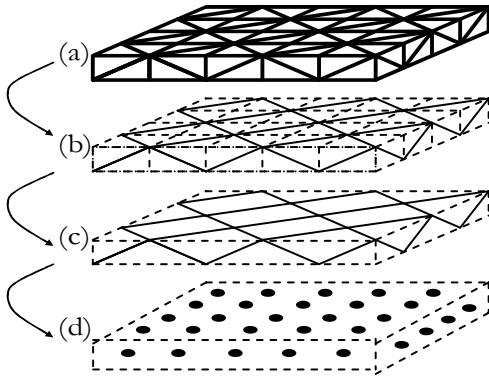


Fig. 4. A waveguide devised in tetrahedral elements where only a center tetrahedral is needed.

The next table presents the efficiency technique to reduce the size of a regular structure, and presents the reduction report between the typical meshing and reduction meshing and another table that presents gain obtained in time considering proper characteristics of the used machine.

Table 1: Reduction report between typical meshing and reduction meshing

Cells Number	Typical Meshes	Reduction Meshes	Reduction Report
16×1×16	2433 edges	1056 edges	≈ 44%
32×1×32	9473 edges	4160 edges	
64×1×64	37377 edges	16512 edges	
128×1×128	148481 edges	65792 edges	

Table 2: Time report between typical and new reduction meshing for different size matrix with a CPU 3 GHz and 4 GB of memory

CPU	Memory	Number of Cells	Time (sec) for 10 iterations		Time (sec) between typical and new meshing
			Typical Meshing	New Meshing	
3 GHz	4Go	16×1×16	16	1,4	11,42
		32×1×32	96	10,2	9,41
		64×1×64	868	97	8,95
		128×1×128	9223	1321	6,98

This purpose will greatly simplify the electromagnetic analysis of the CPU time of second simulation by enabling the characterization of the electromagnetic interaction with the entire structure.

V. NUMERICAL RESULTS

This section contains a series of examples that validate the MSRM-FEM formulation compared with analytic and reference results. Our strategy is based on a unit cell divided on $32\Delta x \times 4\Delta y \times 32\Delta z$ elements. All given examples were studied and carried out with a gain of 4 in memory consumption.

In this part, we consider the finite element analysis in the two-dimensional xz -plane. Although not a physically realistic configuration, the infinite array model provides a reasonably good approximation to the performance of the interior elements in a large finite array. Here, we suppose that this finite unit cell, the patch characterized by its infinite thin thickness is inserted between two dielectric layers that have the same dielectric permittivity.

To show that the periodic boundaries conditions and periodic radiation boundaries conditions are correctly modeling the field behaviour, a simple example is tested. We use a 20 cm thick uniform dielectric layer composed of dielectric with relative permittivity $\epsilon_r=2.2-j$ and backed with a ground plane. The analysis takes into account different oblique incidences. It proves clearly that the reflection coefficient is independent of both angle and polarization of incidence.

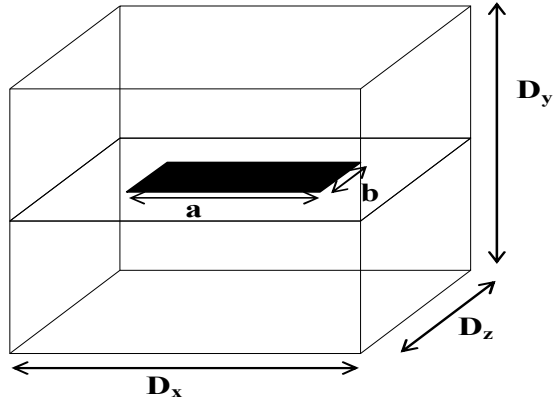
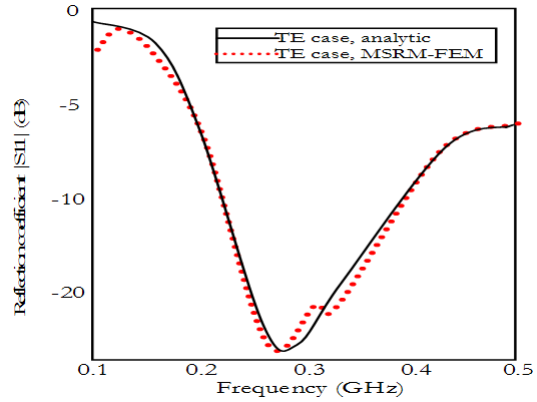


Fig. 5. Rectangular patch unit cell laid between two dielectric.

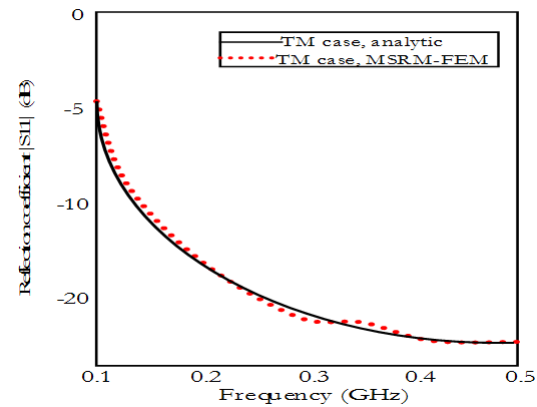
Here, for an incident plane wave with an incident angle $\theta = 60^\circ$, the TE and the TM reflection coefficients, shown in Fig. 5, are calculated over the frequency band 0.1 to 0.5 GHz. In the FEM, the unit cell is modeled as a $20 \times 20 \times 20$ cm homogeneous dielectric box with a ground plane placed on its bottom surface. Good agreement between our MSRM-FEM results and the analytical solutions has to validate considered in the periodic boundary conditions and the periodic radiation boundary conditions.

The dielectric slab is backed by a ground plane. The reflection coefficient should always have magnitude of 1 because all the energy shall be reflected. In our example, it has a few differences with the analytic results. This is due to the intrinsic properties of the used dielectric characterized by its proper properties. In another way, this is not a perfect dielectric characterized by a complex permittivity ($\epsilon_r = 2.2 - j$).

The next example is the reflection due to an incident upon a plane wave onto a frequency selective surface structure. The unit cell presented in Fig. 5 is a rectangular patch laid between two dielectric with 2-mm-thick with a complex permittivity $\epsilon_r = 2.2 - j$, and following geometric dimensions $D_x = D_z = 10.0$ mm, $D_y = 2.0$ mm, $a = 2.5$ mm and $b = 5$ mm.



(a)



(b)

Fig. 6. Reflection coefficient for the 20-cm-thick uniform layer ($\epsilon_r = 2.2$) backed with ground plane at $\theta = 60^\circ$ and $\phi = 0$ for (a) TE, (b) TM.

The normalised power reflection coefficient for an oblique incidence is shown in Fig. 7. It is compared with the analytic results given by the advanced design system (ADS 2004) simulator.

The second example (Fig. 8) presents the normalised transmitted power coefficient for a real permittivity ($\epsilon_r = 4$) and following geometric dimensions $D_x = 50.0$ mm, $D_z = 4.0$ mm, $a = D_x/2$ and $b = D_z$. The unit cell is presented in Figure 5. This 3-D structure is simulated using MSRM-FEM FORTRAN code, and compared with FDTD reference solution [13].

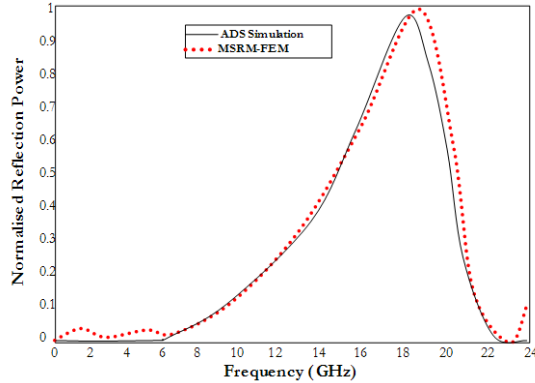


Fig. 7. The normalised power reflection coefficient with side view unit cell, for an oblique incidence.

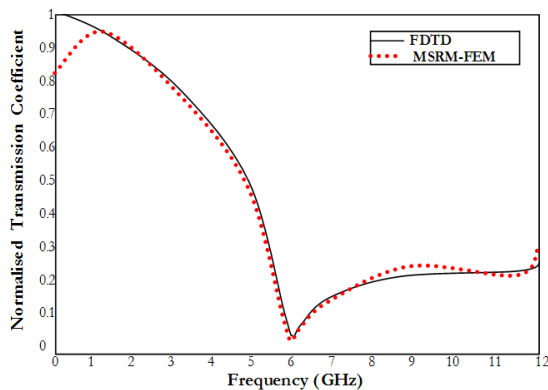


Fig. 8. The normalised power transmission coefficient with side view unit cell, for an oblique incidence $(\theta, \varphi)=(90^\circ, 0^\circ)$.

The incident angle ($theta = 90$ degrees) shows a grazing incidence. Here, very high absorption of energy was shown at the resonant frequency 6 GHz.

Figure 9 shows the normalised transmission power as a function of the frequency, for several values of a . The computed values are indicated with symbols, and intermediate values have been obtained using multiscalelets interpolation.

In all cases, a significant absorption band is observed. In addition, the critical frequency (frequency in which value attains its minimum) decreases as the ratio a/D increases.

For a real permittivity ($\epsilon_r=10.2$) and following geometric dimensions $D_x=D_z=10\text{mm}$, $D_y=2.0$ mm, $a=b=1.0, 4.0$ and 8.0 mm.

Figure 10 presents the normalised transmission power as a function of the frequency, for several

values of incident angle θ . These results show that the critical frequency value depends very weakly on the incidence angle.

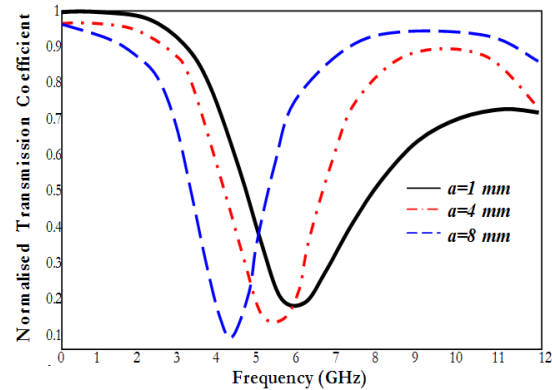


Fig. 9. The normalised power transmission coefficient for various values of the plat's size: for an oblique incidence $(\theta, \varphi)=(90^\circ, 0^\circ)$.

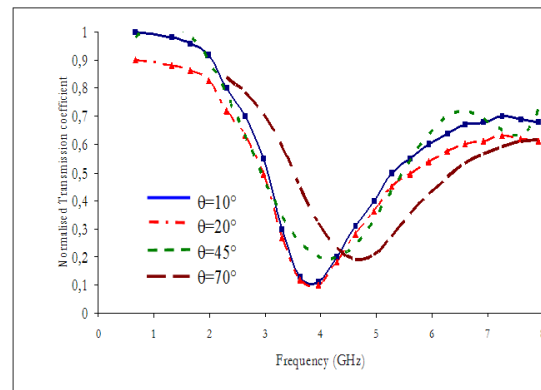


Fig. 10. The normalised transmission coefficient as a function of the incident frequency, for various values of incident angle: $\theta = 10^\circ, 20^\circ, 45^\circ$ and 70° . The period $D_x=D_z = 10.0$ mm, $D_y=2.0$ mm and the plate's size a are kept fixed $a = 8.0$ mm and $\epsilon_r=10.2$.

VI. CONCLUSION

In our paper, a new FEM analysis of infinite periodic structures described by MSRM-FEM is presented. The theoretical basis of FEM theory, combined with the Floquet theorem and the integral equation formulation analysed with new technical meshing strategy is presented. Higher-order multiscalelets vector basis functions are used to expand electromagnetic fields. Numerical results have demonstrated the efficiency and

accuracy of using higher order multiscalets vector basis functions.

The reduction meshing (RM) based technique is combined with FEM to reduce the size of resulting matrix, consequently, minimization of memory and time consumption, 7~11 in time speed compared with typical meshing.

The FEM feed modeling is, also, discussed in detail in radiation problem cases. The validity and versatility of the FEM formulation have been demonstrated through numerical results compared with analytic and published simulations.

REFERENCES

- [1] R. Mittra, C. H. Chan, and T. Cwik, "Techniques for analyzing frequency selective surfaces," *Proc. IEEE*, vol. 76, pp. 1593–1615, Dec. 1988.
- [2] N. Amitay, V. Galindo, and C. P. Wu, *Theory and Analysis of Phased Array Antennas*, New York: Wiley, 1972.
- [3] Daniel G. Swanson, Jr and Wolfgang J. R. , *Microwave Circuit Modeling Using Electromagnetic Field Simulation*, Artech House, Inc., 2003.
- [4] J. L. Volakis, T. F. Eibert, D. S. Filipovic, Y. E. Erdemli, and E. Topsakal, "Hybrid finite element methods for array and FSS analysis using multiresolution elements and fast integral techniques," *Electromagn.*, vol. 22, pp. 297-313, May-Jun 2002.
- [5] J. M. Jin and J. L. Volakis, "Scattering and radiation analysis of three-dimensional cavity array via a hybrid finite-element method," *IEEE Trans. Antennas Propagat.*, vol. 41, pp. 1580-1586, Nov. 1993.
- [6] G. Pan, *Wavelet in Electromagnetics and Device Modeling*, Hoboken, NJ: Wiley, 2003.
- [7] Y. Zhu and A.C Cangellary "Hierarchical Multilevel Potential Preconditioner for Fast Finite-Element Analysis of Microwave Devices," *IEEE Trans. Microwave Theory and Tech.*, vol. 50, no. 8, pp. 1984-1989, Aug. 2002.
- [8] W. Miller, "Introduction to the Mathematics of Wavelets," *Lecture Notes and Background Materials for Math 5467*, May 7, 2004.
- [9] J. Jin, *The Finite Element Method in Electromagnetics*, New York , Wiley 2002.
- [10] M. L. Barton and Z. Cendes "New Vector Finite Element for Three-Dimensional Magnetic Field Computation," *Journal. Appl. Phys.*, vol. 61, no. 8, pp. 3919-3921, April 1987.
- [11] Y. Zhu and R. Lee, "TVFEM Analysis of Periodic Structures for Radiation and Scattering," *Progress In Electromagnetics Research*, vol. 25, pp. 1–22, 2000.
- [12] V. Hill, O. Farle and R. Dyczij-Edlinger "A Stabilized Multilevel Vector Finite Element Solver for Time-harmonic Electromagnetic Waves," *IEEE Transaction on Magnetic.*, vol. 39, no. 39, pp. 1203-1207, May 2003.
- [13] E. A. Navarro, B. Gimeno, and J.L. Cruz, "Modelling of periodic structures using the finite difference time domain method combined with the Floquet theorem," *Electronics Letters*, vol. 29, no.5, March 1993.



Adel Ben Ali received the degree in electronic engineering in 1999 and the M.Sc. degree in communications systems from ELManar University- National Engineering School Tunis, Tunisia, in 2002. He is currently working toward the Ph.D. degree in electrical engineering. His research interests include analysis of microwave structures, microwave integrated circuits by finite element method



El Amjed Hajlaoui received the degree in electronic engineering in 2001 and the M.Sc. degree and Ph.D. in communications systems from ELManar University- National Engineering School Tunis, Tunisia, respectively, in 2003 and 2008. His research interests include multilayered structures, microwave integrated circuits, and quasi-optic structures.



Ali Gharsallah received the degrees in radio-electrical engineering from the Ecole Supérieure de Télécommunication de Tunis in 1986 and the Ph.D. degree in 1994 from the Ecole d'Ingénieurs de Tunis. Since 1991, he was with the department of Physics at the Faculty of Sciences, Tunis. His current research interests include antennas, multilayered structures and microwave integrated circuits.

Equivalent Circuits for Nonuniform Transmission Line Simulation

Jacek Izydorczyk

Institute of Electronics
Silesian University of Technology, Akademicka 16, 44-100 Gliwice, Poland
jacek.izydorczyk@ieee.org

Abstract—The hereby article is devoted to elaboration of the analysis method of nonuniform transmission line (NUTL) with utilization of typical circuit simulator like SPICE. It is assumed that quasi-TEM modes are propagated in the NUTL. Solution of the problem is divided into three parts. 1) The analysis of nonuniform transmission line is reduced to the analysis of cascaded sections of linear varied nonuniform transmission line (LNLT). Proper algorithm originates from literature. 2) Computational model of linear varied nonuniform transmission line is elaborated following the asymptotic waveform evaluation methodology. The q -pole model is matched to imitate position of zeros and poles of admittance matrix of the NUTL. 3) Synthesis of passive circuit which implements the model for broad range values of LNLT slope constant. Consequently parameters of the circuit can be evaluated precisely as polynomial function of slope constant. Resultant model can be easily written in SPICE simulation language.

Index Terms—Asymptotic waveform evaluation, nonuniform transmission line, PR function, SPICE.

I. INTRODUCTION

Rapid development of VLSI technology yields large chips powered by a faster and faster external clock. Electrical length of interconnections becomes a significant fraction of a wavelength. Consequently conventional lumped-impedance models lead to a great computing complexity. There were many calculation models and techniques for real transmission lines that soften this problem. Most of them are focused on VLSI metal interconnections and connections between integrated circuits [1]. Unfortunately none of them can be easily implemented in a circuit simulator.

Strongly nonuniform transmission lines are used in microwave filters and impedance match circuits [6], to form impulse and to process quick-change signals [7]. Therefore, much attention has been paid to them [8], in recent times.

In this article, a new method of nonuniform transmission line (NUTL) simulation is proposed. The NUTL is divided into chunks approximated by lossless linear varied nonuniform transmission line (LNLT). For each approximating chunk an analytical solution of equations, which describes approximating LNLT is known. The solution is converted into SPICE acceptable macro-model [13] by methodology patterned on asymptotic waveform evaluation (AWE). In the original AWE method, initial conditions and a few first moments of the transient are matched with q -pole model. Herein a q -pole model is matched to imitate position and residues of poles and zeros of the admittance matrix of the LNLT. Proposed approximation methodology leads to the simulation model which is equivalent to a simple reciprocal circuit. Consequently, chunks of considerable length LNLT can be modeled with a low order ladder circuit. The model can be easily written in SPICE simulation language.

II. ANALYSIS OF NUTL

Text of this paragraph is quoted from [24] for completeness and smoothness of considerations. Consider ideal linear varied nonuniform transmission line (LNLT). Its wave impedance and propagation constant are:

$$Z(\xi) = Z_0(1 + k\xi), \quad \beta = \omega / c, \quad (1)$$

where Z_0 is a wave impedance in the beginning of the line, $k=(dZ(\xi)/d\xi)/Z_0$ is the slope constant, ξ is the position along the line, c is the phase speed of electromagnetic waves in the line, ω is the angular frequency of the waves. Solution of the telegraph equation for LNLT can be easily found in the

literature. For example in [26], the solution was found and elements of ABCD matrix have been given explicitly. Here the admittance matrix of LNTL line is used:

$$y_{11} = \frac{j}{Z_0} \cdot \frac{-J_0(x)Y_1(x(1+k\ell)) + J_1(x(1+k\ell))Y_0(x)}{J_1(x(1+k\ell))Y_1(x) - J_1(x)Y_1(x(1+k\ell))} \quad (2)$$

$$y_{12} = y_{21} = \frac{-2 \cdot j/x(1+k\ell) / Z_0\pi}{\left[J_1(x(1+k\ell))Y_1(x) - J_1(x)Y_1(x(1+k\ell)) \right]} \quad (3)$$

$$y_{22} = \frac{j/(1+k\ell)}{Z_0} \cdot \frac{-J_0(x(1+k\ell))Y_1(x) + J_1(x)Y_0(x(1+k\ell))}{J_1(x(1+k\ell))Y_1(x) - J_1(x)Y_1(x(1+k\ell))} \quad (4)$$

where $J_n(x)$, $Y_n(x)$, are the Bessel function of the first and second kind of order n respectively; ℓ is the length of the line; $x = \omega\tau / k\ell$ and τ is delay time of the line and $j = \sqrt{-1}$. Using the solution, the following algorithm of NUTL analysis was formulated by K. Lu [26]. The algorithm is quoted here *in extenso*.

Step 1) "Numerically evaluate $y = \int_0^\xi d\xi / c(\xi)$.

Step 2) Select a set of points $(\xi_0, \xi_1, \dots, \xi_i, \dots, \xi_n)$ (corresponding to a set of points in terms of $y(\xi)$ $(y_0, y_1, \dots, y_i, \dots, y_n)$ in the region $0 \leq \xi \leq \ell$) so the NUTL is broken to small n sections. The $Z_c(y)$ of the i -th small section can be approximated by an LNTL:

$$Z_c(y) \approx \hat{Z}_c(y) = Z_c(y_i) [1 + k_i(y - y_i)], \quad (5)$$

$$\text{where } k_i = \frac{Z_c(y_{i+1}) - Z_c(y_i)}{Z_c(y_i)(y_{i+1} - y_i)}, \quad (6)$$

and $i = 0, 1, 2, \dots, n$

Step 3) Evaluate the ABCD matrix $[A^{i-th}]$ of the i -th section by using $\ell_i = y_{i+1} - y_i$, k_i , $Z_c(y_i)$ in place of ℓ , k , and Z_0 in (2)-(4).

Step 4) Evaluate the ABCD matrix $[A^{Total}]$ by cascading the $[A^{i-th}]$ for all small sections.

$$[A^{Total}] = \prod_{i=0}^n [A^{i-th}] \quad (7)$$

Step 5) After $[A^{Total}]$ is obtained, the S, Z, or Y parameters can be calculated by using matrix conversion."

The algorithm is biased by three drawbacks:

- The solution of telegraph equations is given in terms of the Fourier transform. Time domain solution needs one more step i.e. inverted Fourier transform. Practically only numerical approximation can be obtained by the means of FFT algorithm.
- The algorithm cannot be used directly to simulate nonlinear networks – that fact depreciates the value of the algorithm when simulation of digital circuits is considered.
- It cannot be implemented directly in circuit simulator for example in SPICE.

To alleviate these problems AWE approximation of LNTL chunks is considered in the next section.

III. LNTL ADMITTANCE MATRIX APPROXIMATION

Each formula (2)-(4) is approximated by rational function:

$$y_{ij} \approx \hat{y}_{ij} = \frac{a_0^{(ij)}}{x} + \sum_{n=1}^N \left(\frac{a_n^{(ij)}}{x - p_n} + \frac{a_n^{(ij)}}{x + p_n} \right), \quad (8)$$

where p_n are poles of y_{ij} numbered in ascending absolute value order and $a_n^{(ij)}$ is residue of y_{ij} at the pole p_n . Poles of all four admittance parameters of LNTL are the same and can be computed numerically as the solution of the equation:

$$J_1(x(1+k\ell))Y_1(x) - J_1(x)Y_1(x(1+k\ell)) = 0. \quad (9)$$

It is worth searching for the solution of the equation from the approximated value of the pole, which can be derived using approximation of the Bessel functions by trigonometric ones [30]:

$$p_n \approx \frac{n \cdot \pi}{k\ell}, \quad \text{where } n = \pm 1, \pm 2, \pm 3, \dots \quad (10)$$

The exact solution is obtained by the Newton-Raphson method. Residue $a_n^{(ij)}$ of y_{12} and y_{21} at poles p_n can be determined quite easily using the following formulae [33]:

$$a_n^{(12)} = a_n^{(21)} = \frac{-2j}{Z_0 \cdot \pi \cdot p_n (1+k\ell) M'(p_n, k\ell)}, \quad (11)$$

where $M'(x, k\ell)$ is derivative of left side of (9):

$$\begin{aligned}
M'(x, k\ell) = & J_2(x)Y_1(x(1+k\ell)) \\
& - Y_2(x)J_1(x(1+k\ell)) \\
& + (1+k\ell)J_1(x)Y_2(x(1+k\ell)) \\
& - (1+k\ell)Y_1(x)J_2(x(1+k\ell)).
\end{aligned} \quad (12)$$

In case of parameters y_{12} and y_{21} , a simple cut of rational series expansion of (3) gives good results. A rational series expansion of (2) and (4) is also possible. Residue of y_{11} and y_{22} at poles p_n can be determined using the following equations:

$$a_n^{(11)} = \frac{[J_0(p_n)Y_1(p_n(1+k\ell)) - Y_0(p_n)J_1(p_n(1+k\ell))]}{j \cdot Z_0 \cdot M'(p_n, k\ell)}, \quad (13)$$

$$a_n^{(22)} = \frac{[Y_1(p_n)J_0(p_n(1+k\ell)) - J_1(p_n)Y_0(p_n(1+k\ell))]}{j \cdot Z_0 \cdot M'(p_n, k\ell)}. \quad (14)$$

Unfortunately, the rational approximation (8) obtained by the restriction of rational series expansion of (2) and (4) to first $N+1$ terms poorly approximate exact relations (2) and (4) in low frequency domain. A better idea is to find numerically, zeroes $x_n^{(11)}$ of y_{11} :

$$J_0(x)Y_1(x(1+k\ell)) - J_1(x(1+k\ell))Y_0(x) = 0 \quad (15)$$

and zeroes $x_n^{(22)}$ of y_{22} :

$$J_0(x(1+k\ell))Y_1(x) - J_1(x)Y_0(x(1+k\ell)) = 0. \quad (16)$$

In both cases, the approximate solution is:

$$x_n^{(11)} = x_n^{(22)} = \frac{n \cdot \pi + \pi / 2}{k\ell}, \quad (17)$$

where $n = 0, \pm 1, \pm 2, \pm 3, \dots$. The solution can be used to speed up the numerical search for an exact solution of (15) and (16). The goal is to obtain the approximation (8) by reproducing the exact location of first $2N+1$ poles and $2N$ zeroes of (2) and (4) respectively:

$$y_{ii} \approx \hat{y}_{ii} = Y_{ii} \frac{\prod_{n=1}^N (x - x_n^{(ii)}) (x + x_n^{(ii)})}{x \cdot \prod_{n=1}^N (x - p_n) (x + p_n)}. \quad (18)$$

Unknown parameter Y_{ii} should be chosen to reproduce the exact value of residuum $a_0^{(ii)}$ at pole $p_0=0$:

$$a_0^{(11)} = a_0^{(22)} = \frac{2j}{k\ell \cdot (2+k\ell)}. \quad (19)$$

This guarantees that the approximation (8) is accurate in the range of frequencies up to the last pole p_N . Formula for parameter Y_{ii} is as follows:

$$Y_{ii} = \frac{2j}{k\ell \cdot (2+k\ell)} \cdot \frac{\prod_{n=1}^N (p_n)^2}{\prod_{n=1}^N (x_n^{(ii)})^2}. \quad (20)$$

This way, we have an approximation of admittance parameters of linear varied nonuniform transmission line. The approximation consists of four formulas of the type (8). In case of parameters y_{12} and y_{21} residues are computed using (11). In case of y_{11} and y_{22} residues are computed as follows:

$$a_n^{(ii)} = \frac{j \cdot \prod_{m=1}^N |p_m|^2 \cdot \prod_{m=1}^N (p_m^2 + |x_m^{(ii)}|^2)}{p_n^2 (2+k\ell) k\ell \prod_{m=1}^N |x_m^{(ii)}|^2 \prod_{\substack{m=1 \\ m \neq n}}^N (p_m^2 - p_n^2)}. \quad (21)$$

The approximation circuit consists of four active circuits. Order of the whole circuit is four times higher than the order of the rational function used to approximate each individual parameter y_{ij} . Let us consider input admittance Y_{in} of the approximation circuit matched at the output:

$$Y_{in} = \frac{\hat{y}_{11} - Z_0(1+k\ell) \cdot (\hat{y}_{12}\hat{y}_{21} - \hat{y}_{11}\hat{y}_{22})}{1 + \hat{y}_{22}Z_0(1+k\ell)}. \quad (22)$$

The function is a rational function of frequency. Order of the function is $(2N+2)$ where N is the number of pole pairs taken into account in the formula (8). To obtain circuit of the order $2N+1$ determinant:

$$\Delta = \hat{y}_{12}\hat{y}_{21} - \hat{y}_{11}\hat{y}_{22} \quad (23)$$

could not possess poles of multiplicity two. Consequently, the relationship:

$$a_n^{(11)} a_n^{(22)} - (a_n^{(12)})^2 = 0 \quad \text{for } n=0, 1, \dots, N \quad (24)$$

must be fulfilled. Relationship (24) is true if we use (11), (13), and (14). But, when formulas (21), (11), and (22) are used to compute residues, then it is false.

IV. PASSIVE MODEL

Now the goal is to obtain an approximation circuit which is:

- as accurate as possible;
- order of the circuit should be $2N+1$ where N is the number of pole pairs taken into account in the formula (8);
- passive - to assure stability of every one model which contains the model of the nonuniform transmission line.

The conditions for a network with an admittance matrix $[y_{ij}(s)]$ to be passive are [14]:

1. $y_{ij}^*(s) = y_{ij}(s^*)$ for each pair ij (“*” is complex conjugate operator).
2. $[y_{ij}(s)]$ is a positive real (PR) matrix, i.e., the product $(\mathbf{z}^T)^* ([y_{ij}^*(s)]^T + [y_{ij}(s)]) \mathbf{z} \geq 0$ for all complex values of s with $\text{Re}(s) > 0$ and any arbitrary vector \mathbf{z} .

The first condition is satisfied whenever conjugate complex poles (zeros) are selected to create the model. The second condition is then equivalent to that all eigenvalues of $\text{Re}([y_{ij}(j\omega)])$ are greater than zero for $\omega \in \mathfrak{R} \cup \{\pm\infty\}$ [22]. Ensuring that condition is usually a challenging task because of all variations of Padé approximation are notoriously non-passive. Literature gives some ideas of how to reinforce passivity for models obtained by rational approximation of frequency domain responses and do not lose accuracy of approximation [14], and [16]. Nevertheless the model considered herein is free of such problems. Method of order reduction not only slightly enhances model accuracy but does not violate intrinsic model passivity. Therefore, it is sufficient to check passivity of the resulting model.

The idea of model order reduction is to slightly correct residuum $a_n^{(12)}$, computed by (11), and residues $a_n^{(11)}$ and $a_n^{(22)}$, computed by (21), to fulfill (24):

$$\hat{a}_n^{(11)} = a \cdot a_n^{(11)}, \hat{a}_n^{(22)} = b \cdot a_n^{(22)}, \hat{a}_n^{(12)} = c \cdot a_n^{(12)} \quad (25)$$

$$a \cdot b = \alpha^2 c^2 \quad \text{where} \quad \alpha^2 = \frac{(a_n^{(12)})^2}{a_n^{(11)} \cdot a_n^{(22)}}. \quad (26)$$

Correction coefficients a , b , and c should be as close to one as possible. For example, Euclidean distance should be as low as possible:

$$I(a, b, c) = (a - 1)^2 + (b - 1)^2 + (c - 1)^2. \quad (27)$$

Minimization of (27) with constraint (26) gives the solution:

$$a = \alpha \frac{1 + 2|\alpha|}{1 + 2\alpha^2} = b, \quad (28)$$

$$c = \frac{1 + 2|\alpha|}{1 + 2\alpha^2}. \quad (29)$$

After correction of residues, the input admittance Y_{in} of the approximation circuit is a rational function of order $2N+1$.

Passivity of the model can be assured by the checking of passivity criteria for the input impedance (22). A real rational function is the driving-point immittance of a linear, passive, lumped, reciprocal, and time one-port network if, and only if, it is a positive real. This condition can be formulated as the following theorem, cited from [23]:

Theorem 1. A rational function represented in the form

$$F(s) = \frac{P(s)}{Q(s)} = \frac{m_1(s) + n_1(s)}{m_2(s) + n_2(s)}, \quad (30)$$

where $m_1(s)$, $m_2(s)$ and $n_1(s)$, $n_2(s)$ are even and odd parts of the polynomials $P(s)$ and $Q(s)$, respectively, is positive real if, and only if, the following conditions are satisfied:

1. $F(s)$ is real when s is real;
2. $P(s) + Q(s)$ is strictly Hurwitz (zeroes lie on open left-hand plane);
- 3.

$$M(s^2) \Big|_{s=j\omega} = m_1(j\omega)m_2(j\omega) - n_1(j\omega)n_2(j\omega) \geq 0 \text{ for all } \omega.$$

The first condition is enforced by choosing of conjugate complex poles (zeros) of the model. The second condition can be checked by factorization of $P(s) + Q(s)$. The third condition can be reformulated in a much convenient form following [23]:

Theorem 2. If $M(s^2)$ is an even polynomial of a complex variable s with real coefficients and $M(0) > 0$ and $M(s)$ does not possess real negative roots then $M(s^2) \Big|_{s=j\omega} > 0$ for all ω .

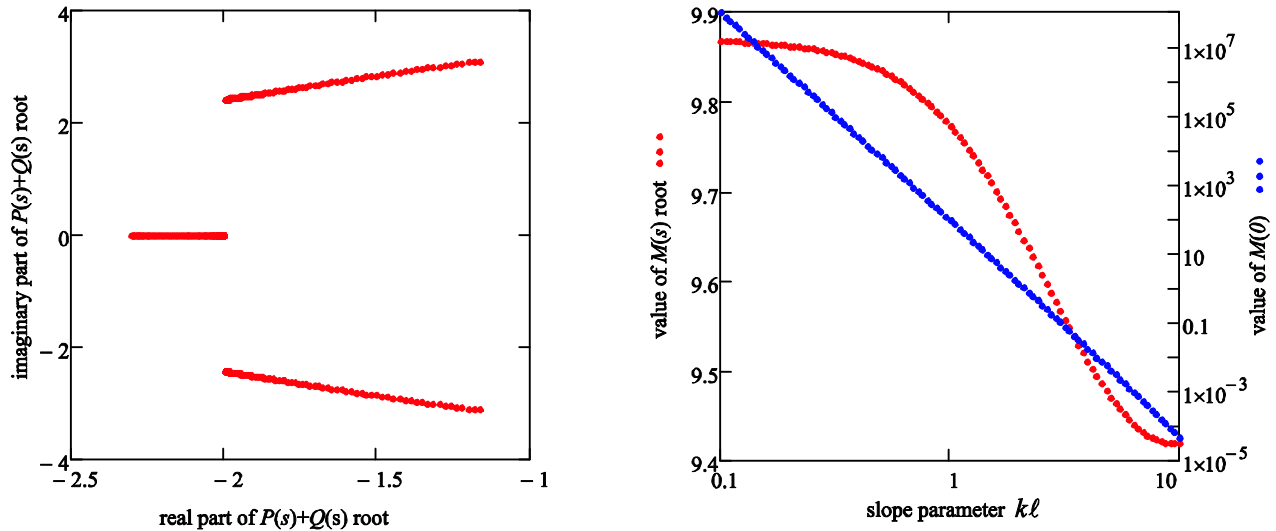


Fig. 1. Passivity check for third order model of LNTL: a) real vs. imaginary part of $P(s)+Q(s)$ roots; b) root of $M(s)$ (multiplicity two) and value $M(0)$.

Results of factoring polynomials $P(s)+Q(s)$ $M(s)$ and values $M(0)$ for the model of LNTL with parameter $N=1$ (third order) are shown in Fig.1. Factorization was performed for the value of the slope parameter kl lying in the range of 0.1 to 10. Polynomial $M(s)$ is a second order polynomial with only one root of multiplicity two. Each time the model passivity conditions are met.

Therefore, the admittance Y_{in} can be synthesized using Darlington methodology [34]. The synthesis algorithm is summarized in Appendix I. The algorithm is based on $Z=1/Y_{in}$ – input impedance of matched reciprocal circuit. For $N=1$, the result of the synthesis is particularly simple. The circuit approximating LNTL consists of inductance connected in series with Darlington C-type section – see Fig. 2. The synthesis has been conducted for normalized linear varied nonuniform transmission line described by parameter kl varied in relatively wide range from 0.1 to 10. The number of synthesized circuits was 100. For each of the inductance L_n , $n=1,3,4$; and for capacity C_2 , a discrete set of values was obtained depending on slope parameter kl . These values are arranged along the regression curves. Each inductance of the model depends on slope parameter kl almost linearly whereas variation of capacity C_2 can be estimated by rational function of second order. Consequently, a simple passive

approximation circuit can be formed. Inductances and capacitance of the subcircuit can be computed using the following equations:

$$L_1 = Z_0 \tau (6259 + (1152 - 6.943 \cdot kl) \cdot kl) \cdot 10^{-5}, \quad (31)$$

$$C_2 = \frac{\tau}{Z_0} \cdot \frac{(-0.4735 \cdot kl - 22.34) \cdot kl + 51.23}{(-11.13 \cdot kl + 1) \cdot kl + 51.27}, \quad (32)$$

$$L_3 = Z_0 \tau (3494 + (3188 + 8.580 \cdot kl) \cdot kl) \cdot 10^{-4}, \quad (33)$$

$$L_4 = Z_0 \tau (28796 + (3361 - 3.24 \cdot kl) \cdot kl) \cdot 10^{-5}. \quad (34)$$

Other configurations of the third order ($N=1$) lumped circuit, which models a section of the linear varied transmission line are discussed in [24].

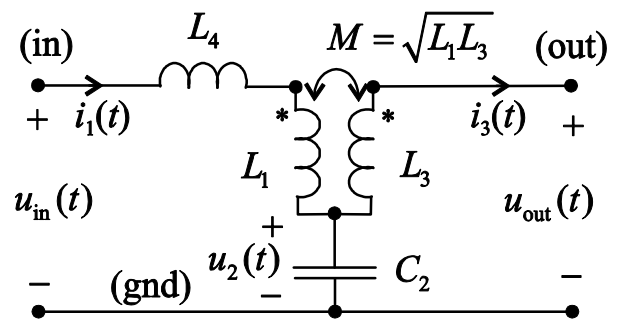


Fig. 2. Passive circuit, which models a segment of the linear varied nonuniform transmission line.

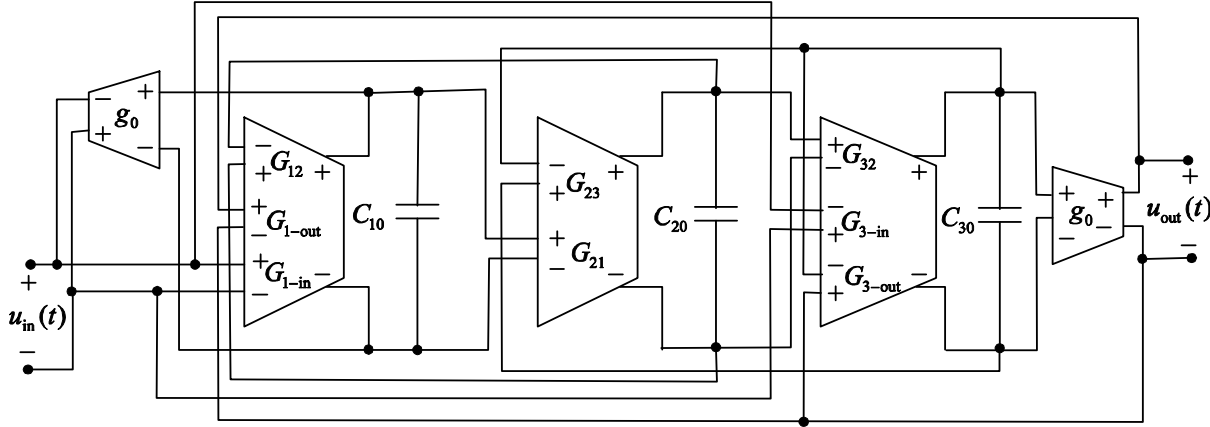


Fig. 3. Active circuit, which models a segment of the linear varied nonuniform transmission line.

Table 1: Transconductances of the active circuit modeling LNTL

Parameter	Expression
G_{12}	$\frac{(L_3 + \sqrt{L_1 \cdot L_3}) \cdot C_1}{L_3 \cdot L_4 \cdot g_0}$
G_{1-in}	$\frac{C_1}{L_4 \cdot g_0}$
G_{1-out}	$\frac{C_1 \cdot \sqrt{L_1 \cdot L_3}}{L_3 \cdot L_4 \cdot g_0}$
$G_{21} = G_{23}$	$\frac{C_2' \cdot g_0}{C_2}$
G_{32}	$\frac{(\sqrt{L_1 \cdot L_3} + L_1 + L_4) \cdot C_3}{L_3 \cdot L_4 \cdot g_0}$
G_{3-in}	$\frac{(\sqrt{L_1 \cdot L_3}) \cdot C_3}{L_3 \cdot L_4 \cdot g_0}$
G_{3-out}	$\frac{(L_1 + L_4) \cdot C_3}{L_3 \cdot L_4 \cdot g_0}$
g_0	an arbitrary value

V. SPICE MODEL

The passive circuit shown in Fig. 2 can be easily described in the SPICE simulation language. A convenient form of the description is a subcircuit. Values of inductance and capacitance, which compose the network, should be determined by the parameters passed to the subcircuit. If the used simulator has a preprocessor, that allows calculating the value of the subcircuit parameters

before analysis, then this task is relatively easy. Example of the model implementation in the form of subcircuit attributed by parameters, in the SPICE simulator environment, was presented in [24].

This article presents a concept of the model implementation, which does not require the involvement of the preprocessor. Many versions of SPICE, including many of those that come from the Berkeley version Spice3f, e.g. Ngspice program, does not have a preprocessor and does not allow user to define parameters. In this situation, parameters can be passed to subcircuit only in the form of voltages (currents) defined outside of the subcircuit. Voltages can easily modify the value of current sources – voltage controlled current sources. Much more difficult is to achieve the effect of modification of the capacity or inductance. As shown in the article [27], it is not impossible, but quite inconvenient. The technique proposed here is based on simulation of an analog computer, which is modeling a passive circuit from Fig. 2. Differential equations in normal form describing the circuit have the form:

$$\begin{bmatrix} \dot{u}_1(t) \\ \dot{u}_2(t) \\ \dot{u}_3(t) \end{bmatrix} = \begin{bmatrix} 0 & -\frac{T_3 + \sqrt{T_1 \cdot T_3}}{T_3 \cdot T_4} & 0 \\ \frac{1}{T_2} & 0 & -\frac{1}{T_2} \\ 0 & \frac{\sqrt{T_1 \cdot T_3} + T_1 + T_4}{T_3 \cdot T_4} & 0 \end{bmatrix} \begin{bmatrix} u_1(t) \\ u_2(t) \\ u_3(t) \end{bmatrix} +$$

Table 2: SPICE description of the active circuit modeling LNTL

```

.subckt xmachine.00 in gnd out gnd tau inz0 kL
*interface for parameters passing
Rtau tau tau2 10
vtau tau2 0 dc 0
rz0 inz0 0 1meg
rkL kL 0 1meg
*circuit reactances computing
VL1 100 0 dc 0
BL1 0 100 i=0.062591+(0.011523-6.942533e-5*v(kL,0))*v(kL,0)
VL3 200 0 dc 0
BL3 0 200 i=0.34938+(0.318778+8.58005e-4*v(kL,0))*v(kL,0)
VL4 300 0 dc 0
BL4 0 300 i=0.287957+(0.033614-3.240502e-5*v(kL,0))*v(kL,0)
VC2 400 0 dc 0
BC2 0 400 i=((-0.47351*v(kL,0)-22.34105)*v(kL,0)+51.22673)/((-
11.12705*v(kL,0)+1)*v(kL,0)+51.27397)
*analog computer
c10 1 gnd 20pF
c20 2 gnd 20pF
c30 3 gnd 20pF
b10 gnd 1 i=(1/i(VL4)*V(in,gnd)-
(i(VL3)+sqrt(i(VL1)*i(VL3)))/i(VL3)/i(VL4)*V(2,gnd)+sqrt(i(VL1)*i(VL3))/i(VL3)/i(VL4)*
b20 gnd 2 i=(1/i(VC2)*V(1,gnd)-1/i(VC2)*V(3,gnd))/i(vtau)*v(inz0)/250e
b30 gnd 3 i=(-sqrt(i(VL1)*i(VL3))/i(VL3)/i(VL4)*V(in,gnd)+
(sqrt(i(VL1)*i(VL3))+i(VL1)+i(VL4))/i(VL3)/i(VL4)*V(2,gnd)-
(i(VL1)+i(VL4))/i(VL3)/i(VL4)*V(out,gnd))/i(vtau)/v(inz0)
g1in in gnd 1 gnd 0.02
g2out gnd out 3 gnd 0.02
.ends

```

$$+ \begin{bmatrix} \frac{1}{T_4} & \frac{\sqrt{T_1 \cdot T_3}}{T_3 \cdot T_4} \\ 0 & 0 \\ -\frac{\sqrt{T_1 \cdot T_3}}{T_3 \cdot T_4} & -\frac{T_1 + T_4}{T_3 \cdot T_4} \end{bmatrix} \begin{bmatrix} u_{in}(t) \\ u_{out}(t) \end{bmatrix}, \quad (35)$$

where $\dot{u}_n(t)$ is time derivative of voltage $u_n(t)$ for $n=1,2,3$, $T_n = g_0 L_n$ for $n=1,3,4$, and $T_2 = C_2/g_0$. g_0 is an arbitrarily assumed value of trans-

conductance, while $u_1(t) = i_1(t)/g_0$ and $u_2(t) = i_2(t)/g_0$ are voltages derived from loop currents $i_1(t)$ and $i_2(t)$ marked in Fig. 2.

System of equations (35) can be realized in the form of the active circuit shown in Fig. 3. The circuit follows a typical active OTA filter based on "leapfrog" structure, though is not identical with the filter [28]. State variables are voltages on capacitors C_1 - C_3 . Relations between state variables, resulting from equations (35), are implemented by transconductances which value depends on three additional input voltages. The

Table 3: SPICE description of LNTL two segment model

```

.subckt xmachine.01 in gnd out gnd intau inz ink1x1.02 in
    gnd 2 gnd intau inz ink11 xmachine.00x2.02 2 gnd
    out gnd intau inz2 ink12 xmachine.00rk1 ink1 0
    1kbz2 inz2 0 v=v(inz,0)*(1+v(ink1,0)/2)bk11 ink11 0
        v=v(ink1,0)/2bk12 ink12 0
        v=v(ink1,0)/(2+v(ink1,0)).ends
    
```

parameters given in this way, modify the properties of the model by specifying a delay τ , wave impedance Z_0 , and slope parameter $k\ell$ of the line. The equations describing the individual transconductances are summarized in Table 1. In a case of typical OTA-based structure of “leapfrog” filter is enough to simulate an LC ladder biased by resistances [29]. Network from Fig. 3 can interact with any biasing system. State variables corresponding to the currents are transformed by the voltage-controlled current sources into corresponding currents actually observed at the ports of the network. As a result, such networks can be connected in a series to form the model of linearly varied transmission line of arbitrarily large order.

SPICE description of the circuit implementing the model in Fig. 3 is shown in Table 2. Input port of subcircuit named **xmachine.00** is between nodes **in** and **gnd**. Output port is between nodes **out** and **gnd**. Wave impedance of the line near the input port is equal Z_0 . Wave impedance of the line near the output port is equal $Z_0(1+k\ell)$. To obtain the appropriate circuit delay the current source should be inserted between the node **tau** and the ground (node number 0). Value of the source expressed in amperes should be equal to the line delay, expressed in nanoseconds. For example, if the line delay is intended to be 1ps, the current value generated by the source should be 1mA. Potential of **inz0** node (expressed in volts) defines the line impedance. Potential of **kl** node (expressed in volts) determines the slope parameter $k\ell$ of the transmission line. Only positive values of the slope parameter are valid.

VI. SIMULATIONS

Using third order circuit in Fig. 3, one could build LNTL model of arbitrarily high order. The idea is to use algorithm invented by K. Lu [26] and presented in section II. The LNTL is divided into small sections; each modeled using the circuit of Fig. 3. Admittance parameters of each section are reproduced by the model in wide range of frequencies. In particular, the mutual interaction of neighboring line segments is reproduced closely. The structure of the circuit causes, that mutually-far segments interact with each other poorly. As a result, it is expected that combining cascade circuits allows effective enhancement of model’s accuracy.

Table 3 shows how to declare a model of LNTL consisting of two segments of equal delay using SPICE simulation language. The first segment of the transmission line has a slope parameter equal to $k\ell/2$, where $k\ell$ is a slope parameter of entire LNTL. Input wave impedance of the first segment is Z_0 . The delay of this and the next segment is equal to $\tau/2$, where τ is a total delay of the LNTL. The appropriate value for this parameter is obtained by combining the **tau** nodes of both circuits and supplying an external source of current which defines total delay τ . The second segment is replaced by the circuit attributed by slope parameter $k\ell/(2+k\ell)$. Input impedance of the segment is equal $Z_0/(1+k\ell/2)$. By means of only ten subcircuits, similar to those in Table 3, one comes to the model of LNTL which consists of 1024 segments.

In order to examine the accuracy of the LNTL multi-segment model, the simulation experiment was conducted. The simulated circuit is

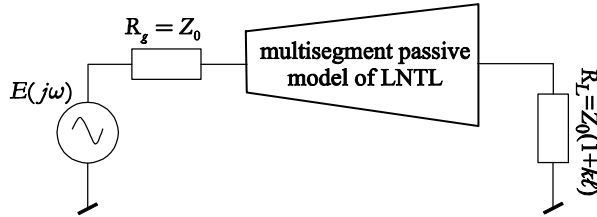


Fig. 4. Circuit used in simulation experiment for examination of LNTL model accuracy.

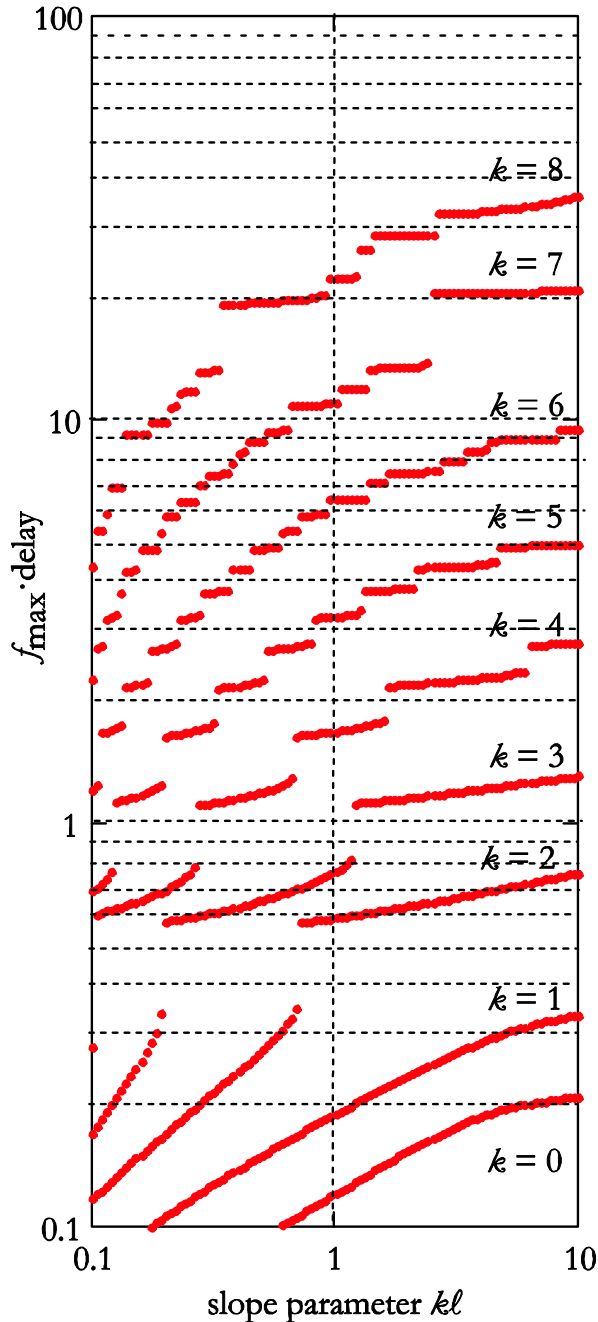


Fig. 5. Maximal frequency of the multi-segment LNTL model.

presented in Fig. 4. The input source (loading resistance) was matched to input (output) wave impedance of LNTL. The number of third order sections, LNTL model consists of, varied from 1 to 256. In each step of the experiment, the number of sections was doubled. In the experiment, the reflection coefficient of the input port $S_{11}(\omega)$ and the reflection coefficient of the output port $S_{22}(\omega)$ were studied. It was assumed, that input impedance of modeled transmission line is 50Ω , whereas delay of the line equal to 1ns. The line slope parameter $k\ell$ has changed in the range of 0.1 to 10. The frequency response of the simulation model $S'_{nn}(\omega)$, where $n=1, 2$, was compared with the response $S_{nn}(\omega)$ obtained on the basis of analytical equations (2)-(4). This allowed to determine limit frequency f_{max} , for each of the tested models, above which the relative deviation of the model reflection coefficient differs greater than 5% from the reflection coefficient determined analytically:

$$\max_{0 \leq \omega \leq 2\pi f_{max}} \left| \frac{S_{nn}(\omega) - S'_{nn}(\omega)}{S_{nn}(0)} \right| \leq 0.05. \quad (36)$$

We examined models consisting of sections, whose number K amounted to:

$$K = 2^k \quad \text{where } k=0,1,\dots,8. \quad (37)$$

Data for the SPICE program was prepared automatically, using an application written in LabVIEW[®] graphical language, due to the large number of test simulations. The results of the frequency domain analysis are shown in Fig. 5. The horizontal axis bears slope parameter $k\ell$ of the LNTL. The vertical axis bears the product of the maximal frequency f_{max} and line delay. The set of curves is parameterized by variable k determining number of sections, which the model comprises. Figure 5 shows that the frequency range in which the model truly reflects the properties of the reflection coefficient is proportional to the number of sections used. The model is better when the transmission line is more nonuniform. This is successful information. The proposed model is useful wherever there is a line that shows high non-uniformity at a short distance compared to the line delay.

A circuit similar to the circuit presented in Fig. 4 was used to determine time complexity of

computations with model of the LNTL line. In this case, the linear varied transmission line described

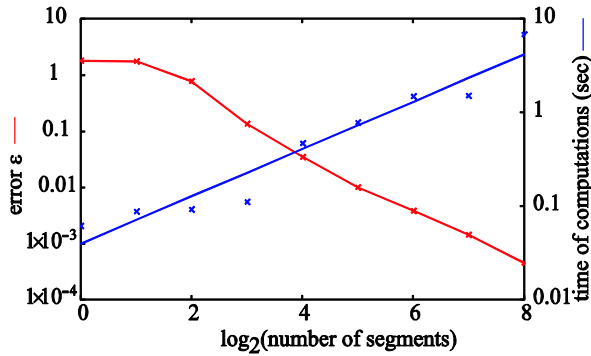


Fig. 6. Time domain error and time of computations versus number of third order segments the LNTL model consists of.

by the slope parameter $k\ell=10$ was used. The input port was excited by the time domain impulse rather than AC source. The impulse has shape of “raised cosine”:

$$e(t) = \frac{A}{2} \begin{cases} 1 - \cos(4\pi t / \tau) & \text{for } 0 \leq t \leq \tau/2 \\ 0 & \text{otherwise} \end{cases}, \quad (38)$$

where amplitude of the impulse was $A=1\text{V}$ and $\tau=1\text{ns}$ was the line delay. Duration of the impulse was equal to half of the line delay. The simulation objective was to obtain reflected wave from the input port in time range 0 to 2τ . Accuracy of the time domain simulation was determined by comparison of reflected wave $u'(t)$ computed by

SPICE, with the reflected wave $u(t)$ computed using analytical formulas (2)-(4). Error of the computations:

$$\varepsilon = \frac{\max_{0 \leq t \leq 2\tau} |u'(t) - u(t)|}{\max_{0 \leq t \leq 2\tau} |u(t)|}, \quad (39)$$

as a function of the LNTL model sections number is presented in Fig. 6. The latter figure, also, shows time of computations on a 2.5 GHz PC computer. The model, which consists of 16 segments gives error less than 4% , whereas computation time is no longer than 500ms.

VII. MEASUREMENTS

In order to verify the algorithm by experiment, the reflection coefficient of the input port $S_{11}(\omega)$ of nonuniform, asymmetric PCB stripline was measured. The transmission line under investigation was implemented on a conventional two-side epoxy-glass laminate. Thickness of the laminate dielectric layer is $h=1.5\text{mm}$. Copper foil thickness amount to $t=35\mu\text{m}$. Relative permittivity of the laminate dielectric layer is equal to $\varepsilon_p=4.2$. Line width varies continuously from 2.9 mm by 0.6 mm to 8.1 mm – see Fig. 7. The line is electrically matched on input and output port. Measurements were performed using the network analyzer HP4396A. Frequency range of the measurement spanned from 1.0 MHz to 1.8

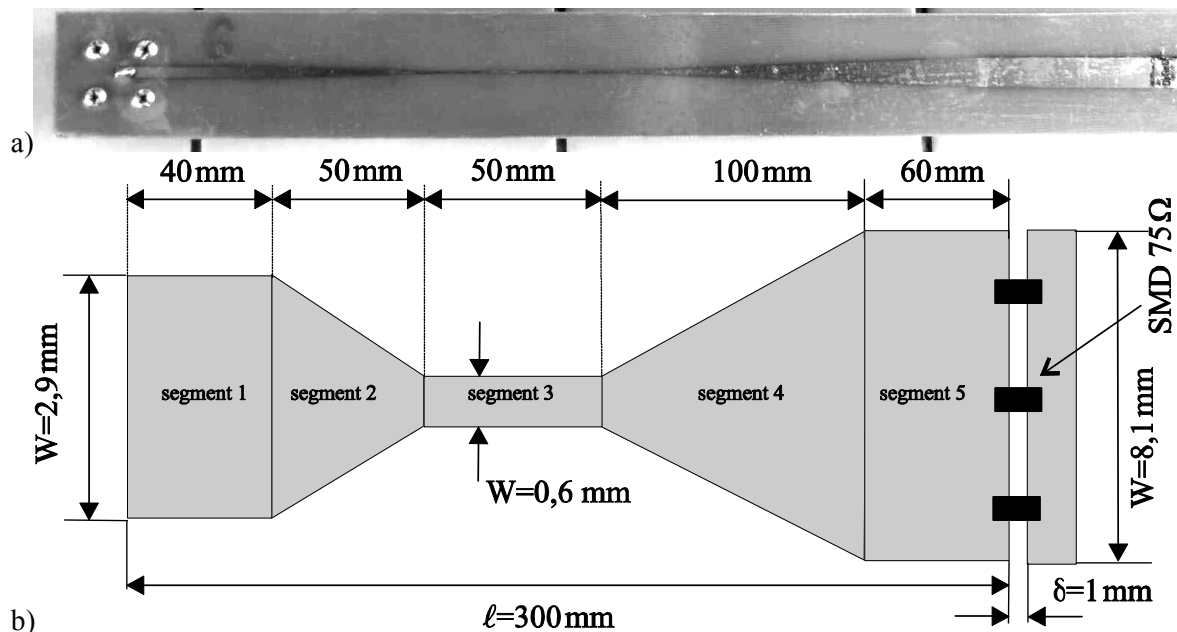


Fig. 7. Tapered lossless transmission lines investigated experimentally a) photograph b) drawing with dimensioning.

GHz. The amplitude and phase of the measured reflection coefficient of the input port is shown in Fig. 8.

The characteristic impedance of the line varies continuously from the value of about 50 ohms through 100 ohms to a value of approximately 25 ohms. However, there is not any generally accepted method of calculating the wave impedance stripline based on its geometry and electrical properties of materials. There are simplified equations, which do not take into account the thickness of the foil e.g. [31]. In literature one can find a more complex formula, which takes into account the thickness of the foil e.g. [32]. None of these equations are much better than the others. It was therefore decided that the characteristic impedance of the line calculated for the first time using the formula found in [31], and the second time using the model found in [32]. Then, the author made a model of nonuniform parts of the transmission line, as proposed in this article. Section 2 was modeled by four third-order segments. Section 4 was modeled by eight third-order segments. Uniform parts (segments 1, 3, and 5) were modeled by intristical SPICE model. The input port was excited by a triangular impulse. Basically, the shape of the impulse was the following:

$$e(t) = A \cdot \begin{cases} t/\tau_1 & \text{for } 0 \leq t \leq \tau_1 \\ (2\tau_1 - t)/\tau_1 & \text{for } \tau_1 \leq t \leq 2\tau_1, \\ 0 & \text{otherwise} \end{cases} \quad (40)$$

where $\tau_1 = 2$ ns and $A=1$ V. Pulse is formed through the Chebyshev filter of 15-order with a

pass-band frequency 1.8GHz, so to limit its spectrum. The wave reflected from the input port, as calculated by the program SPICE, is presented in the Fig. 9. Actually, the figure shows two waveforms computed by SPICE – time calculations was 1.02 s, using the SPICE program on a 2.5 GHz PC. First of them (solid line) concerns the profile of the transmission line impedance calculated by formulas from [32]. The second waveform (dotted line) concerns the impedance profile of transmission line calculated by formulas from [31]. In addition, the figure shows a reflected wave, which was calculated from the measured reflection coefficient (points). For calculations, the standard algorithm for convolution of discrete signals using the FFT was used [35]. Comparing the calculated and measured results, we found that the result agrees well with the experiment.

VIII. CONCLUSIONS

In this article, a method of nonuniform transmission line analysis is proposed. The method reduces NUTL to cascaded linear varied transmission lines. LNTL segments are approximated by a passive circuit, which consists of inductance, cascaded with Darlington C section. The model is implemented in circuit simulator as active circuit similar to OTA-based leapfrog filter. Parameters of each section are computed using polynomial regression. Cascaded circuits are insensitive to parameters variation. Due to this fact, inevitable regression errors do not disturb the frequency response of the model significantly.

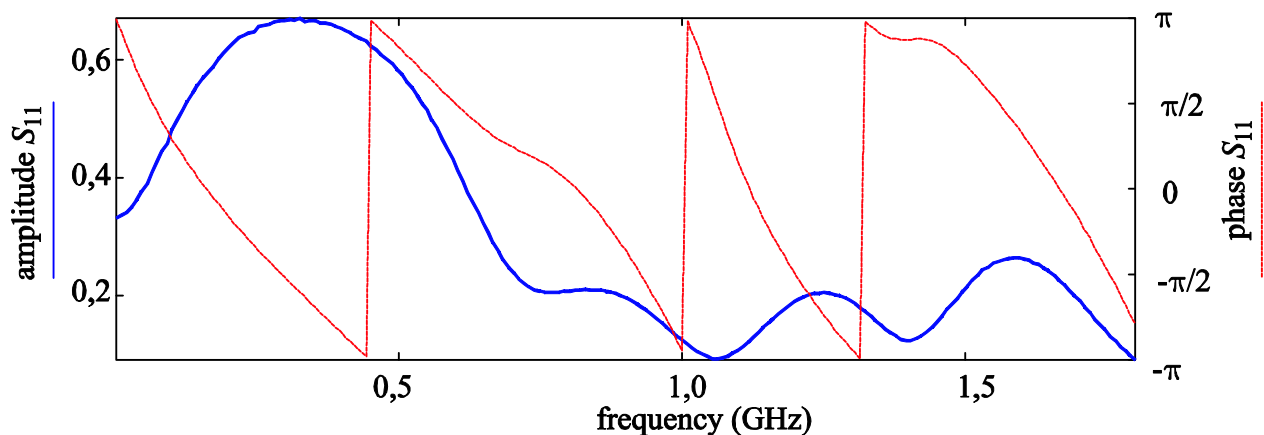


Fig. 8. Amplitude and phase of reflection coefficient $S_{11}(\omega)$ of stripline from Fig. 7. Measurement made with HP4396A.

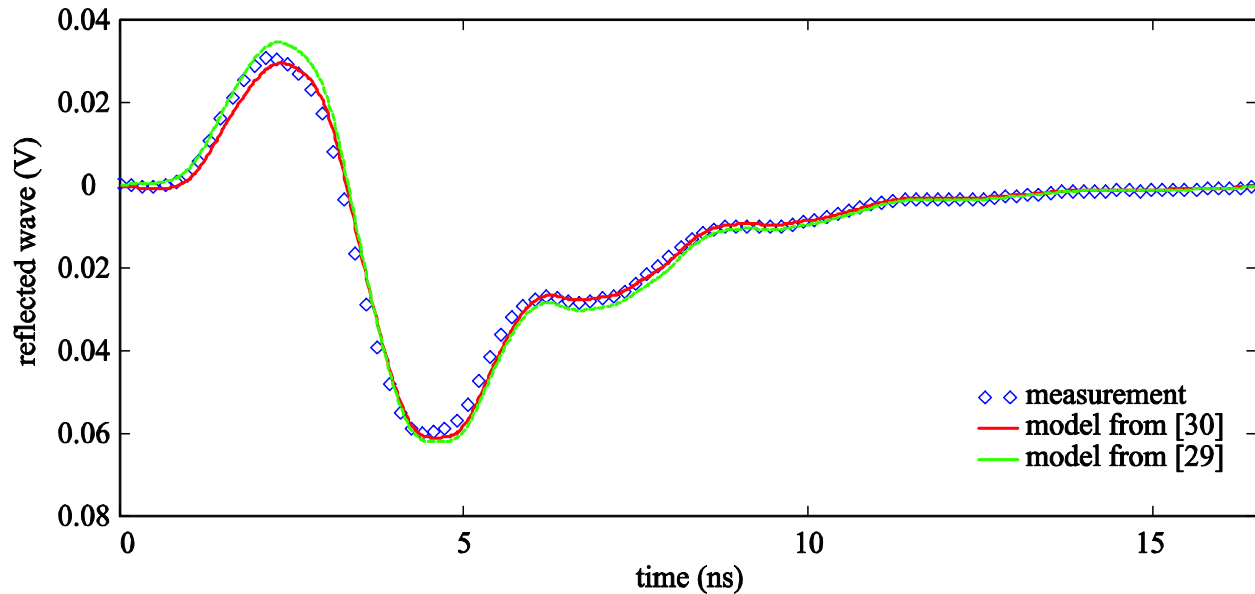


Fig. 9. Waveform, which was computed by SPICE, reflected from input port of the stripline (Fig. 7) vs. measured waveform.

Calculations performed using the proposed model agree well with laboratory measurements.

REFERENCES

- [1] J. Jeong and R. Nevels, "Time-Domain Analysis of a Lossy Nonuniform Transmission Line," *IEEE Transactions on Circuits and Systems II: Express Briefs*, vol. 56, no. 2, pp. 157–161, Feb. 2009.
- [2] L. Jia, W. Shi, and J. Guo, "Arbitrary-Difference Precise-Integration Method for the Computation of Electromagnetic Transients in Single-Phase Nonuniform Transmission Line," *IEEE Transactions on Power Delivery*, vol. 23, no. 3, pp. 1488–1494, July 2008.
- [3] M. Tang and J. Mao, "A Precise Time-Step Integration Method for Transient Analysis of Lossy Nonuniform Transmission Lines," *IEEE Transactions on Electromagnetic Compatibility*, vol. 50, no. 1, pp. 166–174, Feb. 2008.
- [4] E. Gad and M. Nakhla, "Simulation and sensitivity analysis of nonuniform transmission lines using integrated congruence transform," *IEEE Transactions on Advanced Packaging*, vol. 28, no. 1, pp. 32–44, Feb. 2005.
- [5] F. Kato, "A theory for deriving exactly solvable nonuniform transmission lines systematically," *IEEE Transactions on Circuits and Systems II: Express Briefs*, vol. 52, no. 12, pp. 836–840, Dec. 2005.
- [6] L. A. Hayden and V. K. Tripathi, "Nonuniformly coupled microstrip transversal filters for analog signal processing," *IEEE Trans. Microwave Theory Tech.*, vol. 39, pp. 47–53, Jan. 1991.
- [7] S. C. Burkhart and R. B. Wilcox, "Arbitrary pulse shape synthesis via nonuniform transmission lines," *IEEE Trans. Microwave Theory Tech.*, vol. 38, pp. 1514–1518, Oct. 1990.
- [8] G. Antonini, L. De Camillis, and F. Ruscitti, "A Closed-Form Sensitivity Analysis of Transmission Lines," *ACES Journal*, vol. 24, no. 4, pp. 352–360, Aug. 2009.
- [9] B. Essakhi, J. Benel, M. Smail, G. Akoun, and L. Pichon, "Circuit Models for Interconnects Using 3D Computational Techniques," *ACES Journal*, vol. 23, no. 1, pp. 39–45, March 2008.
- [10] A. G. Chiariello, A. Maffucci, G. Miano, F. Villone, and W. Zamboni, "High-Frequency Full-Wave Analysis of Interconnects with Inhomogeneous Dielectrics through an Enhanced Transmission Line Model," *ACES Journal*, vol. 23, no. 1, pp. 31–38, March 2008.
- [11] S. Barmada and M. Raugi, "Transient numerical solutions of nonuniform MTL equations with nonlinear loads by wavelet expansion in time or space domain," *IEEE Transactions on Circuits and Systems I: Fundamental Theory and Applications*, vol. 47, no. 8, pp. 1178–1190, Aug. 2000.
- [12] S. Barmada, "Algebraic solution of time-domain nonuniform transmission-line equations by 2-D wavelet transform," *IEEE Transactions on Circuits and Systems I: Fundamental Theory and Applications*, vol. 49, no. 4, pp. 504–508, Apr. 2002.

- [13] G.W. Roberts and A.S. Sedra, *SPICE, Second edition*, Oxford University Press, New York, 1997.
- [14] D. Saraswat, R. Achar, and M. S. Nakhla, "Global Passivity Enforcement Algorithm for Macromodels of Interconnect Subnetworks Characterized by Tabulated Data," *IEEE Transactions on Very Large Scale Integration (VLSI) Systems*, vol. 13, no. 7, pp. 819–832, July 2005.
- [15] P. Triverio, S. Grivet-Talocia, M. S. Nakhla, F. G. Canavero, and R. Achar, "Stability, Causality, and Passivity in Electrical Interconnect Models," *IEEE Transactions on Advanced Packaging*, vol. 30, no. 4, Nov. 2007, pp. 795–808.
- [16] D. Saraswat, R. Achar, and M. S. Nakhla, "Fast Passivity Verification and Enforcement via Reciprocal Systems for Interconnects with Large Order Macromodels," *IEEE Transactions on Very Large Scale Integration (VLSI) Systems*, vol. 15, no. 1, pp. 48–59, Jan. 2007.
- [17] B. Gustavsen and A. Semlyen, "Enforcing passivity for admittance matrices approximated by rational functions," *IEEE Transactions on Power Systems*, vol. 16, no. 1, pp. 97–104, Feb. 2001.
- [18] B. Porkar, M. Vakilian, R. Iravani, and S. M. Shahrtash, "Passivity Enforcement Using an Infeasible-Interior-Point Primal-Dual Method," *IEEE Transactions on Power Systems*, vol. 23, no. 3, pp. 966–974, Aug. 2008.
- [19] B. Gustavsen, "Fast Passivity Enforcement for S-Parameter Models by Perturbation of Residue Matrix Eigenvalues," *IEEE Transactions on Advanced Packaging*, vol. 33, no. 1, pp. 257–265, Feb. 2010.
- [20] B. Anderson, J. E. Bracken, J. B. Manges, G. Peng, and Z. Cendes, "Full-wave analysis in SPICE via model-order reduction," *IEEE Transactions on Microwave Theory and Techniques*, vol. 52, no. 9, pp. 2314–2320, Sept. 2004.
- [21] A. Lamecki and M. Mrozowski, "Equivalent SPICE Circuits With Guaranteed Passivity from Nonpassive Models," *IEEE Transactions on Microwave Theory and Techniques*, vol. 55, no. 3, pp. 526–532, March 2007.
- [22] W. Cauer, *Synthesis of Linear Communications Network*, New York: McGraw-Hill, 1958.
- [23] W-K. Chen, "Passive Immittances and Positive-Real Functions," *The Circuits and Filters Handbook*, CRC Press Inc., Boca Raton, 2003.
- [24] J. Izydorczyk, "A simple SPICE model of a nonuniform transmission line," *33rd International Conference and Exhibition IMAPS – Poland 2009*, Gliwice-Pszczyna, pp. 163–166, 21-24 September 2009.
- [25] J. Izydorczyk, "Nonuniform transmission line simulation with circuit simulator," *Proceedings of IEEE MELECON 2010 Mediterranean Electrotechnical Conference*, Valetta (Malta), 25-28 April 2010.
- [26] K. Lu, "An Efficient Method for Analysis of Arbitrary Nonuniform Transmission Lines," *IEEE Trans. Microwave Theory Tech.*, vol. 45, no. 1, pp. 9–14, January 1997.
- [27] G. J. Fisher and J. A. Connelly, "Modeling Time-Dependent Elements for SPICE Transient Analyses," *IEEE Transactions on Computer-Aided Design of Integrated Circuits and Systems*, vol. 5, no. 3, pp. 429–432, July 1986.
- [28] E. Sanchez-Sinencio and J. Silva-Martinez, "CMOS transconductance amplifiers, architectures and active filters: a tutorial," *IEE Proceedings - Circuits, Devices and Systems*, vol. 147, no. 1, pp. 3–12, Feb 2000.
- [29] R. Schaumann, "Continuous-Time Integrated Filters," *The Circuits and Filters Handbook*. CRC Press, Boca-Raton, 2003.
- [30] N. W. McLachlan, *Bessel Functions for Engineers*, 2nd edition, Clarendon Press, Oxford, 1955.
- [31] S. Rosłonec, *Design methodology of some linear microwave circuits*, WKiŁ, Warszawa, pp. 125–128, 1987.
- [32] T. K. Ishii, "Transmission lines," *The Circuits and Filters Handbook*. CRC Press and IEEE Press, 2003, pp. 1165–1181.
- [33] T. Needham, *Complex Analysis*, Oxford University Press, Oxford, 2002.
- [34] H. J. Carlin, "Darlington synthesis revisited," *IEEE Trans. Circuits Syst. I*, vol. 46, no. 1, pp. 14–21, January 1999.
- [35] A.V. Oppenheim and R. W. Schaffer, *Digital Signal Processing*, Prentice-Hall. Inc., Englewood Cliffs, New Jersey, 1975.

Appendix I

Synthesis algorithm of Nth order model of LNTL

1. Let delay of the line τ be equal to 1s and let wave impedance at the input Z_0 of the line be equal to 1Ω .
2. Select a set of points $\{k\ell_1, k\ell_2, \dots, k\ell_K\}$ from the interval $0.1 \leq k\ell \leq 10$.
3. $n = 1$.
4. Let $k\ell = k\ell_n$.
5. Numerically evaluate $2N+1$ poles of the linear varied nonuniform transmission line. Pole is always at $\omega = 0$. The rest of $2N$ poles are solutions of the following nonlinear equation:

$$J_1\left(\frac{p(1+k\ell)}{k\ell}\right)Y_1\left(\frac{p}{k\ell}\right) - J_1\left(\frac{p}{k\ell}\right)Y_1\left(\frac{p(1+k\ell)}{k\ell}\right) = 0.$$

The solutions should have the smallest absolute value possible. Approximate values of the solutions are given by formula $p \approx n \cdot \pi$ where $n = \pm 1, \pm 2, \dots, \pm N$.

6. Evaluate residues of y_{21} parameter at poles found in Step 4) by using equation (11).

7. Numerically evaluate $2N$ zeroes of y_{11} parameter and $2N$ zeroes of y_{22} parameter of the linear varied nonuniform transmission line. Zeros of y_{11} parameters are solutions of nonlinear equation:

$$J_1\left(\frac{p(1+k\ell)}{k\ell}\right)Y_0\left(\frac{p}{k\ell}\right) - J_0\left(\frac{p}{k\ell}\right)Y_1\left(\frac{p(1+k\ell)}{k\ell}\right) = 0.$$

Zeros of y_{22} parameter are solutions of nonlinear equation:

$$J_1\left(\frac{p}{k\ell}\right)Y_0\left(\frac{p(1+k\ell)}{k\ell}\right) - J_0\left(\frac{p(1+k\ell)}{k\ell}\right)Y_1\left(\frac{p}{k\ell}\right) = 0$$

Approximate values of zeros are given by formula $p \approx n \cdot \pi + \pi/2$ where $n = -N, -N+1, \dots, N-1$.

8. Evaluate residues of y_{11} and y_{22} parameter at poles found in Step 4) by using equation (13) and (14) respectively.

9. Evaluate correction coefficients a, b and c for each residuum by using formulas (28) and (29).

10. Evaluate coefficients of rational function, which describes the input impedance $Z(s) = 1/Y_{in}(s)$ by using equation (22).

Determinant $\Delta = y_{12}^2 - y_{11}y_{22}$ possess only poles of multiplicity one. Residuum a_n of the determinant at pole p_n can be computed using formula:

$$a_n = \sum_{\substack{k=-N \\ k \neq n}}^N \frac{2a_{k,12}a_{n,12} - a_{k,22}a_{n,11} - a_{n,22}a_{k,11}}{(p_k - p_n)}.$$

where $a_{n,ij}$ is a corrected residuum of y_{ij} at pole p_n .

11. Separate inductance L_x using formula:

$$L_x = \lim_{s \rightarrow \infty} \frac{Li(s)}{s \cdot Mn(s)}, \quad (41)$$

where impedance function is a ratio of polynomials $Z(s) = Li(s)/Mn(s)$.

12. Let us $Z(s) \leftarrow Z(s) - sL_x$.

13. Numerically solve polynomial equation:

$$Ev(Z(s)) = 0. \quad (42)$$

14. Choose solution s_0 of (42) which has negative real part and minimal absolute value.

15. Evaluate index set $\{q_0, q_1, q_2, q_3\}$ assigned to s_0 by impedance function $Z(s)$. Elements of index set are given by formulas:

$$q_0 = \frac{R_0/\sigma_0 - X_0/\omega_0}{R_0/\sigma_0 + X_0/\omega_0}, \quad (43)$$

$$q_1 = \frac{2Z_0Z_0^*}{R_0/\sigma_0 + X_0/\omega_0}, \quad (44)$$

$$q_2 = \frac{2}{R_0/\sigma_0 - X_0/\omega_0}, \quad (45)$$

$$q_3 = \frac{R_0/\sigma_0 + X_0/\omega_0}{R_0/\sigma_0 - X_0/\omega_0} = \frac{1}{q_0}, \quad (46)$$

$$\text{where } Z(s_0) = Z_0 = R_0 + j \cdot X_0. \quad (47)$$

16. Compute coefficients of rational function:

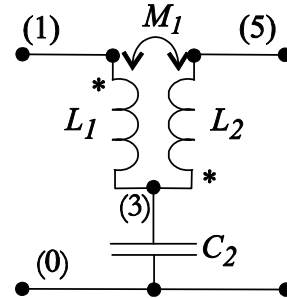


Fig. 10. The Darlington type-C section.

$$W_1(s) = \frac{D_1(s)Z(s) - B_1(s)}{-C_1(s)Z(s) + A_1(s)}, \quad (48)$$

$$\text{where } A_1(s) = q_3s^2 + s_0s_0^*, \quad (49)$$

$$B_1(s) = q_1s, \quad (50)$$

$$C_1(s) = q_2s, \quad (51)$$

$$D_1(s) = q_0s^2 + s_0s_0^*. \quad (52)$$

Detailed algorithm of computations is given in the Appendix II.

17. If s_0 is a real function, compute parameters of type-C section:

$$L_1 = \frac{1}{q_0q_2}, \quad L_2 = \frac{q_0}{q_2}, \quad (53)$$

$$C_2 = \frac{q_2}{\sigma_0^2}, \quad M_1 = \frac{-1}{q_2} < 0. \quad (54)$$

18. If order of $W_1(s)=0$ then go to 25.
19. Let $Z(s) \leftarrow W_1(s)$.

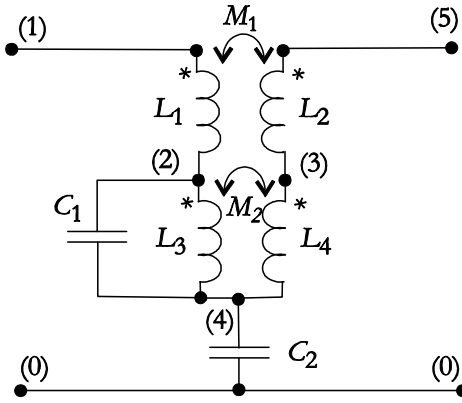


Fig. 11. The Darlington type-D section

20. Evaluate index set $\{p_0, p_1, p_2, p_3\}$ assigned to s_0 by modified impedance function $Z(s)$ by using equations (43)-(47).

21. Compute coefficients of rational function:

$$W_2(s) = \frac{D_2(s)Z(s) - B_2(s)}{-C_2(s)Z(s) + A_2(s)}, \quad (55)$$

$$\text{where } A_2(s) = p_3s^2 + s_0s_0^*, \quad (56)$$

$$B_2(s) = p_1s, \quad (57)$$

$$C_2(s) = p_2s, \quad (58)$$

$$D_2(s) = p_0s^2 + s_0s_0^*. \quad (59)$$

Detailed algorithm of computations is given in the Appendix II.

22. Compute parameters of type-D section:

$$L_1 = \frac{p_3q_3}{p_3q_2 + p_2q_0}, \quad L_2 = \frac{p_0q_0}{p_3q_2 + p_2q_0}, \quad (60)$$

$$M_1 = \sqrt{L_1L_2}, \quad C_2 = \frac{p_2 + q_2}{s_0s_0^*}, \quad (61)$$

$$M_2 = -\frac{\omega_{13}^4 - 2(\omega_0^2 - \sigma_0^2)\omega_{13}^2 + |s_0|^4}{\omega_{13}^4(p_3q_2 + p_2q_0)} \leq 0, \quad (62)$$

$$\text{where } \omega_{13}^2 = \frac{s_0s_0^*(p_2 + q_2)}{p_3q_2 + p_2q_0}, \quad (63)$$

$$L_4 = -\frac{q_2M_2}{p_2}, \quad L_3 = -\frac{p_2M_2}{q_2}, \quad C_1 = -\frac{q_2}{\omega_{13}^2p_2M_2}. \quad (64)$$

23. If order of $W_2(s)=0$ then go to 25.
24. Let $Z(s) \leftarrow W_2(s)$ and go to 13.

25. Let $n = n + 1$.
26. If $n \leq N$ go to 4.
27. For each element of the circuit, find parameters of regression curve describing variation of the element versus variations of kl parameter.

Appendix II

Algorithm of rational function separating

Consider rational PR function

$$Z(s) = Li(s) / Mn(s), \text{ where}$$

$$Li(s) = l_0 + l_1s + \dots + l_Ns^N,$$

$Mn(s) = m_0 + m_1s + \dots + m_Ns^N$ and four polynomials:

$$A(s) = a_0 + a_2s^2, \quad B(s) = b_1s, \quad (65)$$

$$C(s) = c_1s, \quad D(s) = d_0 + d_2s^2,$$

obtained according equations (49)-(52). Exists rational PR function $W(s)$ [34]:

$$Z(s) = \frac{A(s)W(s) + B(s)}{C(s)W(s) + D(s)} \quad (66)$$

$$\text{or } Z(s) = \frac{A(s)Li'(s) + B(s)Mn'(s)}{C(s)Li'(s) + D(s)Mn'(s)} = \frac{Li(s)}{Mn(s)}, \quad (67)$$

where $Li'(s) = l'_0 + l'_1s + \dots + l'_{N-1}s^{N-1}$, $Mn'(s) = m'_0 + m'_1s + \dots + m'_{N-1}s^{N-1}$. Order of $W(s)$ is equal to order of $Z(s)$ decremented by 2. Coefficients of the left side numerator should be equal the right side coefficients of numerator of (67). At the same time, coefficients of the left side denominator of should be equal coefficients of the right side denominator of (67). From equality of free coefficients we obtain:

$$l'_0 = \frac{l_0}{a_0}, \quad m'_0 = \frac{l'_0}{d_0}. \quad (68)$$

Equality of first order coefficients gives:

$$l'_1 = \frac{l_1 - m'_0b_1}{a_0}, \quad m'_1 = \frac{m_1 - l'_0c_1}{d_0}. \quad (69)$$

Equality of second order coefficients gives:

$$l'_2 = \frac{l_2 - m'_1b_1 - l'_0a_2}{a_0}, \quad m'_2 = \frac{m_2 - l'_1c_1 - m'_0d_2}{d_0}. \quad (70)$$

Equality of third order coefficients gives:

$$l'_3 = \frac{l_3 - m'_2b_1 - l'_1a_2}{a_0}, \quad m'_3 = \frac{l_3 - l'_2c_1 - m'_1d_2}{d_0}. \quad (71)$$

In general, following recursive formula can be written:

$$l_k = \frac{l_k - m'_{k-1}b_1 - l'_{k-2}a_2}{a_0},$$

$$m_k = \frac{m_k - l'_{k-1}c_1 - m'_{k-2}d_2}{d_0},$$
(72)

where $k = 0, 1, \dots, N-1$. Initial conditions for computations are:

$$l_{-1} = l_{-2} = m_{-1} = m_{-2} = 0. \quad (73)$$

Similarly, the reverse computing formula can be obtained.



Jacek Izydorczyk (M'95) was born in Bielszowice, Silesia, Poland in 1964 and became a Member (M) of IEEE in 1995 and senior member of IEEE in 2009.

He obtained his M.S. degree from Silesian University of Technology, Gliwice, Poland in 1988, Ph.D. degree from Silesian University of Technology, Gliwice, Poland in 1990. His dissertation research dealing with the construction of time domain invariants of sensitivities in the linear and non-linear circuits. He is involved in the researches dealing with network invariants, circuit simulations, magnetic media modeling, signal processing, speech synthesis, speech modeling, and analog filters.

Dr. Izydorczyk is author or co-author of three books published in Poland, i.e. *Pspice*, *Signal Theory*, and *Analog and Digital Filters*.

High-Isolation and Low-Loss RF MEMS Shunt Switches

Haslina Jaafar^{1,2}, Othman Sidek², Azman Miskam², and Razi Abdul-Rahman^{2,3}

¹ Department of Electrical and Electronics Engineering, Faculty of Engineering
Universiti Putra Malaysia, 43400, Serdang, Selangor
jhaslina@eng.upm.edu.my

² Collaborative Microelectronic Design Excellence Centre
Universiti Sains Malaysia, Engineering Campus, 14300 Nibong Tebal, Pulau Pinang, Malaysia

³ School of Mechanical Engineering
Universiti Sains Malaysia, Engineering Campus, 14300 Nibong Tebal, Pulau Pinang, Malaysia
othman@cedec.usm.my, azman@cedec.usm.my, arahman@eng.usm.my

Abstract — This paper presents the design and simulation of a radio frequency (RF) microelectromechanical system (MEMS) shunt switch using a three-dimensional RF simulator, Em3ds10 (2008 version) software for the frequency range of 1-40 GHz. The shunt capacitive switch is electrostatic actuated and designed with a meander beam support to lower the pull-in voltage. Fast simulations of complex structures based on a method-of-moment approach allow for optimal design of MEMS switch. The switch has a simulated pull-in voltage of 2.5 V and the RF performances of insertion loss and isolation are less than -0.2 dB and -50 dB at 12 GHz, respectively.

Index Terms — Insertion loss, isolation, low voltage, MEMS, method-of-moment, RF MEMS, shunt switch.

I. INTRODUCTION

Radio frequency (RF) microelectromechanical system (MEMS) technology is an area of MEMS technology that shows great potential. RF MEMS enable the creation of devices and techniques to improve the performance of communication circuits and systems. The RF MEMS switch enables the realization of micro-size mechanical switches to be embedded in electronic devices. The MEMS switch offers the advantages of low actuation, low insertion loss,

high isolation, large capacitance ratio, and high-power handling. Thus, a low-voltage, low-insertion loss, and high-isolation MEMS switch is desirable for switch better performance.

A RF MEMS shunt switch is a type of MEMS switch, unlike a series switch, which consists of a suspended movable thin metal bridge over the center conductor. It is fixed and anchored at both ends to the ground line of the transmission line. MEMS switches for RF applications operate through short and open circuits to transmit signals. They operate based on mechanical movement to achieve on and off states.

Figures 1 (a) and 1 (b) show the MEMS shunt switch in the on state and off state conditions. In the on or up state, the DC bias voltage applied to the signal line is 0 V; therefore, the bridge remains up and the signal easily passes through the transmission line due to low capacitance. However, when the DC voltage increases, the center electrode provides an electrostatic force and high RF capacitance between the transmission line and the ground. As a result, the bridge is pulled down onto the dielectric layer placed on top of the signal line. This causes the RF signal to short onto the ground. This state is called the off or down state.

The shunt switch could be integrated in a coplanar waveguide (CPW) or in a microstrip transmission line. In a CPW transmission line, the anchors of the switch are normally connected to the CPW ground planes in the microstrip

configuration. One anchor is connected to a quarter-wave open stub, which creates the short circuit at the bridge, and the second anchor is left unconnected or connected to the bias resistor [1].

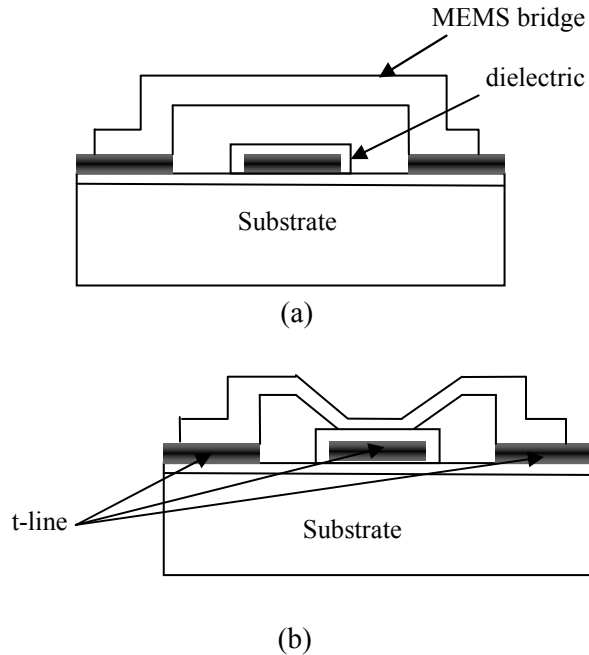


Fig. 1. RF MEMS shunt switch on CPW transmission line: (a) on/up state (b) off/down state.

Obtaining an optimal design of a MEMS shunt switch is best achieved with the aid of a modeling tool for obvious economical advantages. In this work, simulations based on an approach called generalized transverse resonance diffraction (GTRD) have been used. The GTRD method is being implemented in the Em3ds10 software package developed by MEM research. Based on the method of moments, it is a general three-dimensional (3D) integral equation approach for the modeling of passive monolithic microwave integrated circuits (MMICs) involving thick lossy conductors and dielectric discontinuities. The ability of the method to efficiently handle thick lossy conductors and dielectric discontinuities in complex structures is discussed in [2]. It has been shown to successfully model several structures such as the metal-insulator-metal (MIM) capacitor, spiral inductors, and CPWs.

II. RF PARAMETERS

As the parameters of RF performance are essential, microwave parameters other than the actuation voltage should, also, be considered and optimized when designing RF MEMS switches. In the on state, the RF switch connects the input port to the output port. In the off state, the switch is configured to disconnect the two ports. The measurable parameters for RF performance are insertion loss in the on state, isolation in the off state, and return loss in both states. Achievements of the design include the RF insertion loss and isolation at less than -0.5 dB and approximately 26 dB, respectively, obtained at 40 GHz [3].

The MEMS shunt switch is modeled by two short sections comprising a transmission line and a lumped capacitance, inductance and resistance (CLR) model of the bridge with the capacitance with up state/down state values as shown in Fig. 2 [4].

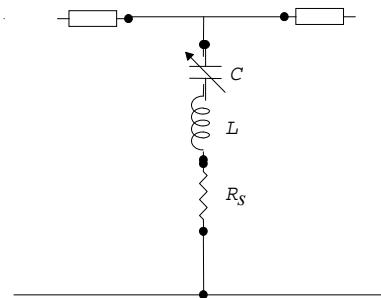


Fig. 2. Circuit model of a MEMS shunt switch.

The switch shunt impedance is given by (1).

$$Z_s = R_s + j\omega L + \frac{1}{j\omega C} \quad (1)$$

where C is C_u or C_d depending on the position of the switch. The inductance and capacitance (LC) series resonant frequency of the shunt switch is:

$$f_o = \frac{1}{2\pi\sqrt{LC}} \quad (2)$$

In the up state position, $Z_s \gg Z_o$, and the loss becomes

$$\text{Loss} = \omega^2 C_u^2 R_s Z_o \quad (3)$$

In the down state position, $Z_s \ll Z_o$, and the loss is [4]

$$\text{Loss} = \frac{4R_s}{Z_o} \quad (4)$$

The insertion loss is caused by the mismatch between the characteristic impedances of the line and the switch [5]. The contact resistance and the beam metallization loss will also contribute to the insertion loss. Hence, it is essential to design RF MEMS switches with transmission line structures that are circuit elements in a microwave integrated circuit.

Low-insertion loss MEMS shunt switches are one of the design goals for most MEMS switches. The ratio between the C_u and C_d is a key parameter for the capacitive coupling shunt switch as it is a determining factor for both insertion loss and isolation. A small C_u is necessary for maintaining low insertion loss. This requires a large gap between the membrane and the bottom electrode, which is traded off by achieving a low pull-down voltage [5].

When the membrane is in the unactuated or up state, the capacitance of the system is approximated using (5) by considering the dielectric layer between the two plates.

$$C_u = \epsilon_0 w W \left(g_0 + \frac{t_d}{\epsilon_r} \right)^{-1}, \quad (5)$$

where w is the width of the membrane, W is the width of the center conductor of the CPW line, g_0 is the gap height between the membrane and the bottom transmission line, ϵ_0 is air permittivity, t_d is the thickness of the dielectric layer and ϵ_r is the relative permittivity.

The MEMS switch capacitance in the down state position can be calculated using (6).

$$C_d = \frac{\epsilon_o \epsilon_r A}{t_d}, \quad (6)$$

where A is the area of pull-down electrode ($w \times W$). In this case, the thickness of the dielectric is so small that the fringing capacitance is negligible [5]. Thus, the down state/up state capacitance ratio is

$$\frac{C_d}{C_u} = \frac{\frac{\epsilon_o \epsilon_r A}{t_d}}{\frac{\epsilon_o A}{g + \frac{t_d}{\epsilon_r}} + C_f}, \quad (7)$$

with $C_f = 0.3 - 0.4C_u$.

High isolation is a desirable parameter of RF switches in the off or down state condition. In this state, a capacitance causes undesired coupling.

The gap between the membrane and the signal line could be increased for greater isolation (> 20 dB is desirable). However, a high gap will result in an even greater actuation voltage. Therefore, a large Cd is necessary to maintain high isolation. This requires intimate contact between the membrane and the dielectric film over the bottom electrode in the down state [5]. The increment of Cd/Cu can effectively improve isolation performance.

III. RF SIMULATIONS

The shunt switch is designed on silicon substrates layers of 280 μm thickness. Then, 1 μm aluminum is fabricated on the silicon layer as the transmission line, while silicon nitride is deposited on the electrode (middle transmission line) as the dielectric layer. The switch membrane consists of a thin Au with 1.5 μm thickness over the 2.5 μm gap between the membrane and the electrode. The transmission line metal connects the electrode and the dielectrics materials to form the through path of a shunt switch.

In this research, the CPW was used as the transmission line of the RF MEMS capacitive shunt switch. The characteristics of the CPW line greatly depend on the width, W , conductor spacing, S , substrate permittivity, ϵ_r , and the height of the substrate, H , to obtain the desired characteristic impedance, Z_0 .

The utilized CPW had a signal line width of 100 μm and 60 μm of space. The Z_0 of the 60/100/60 μ ($S/W/S$) CPW was designed with a silicon substrate height of 280 μm approximately 50 Ω .

The Em3ds10 software was used to simulate the RF performances in terms of insertion loss and isolation during the on and off state conditions. Using the software, the switch design can be built and simulated either using 2.5-dimensional (2.5D) or 3D mode. However, the speed is increased in 2.5D mode by a factor varying from 50% up to more than 300% [8]. In other words, the more complex the structure, the larger is the time saved [8].

The switch structure is drawn layer by layer starting from the top layer to the substrate. Few parameters of each layer were defined including y subsection, thickness and the material properties. Figure 3 shows the switch design which consists of five layers for substrate, transmission line,

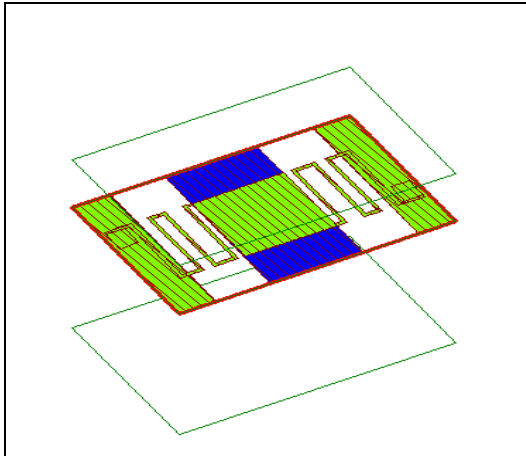


Fig. 3. Switch design using Em3ds in 2.5D mode.

dielectric, bridge, and via. The simulation done was twice for up state and downstate conditions and the design for the two conditions was different depending on the gap height and structure.

This simulator used finite-thickness, finite conductivity real conductors, and dielectrics by using volume mesh currents. The current induced in conductors appears to be oriented of $(J_x, J_y$ and $J_z)$ in the 3D mode [6] as the total current may have arbitrary orientation even over sides of a thick conductor. J_x is described by piece-wise sinusoidal (PWS) function with respect to x and piece-wise constant (PWC) function with respect to y and z . Similarly, J_z is described by means of PWS function with respect to z and PWC with respect to x and y . However, vertical y currents are piecewise constant with respect to any direction [6]. Figure 4 shows the relationship with mesh cells as J_x and J_y as a function of x [8].

In addition, better results can be obtained by setting a fine y subsectioning whenever sharp vertical discontinuities are encountered, such as in vias or contacts between conductors lying on different layers. This is due to increasing the number of vertical y or “slices” which may result in a large computational effort [2].

The GTRD approach of modeling with this reduced dimension was first verified by comparing the simulation results of scattering parameters with the experimental data published by [3]. As depicted in Figure 5, the computed insertion loss S_{21} and return loss S_{11} in the down state condition for the switch design in [3] agrees well with the

measurements. Of significant interest is the reduction in simulation time is considerable; up to 50 percent of reduction time was observed compared with full three dimensional modeling.

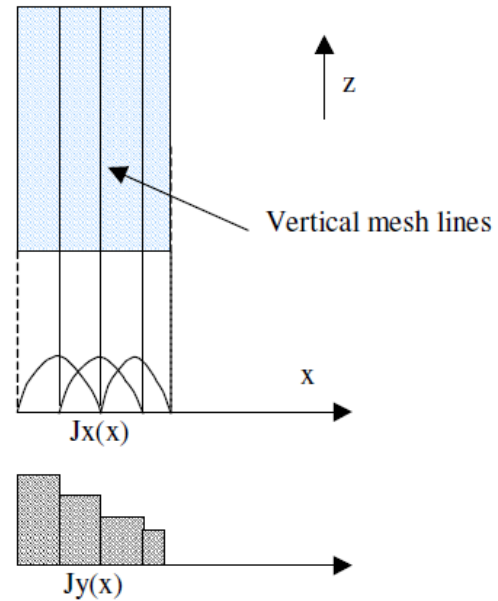


Fig. 4. J_x and J_y as function of x .

IV. RESULTS AND DISCUSSION

The insertion loss and isolation are obtained by the simulation of the S parameters when the switch transmits the signal while in the up state, and the signal is capacitively grounded when the beam is in the down state. Figures 6 and 7 illustrate the RF characterization results in the up (on) state condition when the membrane is unactuated. From the S parameter, the insertion loss, which is measured as S_{21} in the up state condition is very low (approximately -0.03 dB at 9 GHz or -0.27 dB at 30 GHz). Meanwhile, the return loss measured as S_{11} in the same condition is 13 dB at 29 GHz. The insertion loss is a measure of its efficiency for signal transmission. The return loss is the reflected energy due to the parasitic capacitance caused by the proximity of the transmission path to the grounded metal membrane in the suspended off state [7].

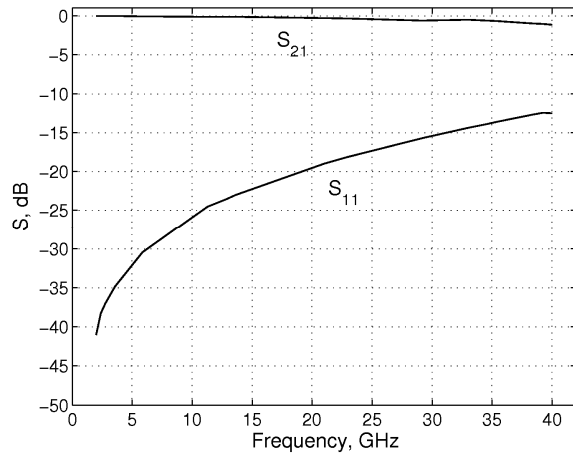


Fig. 5. Insertion loss S_{21} and return loss S_{11} in the down state condition for the switch model in [3].

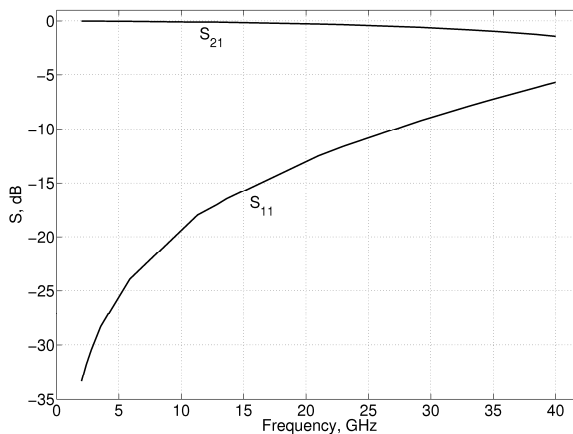


Fig. 6. S parameter showing both insertion loss S_{21} and return loss S_{11} in the up state condition.

A lower insertion loss means a better switch. Resistive losses at lower frequencies and skin depth effects at higher frequencies are the major causes for these losses [5].

Isolation is simulated in the down state condition where the RF signal originating from the input is shorted to the ground due to beam reflection. In other words, isolation is measured when no signal transmission occurs. The isolation value may, also, be defined as a result of proximity coupling between the moving part and the stationary transmission line of leakage currents [5]. Thus, greater isolation means better

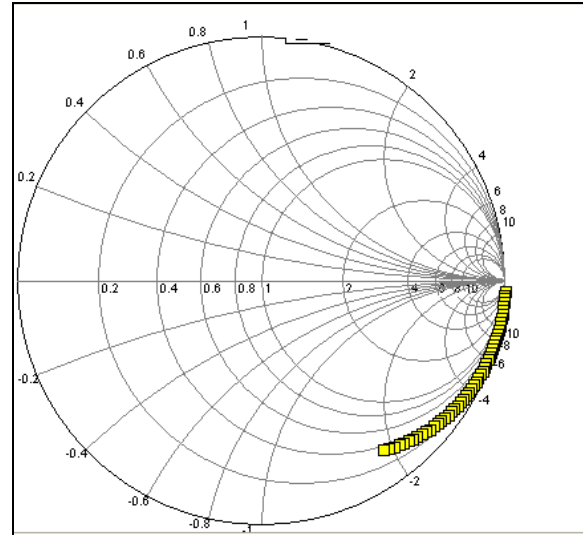


Fig. 7. Insertion loss illustrated in a Smith chart.

performance of the switch. Figure 8 shows that the S parameter for the downstate condition, represented by S_{21} , is -50 dB at 12 GHz, while the isolation illustrated in a Smith chart is shown in Figure 9. From the S parameter, the resulting isolation is high and above the minimum requirement of -20 dB.

One means of obtaining a higher isolation at lower frequencies is to increase the series inductance of the switch to lower the resonant frequency. This is achieved by adding a short section of transmission line between the MEMS bridge and the ground plane. By choosing the appropriate length of the line l , the series resonant frequency can be lowered to the desired frequency range. This gives a high isolation inductively tuned MEMS shunt switch without the use of additional switches or tuned designs [5].

Isolation can, also, be improved by using high dielectric constant materials. It can be further improved by decreasing the thickness of the dielectric between the switch and the center conductor, thus increasing the on capacitance. However, the thin film should be sufficiently thick so that dielectric breakdown and current flow will not occur [3].

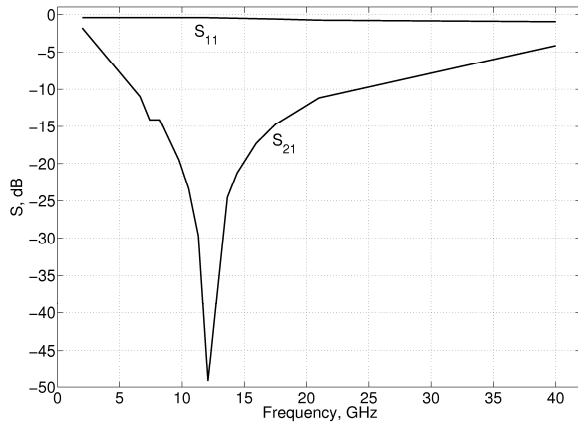


Fig. 8. Isolation S_{21} and return loss S_{11} in the down state condition.

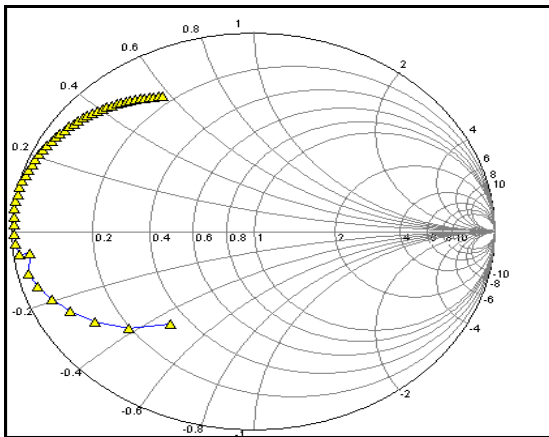


Fig. 9. The isolation illustrated in a Smith chart.

V. CONCLUSION

RF MEMS switches with actuation voltages of 2.5 V and excellent RF characteristics were designed and analyzed. The RF performances of the RF MEMS shunt switch were simulated based on the approach of the generalized transverse resonance diffraction as implemented in the 3D electromagnetic software package Em3ds10. The possibility of reduced order of dimension with this method allows rapid simulations without compromising the accuracies of computed results. The simulated performances were insertion loss, return loss, and isolation. The insertion loss obtained was very low, less than -0.2 dB at 12 GHz, while isolation was high with -50 dB at 12 GHz. These excellent RF characterizations prove that the switch is suitable for microwave applications or space systems where low loss, high

isolation, and low power consumption are essential.

REFERENCES

- [1] G. M. Rebeiz, *RF MEMS Theory, Design and Application*, John Wiley and Sons, New Jersey, 2003.
- [2] M. Farina and T. Rozzi, "A 3-D integral equation-based approach to the analysis of real-life MMICs—application to microelectromechanical systems," *IEEE Transactions on Microwave Theory and Techniques*, vol. 49, no. 12, pp. 2235-2240, December 2001.
- [3] S. P. Pacheco, Linda P. B. Katehi, and T. G. Nguyen, "Design of low actuation voltage RF MEMS switch," *Microwave symposium digest, IEEE MTT-S Int.* pp.165-168, 2000.
- [4] J. B. Muldavin and G. M Rebeiz, "High isolation CPW MEMS shunt switches-part 1: modeling," *IEEE Transactions on Microwave Theory and Techniques*, vol. 48, no. 6, pp. 1045-1052, 2000.
- [5] V. K. Varadan, K. J. Vinoj, and K. A. Jose, *RF MEMS and Their Applications*, John Wiley & Sons, Oxford, 2002.
- [6] T. Rozzi and M. Farina, "Advanced electromagnetic analysis of passive and active planar structures," *IEEE Circuits and Devices Magazine*, vol. 17, no. 6, pp. 40-41, Aug. 2002.
- [7] C. L. Goldsmith, Z. Yao, S. Eshelman, and D. Denniston, "Performance of low-loss RF MEMS capacitive switches," *IEEE Microwave and Guided Wave Letters*, vol. 8, no. 8, pp. 269-271, 1998.
- [8] MEM Research, available at: <http://www.memresearch.com/em3ds.htm>.



Haslina Jaafar is a staff of Universiti Putra Malaysia (UPM) in the Electrical and Electronics Engineering department. Her research interests are microelectronics devices and systems. She earned her bachelor degree in Electrical, Electronics, and Systems from National University of Malaysia (UKM) in 1999. Soon after, she graduated with a Master of Science (M.Sc.), majoring in microelectronics from the same university in 2001. She's now finishing her Ph.D. study at Universiti Science of Malaysia (USM) in Penang in Microelectromechanical Systems (MEMS) area.



Othman Sidek received the M.Sc. in Communication Engineering from UMIST, Manchester in 1984 and later Ph.D. in Info. Sys. Eng in CAD for VLSI from Bradford University in 1993.

He was a lecturer at the School of Electrical & Electronic Engineering since 1984 and was appointed as the Dean from 2002-2007. In late 2006, he founded a research centre, named CEDEC (Collaborative Micro-Electronic Design Excellence Centre) and was financed by the Ministry of Finance Malaysia. Since 2007, he is the Director of CEDEC with more than 25 researchers under his guidance.



Muhamad Azman Miskam received his M.Sc. degree in mechanical engineering from Universiti Sains Malaysia, Pulau Pinang, Malaysia in 2007. From 2000-2007, he was a

Tutor in the School of Mechanical Engineering, Universiti Sains Malaysia. Since 2008, he has been a research officer in the Collaborative Microelectronic Design Excellence Center, Universiti Sains Malaysia. His research area covers on Microelectromechanical System (MEMS) and Micro Power Generation.



Razi Abdul-Rahman received the B.S. degree in Mechanical Engineering from Carnegie Mellon University, Pittsburgh, PA, in 1996, and the M. S. degree in mechatronics engineering and the Ph.D. degree in engineering from Hamburg University of

Technology, Hamburg, Germany in 2002 and 2008, respectively. His current research interests include efficient computational methods for MEMS devices, particularly adaptive finite element methods for multi-nature systems.

A New UWB Slot Antenna with Rejection of WiMax and WLAN Bands

J. William and R. Nakkeeran

Department of Electronics and Communication Engineering
Pondicherry Engineering College, Puducherry – 605 014, India
wills.susan@gmail.com, rmakeeran@pec.edu

Abstract – This paper presents a compact coplanar waveguide (CPW) fed ultra wideband (UWB) planar slot antenna with the characteristics of dual band rejection. The antenna consists of a rectangular slot with triangular tuning stub. The band notching of WiMax (3.2-3.8 GHz, with VSWR 68 at 3.5 GHz) is achieved by inserting a ‘U’ slot in the ground plane and band-notching of WLAN 802.11a (5.1-5.9 GHz, with VSWR 14 at 5.5 GHz) is obtained by embedding a ‘U’ type slot in the triangular tuning stub. The characteristics of the proposed antenna are studied both numerically and experimentally, and the design parameters for achieving optimal operation of the antennas are also analyzed extensively. The size of the antenna is around 28mm (L) × 21mm (W) × 1.6mm (T). The prototype of the proposed antenna is fabricated for its optimal values and tested. The VSWR, radiation pattern and gain are measured and agree well with the simulation results. The proposed antenna is simple, easy to fabricate and can be integrated into any UWB system, which can work without interference from WiMax, WLAN, and HYPERLAN/2 systems.

Index Terms – CPW, dual band, slot antenna, UWB.

I. INTRODUCTION

The unlicensed UWB spectrum 3.1 GHz to 10.6 GHz was released in the year 2002 by the Federal Communications Commission (FCC) for commercial purposes. UWB, a short pulse communication system, gets much attention among the researchers due to its inherent properties of low power consumption, high data rate, and simple configuration [1]. With the rapid developments of such UWB systems, a lot of attention is being given to design the UWB

antennas. Designing an antenna to operate in the UWB band is quite a challenge because it has to satisfy the requirements such as ultra wide impedance bandwidth, omni directional radiation pattern, constant gain, high radiation efficiency, constant group delay, low profile, easy manufacturing, etc [2]. Interestingly, the planar slot antennas with CPW fed possess the above said features with simple structure, less radiation loss, less dispersion, and easy integration of monolithic microwave integrated circuits (MMIC) [3]. One of the major problems associated with the UWB system is the interference from the other narrow band communication systems, such as WiMax (3.3 GHz - 3.7 GHz), IEEE 802.11a (5.15 GHz - 5.35 GHz and 5.725 GHz - 5.825 GHz), and HYPERLAN/2 (5.15 GHz - 5.35 GHz and 5.47 GHz - 5.825 GHz), which are operated in the portion of UWB band.

To mitigate this effect, many antenna designs have been proposed in the literature [4-10]. Many techniques are, also, used to introduce notch band for rejecting the interference in the UWB slot antennas. It is done either by inserting half wavelength slits, stripes in the tuning stub [11], or inserting stub in the aperture connected to the ground planes [12], or inserting square ring resonator in the tuning stub [13], or inserting ‘L’ branches in the ground plane [14], or with complementary split ring resonator [15], or inserting strip in the slot [16]. All of the above methods are used for rejecting a single band of frequencies. However, to effectively utilize the UWB spectrum and to improve the performance of the UWB system, it is desirable to design the UWB antenna with dual band rejection. It will help to minimize the interference between the narrow band systems with the UWB system. Some methods are used to obtain the dual band rejection

of WiMax and WLAN bands in the literature [17-22]. In this paper, a new method is proposed to obtain the dual band rejection of frequency bands for WiMax, WLAN 802.11a, and HYPERLAN/2 systems. The WiMax frequency band is rejected by inserting a half wavelength 'U' slot in the ground plane at a center frequency of 3.5 GHz, and another 'U' type half wavelength slot at a frequency of 5.5 GHz is inserted in the triangular tuning stub to reject the desired WLAN frequency band. The simulation software used for this analysis is IE3D [23].

The paper is organized as follows: Section II brings out the geometry of the antenna. Simulation results and analysis are presented in Section III. In Section IV, obtained experimental results are given. Section V concludes the paper.

II. ANTENNA GEOMETRY

The structure of the antenna is shown in Fig. 1. The antenna consists of a rectangular slot with width 'W₁' and length 'L₁'. The tuning stub comprises a triangular patch with height 'H'. The distance between the tuning stub and the feed line is 'd', 'W', and 'L' are the overall width and length of the antenna respectively. In this study, the dielectric substance (FR4) with thickness of 1.6 mm with relative permittivity of 4.4 is chosen as substrate to facilitate printed circuit board integration. The 50 Ω characteristic impedance CPW feed is designed with fixed feed line width of 2.4 mm and 0.5 mm ground gap. The proposed antenna is designed to cover the entire UWB band with dual band rejection capability. The effective length of the rectangular slot introduced in the ground plane is approximately 0.5 λ_{eff} at the desired notch center frequency of 3.5 GHz.

The length 'L₂' of the slot in the ground plane is

$$L_2 = \frac{\lambda_{\text{eff}}}{2} = \frac{c}{2f_{n1}\sqrt{\epsilon_{\text{eff}}}}, \quad \epsilon_{\text{eff}} \approx \frac{\epsilon_r + 1}{2}, \quad (1)$$

where 'f_{n1}' is the centre frequency of the WiMax frequency band.

The length L₃ of the slot in the tuning stub is,

$$L_3 = \frac{\lambda_{\text{eff}}}{2} = \frac{c}{2f_{n2}\sqrt{\epsilon_{\text{eff}}}}, \quad (2)$$

where 'f_{n2}' is the centre frequency of the WLAN frequency band.

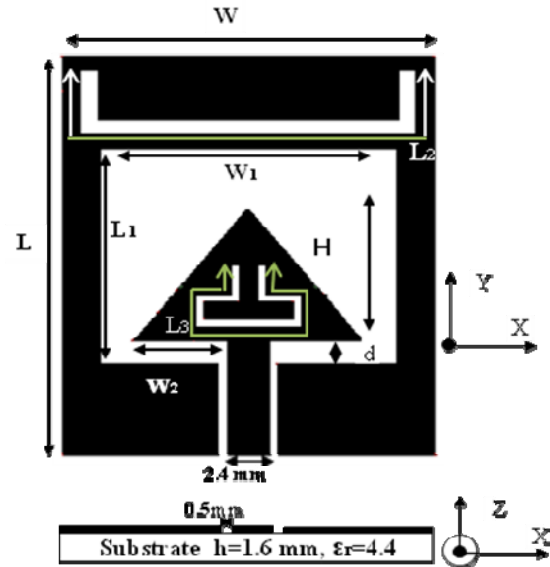


Fig. 1. Geometry of the proposed dual band notch slot antenna.

III. SIMULATED RESULTS AND ANALYSIS

The analysis and performance of the proposed antenna is explored by using IE3D for better impedance matching. The detailed parametric analysis of the UWB antenna is carried out and presented in our paper [24]. In order to evaluate the performance of the proposed antenna with dual band slots, the optimal parameter values of the antenna (without slot) suggested in that paper are considered. The final optimal parameter values of the antenna are listed in Table 1.

Table 1: Optimal parameter values of the antenna

Parameter	Description	Values
L	Length of the Antenna	28mm
W	Width of the Antenna	21mm
L ₁	Length of the Slot	15mm
W ₁	Width of the Slot	16.8mm
d	Feed gap Distance	1.6 mm
H	Height of the tuning stub	9.3 mm

However, to study the impact of the slots in the ground plane and in the tuning stub, the slot lengths 'L₂' and 'L₃' are varied and the simulated VSWR results of the proposed antenna is shown in Fig. 2. It clearly indicates that the rejection of dual bands of 3.2 GHz -3.8 GHz and 5.1 GHz- 5.9 GHz are achieved by inserting slots at appropriate

length in the ground plane and in the tuning stub. The current distribution, gain and group delay are, also, studied.

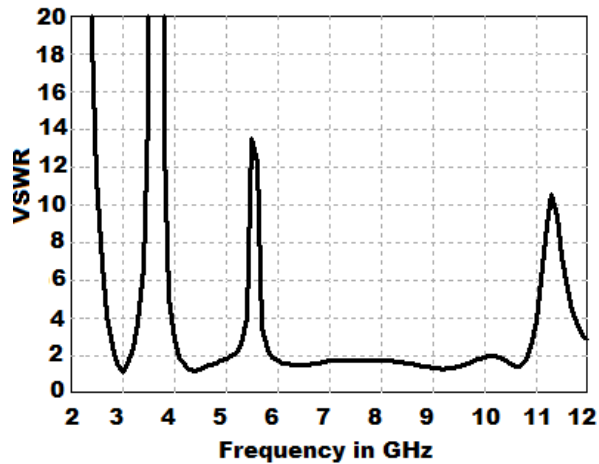


Fig. 2. Simulated VSWR of the proposed antenna.

A. Effect of ‘U’ slots

The effect of variation of the slot lengths is studied in this section. The length ‘ L_2 ’ of the ground slot is varied by keeping tuning slot length ‘ L_3 ’ as constant and the response is shown in Fig. 3. It is noticed that the variation of length ‘ L_2 ’ changes the notch center frequencies of the first rejected band. The optimal value chosen for this case is 28 mm.

The response curve for different slot lengths ‘ L_3 ’ in the tuning stub is shown in Fig. 4, which clearly indicates that slot length variation gives an impact on the variation of the notch center

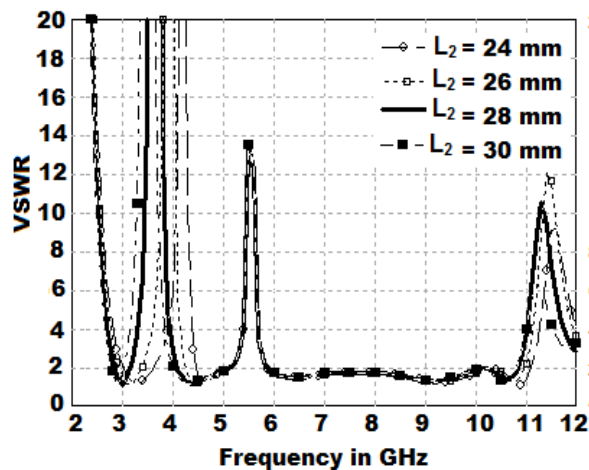


Fig. 3. Simulated VSWR for different ground slot lengths ‘ L_2 ’.

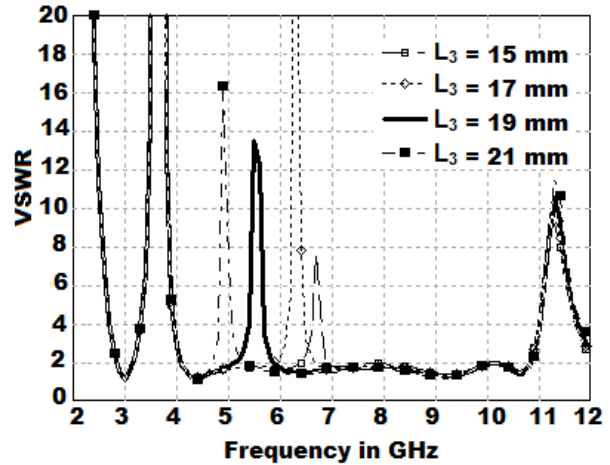


Fig. 4. Simulated VSWR for tuning stub slot lengths ‘ L_3 ’.

frequency for the second rejected band. The optimal value of ‘ L_3 ’ is 19 mm.

B. Gain

The simulated maximum gain of the proposed dual band notched UWB antenna is shown in Fig. 5. It is observed that there is a drop in gain at the notched frequencies of 3.5 GHz and 5.5 GHz.

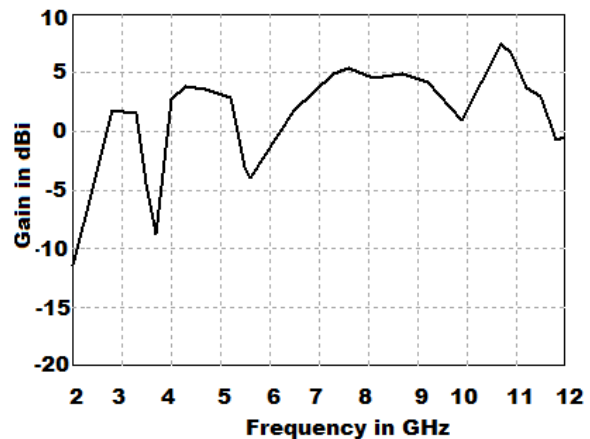


Fig. 5. Simulated maximum gain response.

C. Current distribution

The simulated current distribution at two designed notch center frequencies is presented in Fig. 6; as shown in this figure, the current distribution, at a frequency of 3.5 GHz, is mainly around the slot in the ground plane. This current distribution around the slot in the ground plane, which gives destructive disturbance to the radiating slot current distribution, is responsible for the notch in the particular frequency band.

Similarly at the notch center frequency of 5.5 GHz, the current distribution of the radiation slot is disturbed by the tuning stub slot which causes notching in the specific band. The current distribution for other operating frequencies 4.5 GHz and 9 GHz are, also, plotted, which confirms that on these frequencies current distribution is mainly around the slot and the tuning stub which is responsible for the better radiation at these frequencies.

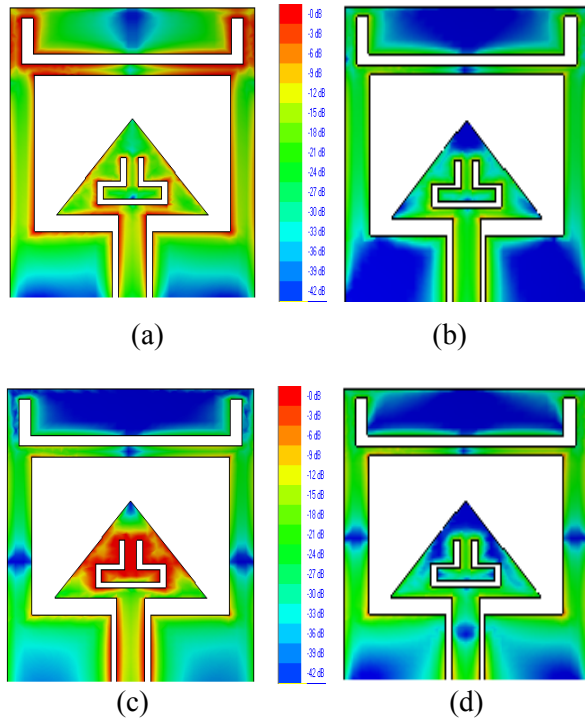


Fig. 6. Simulated current distribution at a) 3.5 GHz, b) 4.5 GHz, c) 5.5 GHz, and d) 9 GHz.

D. Radiation pattern

The radiation pattern for the E plane and H plane at frequencies 3.5, 4.5, 5.5, 7, and 9 GHz are simulated and displayed in Fig.7, which discloses that the directivity gain of the radiation pattern is reduced at the notch frequencies without affecting the shape of the radiation pattern. In the E plane, it is the bidirectional pattern and in the H plane, it is the omni directional pattern.

E. Group delay

The group delay ‘ τ ’ of the antenna is calculated from the phase of the computed ‘ S_{21} ’ by using the following equation and plotted in Fig. 8,

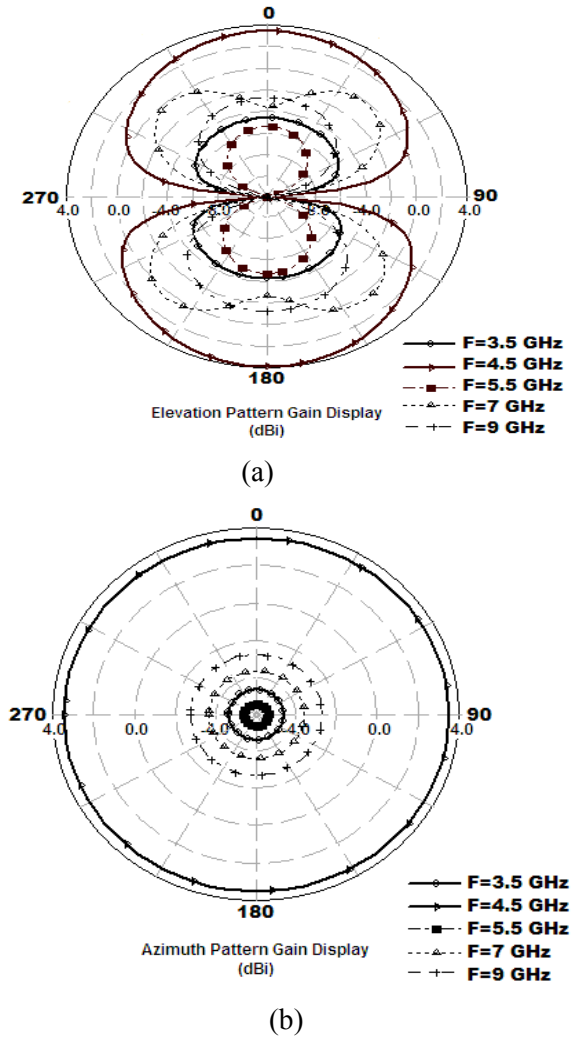


Fig. 7. Radiation patterns of the proposed antenna at 3.5, 4.5, 5.5, 7, and 9 GHz: a) E-Plane (yz-plane) and b) H-Plane (xz-plane).

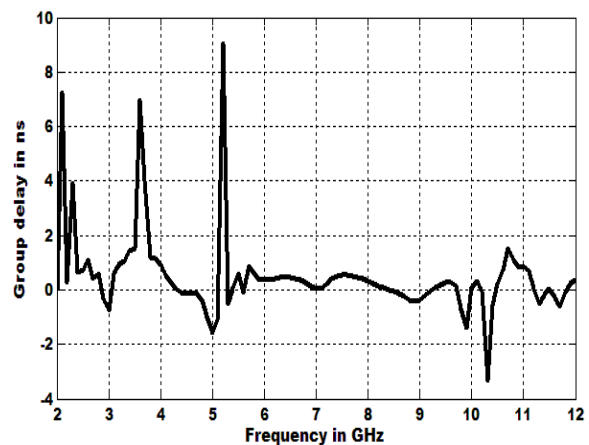


Fig. 8. Simulated group delay.

$$\tau = - \frac{d\phi}{df}, \tag{3}$$

where ‘ ϕ ’ is phase of S_{21} in radians /sec and ‘ f ’ is frequency in GHz. From Fig. 8, it is noticed that the variation in the group delay for the antenna is around 2 ns for the frequency range from 3.1 GHz to 10.6 GHz. There is a variation in the group delay response at the notch band which is due to notch behavior of the antenna.

IV. EXPERIMENTAL RESULTS AND DISCUSSION

The prototype of the proposed antenna shown in Fig. 1 was fabricated for its optimal values and tested, which is depicted in Fig. 9. Using Hewlett Packard Network Analyzer (HP8757D) the VSWR is measured and plotted. The gain and radiation pattern of the antenna is measured by using VNA Agilent HP 5230A.

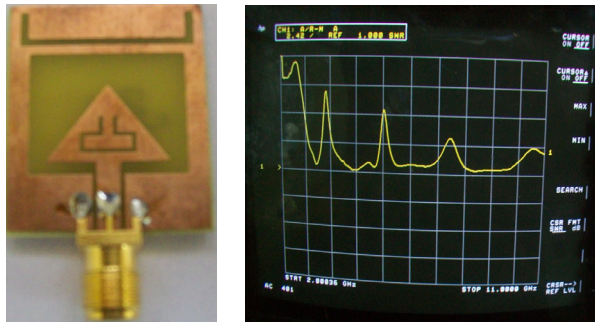


Fig. 9. Fabricated antenna and its measured results.

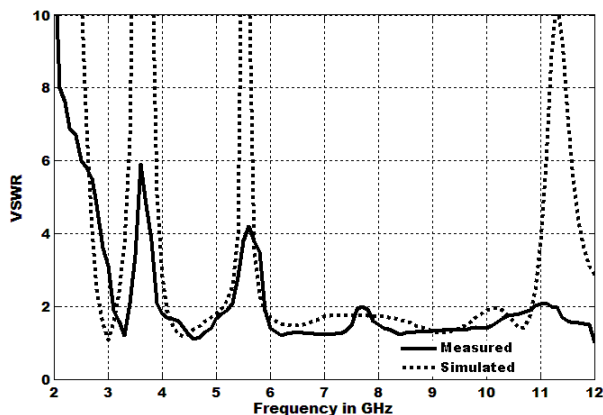


Fig. 10. VSWR comparison of the proposed antenna.

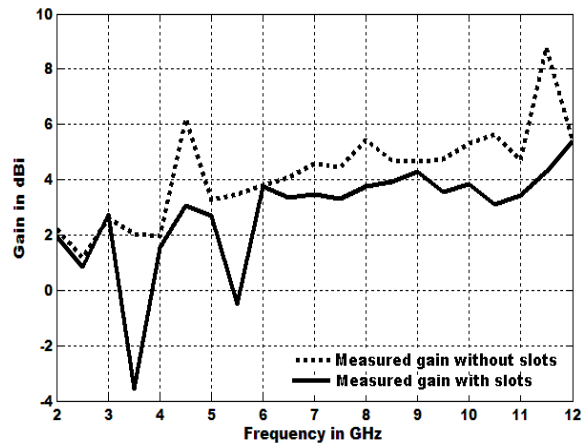
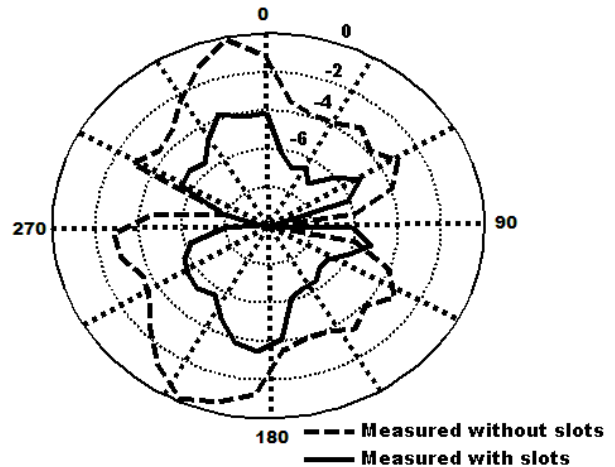
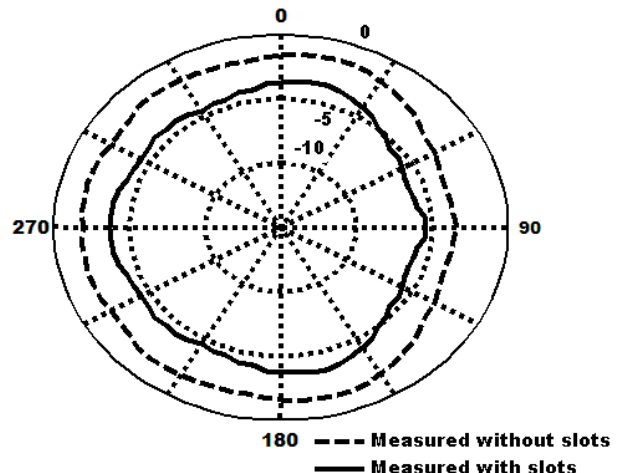


Fig. 11. Measured gain comparison.



(a)



(b)

Fig. 12. Measured radiation pattern at 6.5 GHz: a) E-Plane (yz-plane) and b) H-Plane (xz-plane).

The measured result is shown in Fig. 10 which ensures that the measurement result is in good agreement with the simulation. The discrepancy between the measured and the simulated result seen in Fig. 10 might be due to the effect of soldering or fabrication tolerance. The simulation results have been obtained by assuming coplanar input port, whereas practically a SMA connector was used, the imperfect transition between a SMA feed to coplanar would introduce losses [25]. However, the measured bandwidth is 7.7 GHz (3.1-10.8 GHz), which is moderately close to the simulated impedance bandwidth, 8 GHz (2.8 - 10.8 GHz).

The maximum gain of the proposed antenna is measured and compared with the gain for an antenna without slot. The comparison is shown in Fig. 11, which implies that there is a variation in the gain at the notch frequency bands due to the introduction of the slots in the design.

The radiation pattern of the designed antenna at a frequency 6.5 GHz is measured and plotted in Fig. 12. The figure shows the measured radiation pattern with slot and without slots. The E plane and H plane radiation patterns with slot show a drop in gain when compared to patterns without slot; this may be due to the effect of introduction of the slots in the design.

V. CONCLUSION

In this paper, a planar UWB slot antenna with dual band rejection is presented. Dual band rejection of WiMax and WLAN is achieved by inserting slots at appropriate lengths in the ground plane and in the tuning stub. The antenna was fabricated using FR4 substrate, characterized by measuring VSWR, radiation pattern and gain, and compared with the simulation results. The measurement results are in good agreement with simulation. The proposed antenna achieves good impedance bandwidth covering frequency range from 2.8 GHz to 10.8 GHz with VSWR < 2 except the bands of WiMax and WLAN 802.11a. This type of antenna configuration would be quite useful for UWB indoor applications with no interference from WiMax, WLAN, and HYPERLAN/2 systems when they coexist with a UWB system.

REFERENCES

- [1] FCC News release, FCC NEWS (FCC 02-48), Feb. 14, 2002.
- [2] M. Ghavami, L.B. Michael, and R. Kohno, *Ultra Wideband Signals and Systems in Communication Engineering*, New York: John Wiley and Sons, USA, 2004.
- [3] R. N. Simons, *Coplanar waveguide Circuits Components and Systems*, John-Wiley & Sons, New York, 2001.
- [4] I.-J. Yoon, H. Kim, H. K. Yoon, Y. J. Yoon, and Y. H. Kim, "Ultra-wideband tapered slot antenna with band cutoff characteristic," *Electronics Letters*, vol. 41, no. 11, pp. 629-630, May 2005.
- [5] A. M. Abbosh, M. E. Bialkowski, J. Mazierska, and M. V. Jacob, "A planar UWB antenna with signal rejection capability in the 4-6 GHz band," *IEEE Microwave and Wireless Comp. Letters*, vol. 16, no. 5, pp. 278-280, May 2006.
- [6] K. Bahadori and Y. Rahmat-Samii, "Miniaturized elliptic-card UWB antenna with WLAN band rejection for wireless communications," *IEEE Trans. Antennas and Propag.*, vol. 55, no. 11, pp. 3326-3332, Nov. 2007.
- [7] C.-Y. Hong, C.-W. Ling, I. Y. Tarn, and S. J. Chung, "Design of a planar ultra-wideband antenna with a new band-notch structure," *IEEE Trans. Antennas and Propag.* vol. 55, no. 12, pp. 3391-3397, Dec. 2007.
- [8] L. Wang, W. Wu, X.-W. Shi, F. Wei, and Q. -L. Huang, "Design of a novel monopole UWB antenna with a notched ground," *PIER*, vol. 5, pp. 13-20, 2008.
- [9] J.-Y. Sze and J.-Y. Shiu, "Design of band-notched ultrawideband square aperture antenna with a hat-shaped back-patch," *IEEE Trans. Antennas and Propag.*, vol. 56, no. 10, pp. 3311-3314, Oct. 2008.
- [10] N. Farrokh-Heshmat, J. Nourinia, and C. Ghobadi, "Band-notched ultra-wideband printed open-slot antenna using variable on-ground slits," *Electronics Letters*, vol. 45, no. 21, pp. 1060-1061, Oct. 2009.
- [11] Y.-C. Lin and K.-J. Hung, "Compact ultrawideband rectangular aperture antenna and band-notched designs," *IEEE Trans. Antennas Propag.*, vol. 54, no. 11, pp. 3075-3081, Nov. 2006.
- [12] H. K. Yoon, Y. Lim, W. Lee, Y. J. Yoon, S. M. Han, and Y. Kim, "UWB wide slot antenna with band-notch function," *Proc. IEEE Antennas and Propag. Society Intl Symposium*, pp. 3059-3062, July 2006.
- [13] W.-J. Lui, C.-H. Cheng, and H.-B. Zhu, "Improved frequency notched ultra wideband slot antenna using square ring resonator," *IEEE Trans.*

Antennas Propag., vol. 55, no. 9, pp. 2445-2450, Sep. 2007.

- [14] Y. Cai and Z. Feng, "A UWB antenna with novel L branches on ground for band-notching application," *Proc. of IEEE Intl. Conference on Microwave and Millimeter Wave Tec.*, vol. 4, pp. 1654-1657, April 2008.
- [15] T.-N. Chang and M.-C. Wu, "Band-notched design for UWB antennas," *IEEE Antennas Wirel. Propag. Letters*, vol. 7, pp. 636-639, 2008.
- [16] C.-Y. Huang, S.-A. Huang, and C.-F. Yang, "Band-notched ultra-wideband circular slot antenna with inverted C-shaped parasitic strip," *Electronics Letters*, vol. 44, no. 15, pp. 891-892, July 2008.
- [17] Q.-X. Chu and Y.-Y. Yang, "3.5 / 5.5 GHz dual band-notch ultra-wide band antenna," *Electronics Letters*, vol. 44, no. 3, pp. 172-174, Jan. 2008.
- [18] H.-J. Zhou, B.-H. Sun, Q.-Zh. Liu, and J.-Y. Deng, "Implementation and investigation of U-shaped aperture UWB antenna with dual band-notched characteristics," *Electronics Letters*, vol. 44, no. 24, pp. 172-174, Nov. 2008.
- [19] S. Zhou, J. Ma, and J. Deng, "A novel dual band-notched ultra wideband," *Journal of Electromagn. Waves and Appln.*, vol. 23, pp. 57-63, 2009.
- [20] J. Y. Deng, Y. Z. Yin, J. Ma, and Q. Z. Liu, "Compact ultra-wideband with dual band-notched characteristics," *Journal of Electromagnetic Waves and Appln.*, vol. 23, pp. 109-116, 2009.
- [21] X. Li, L. Yang, S. X. Gong, and Y. J. Yung, "A novel tri band-notched monopole antenna," *Journal of Electromagnetic Waves and Appln.*, vol. 23, pp. 139-147, 2009.
- [22] K. S. Ryu and A. A. Kishk, "UWB antenna with single or dual band-notches for lower WLAN Band and upper WLAN band," *IEEE Trans. Antennas Propag.*, vol. 57, no. 12, pp. 3942-3950, Dec. 2009.
- [23] IE3D 14, Zeland Software, Ins., Fremont, USA.
- [24] J. William and R. Nakkeeran, "A new compact CPW-fed wideband slot antenna for UWB applications," *Proc. of IEEE First Himalayan Intl. Conference on Internet*, Nov. 2009.
- [25] K.-P. ma, Y. Qian, and T. Itoh, "Analysis and applications of a new CPW- slot line transition," *IEEE Transactions on Microwave theory and Techniques*, vol. 47, pp. 426-432, April 1999.



J. William received his B.E. degree in Electronics and Communication from Bharathidasan University, Tamilnadu, India, and the M. Tech. degree in Communication Systems from the National

Institute of Technology (N.I.T), Trichy, India, in 1991 and 2006, respectively. He is currently working towards the Ph.D. degree at Pondicherry Engineering College, Pondicherry, India. He is a life member of ISTE and IE (I) and a member of IEICE and EurApp. His current research interest is in the area of coplanar waveguide feed antennas and printed slot antennas for UWB.

R. Nakkeeran received his B.Sc. Degree in Science and B.E. degree in Electronics and Communication Engineering from the Madras University in 1987 and 1991, respectively, and his M.E. degree in Electronics and Communication Engineering (diversification in Optical Communication) from the Anna University in 1995. He received his Ph.D. from Pondicherry University in 2004. Since 1991, he has been working in the teaching profession. Presently, he is Assistant Professor at Pondicherry Engineering College. He is a life member of IETE, ISTE, OSI, and IE (I). Also, he is a member of OSA, SPIE, and IEEE. He has published seventy five papers in National and International Conference Proceedings and Journals. He has co-authored a book, published by PHI. His areas of interest are optical communication, networks, antennas, electromagnetic fields, and wireless communication.

Microstrip Inductor Design and Implementation

Abdullah Eroglu

Department of Engineering
Indiana University – Purdue University Fort Wayne, Fort Wayne, IN 46805, USA
eroglua@ipfw.edu

Abstract — High frequency (HF) microstrip spiral inductor design using analytical formulation with network model and numerical simulation with planar electromagnetic simulator, Sonnet, are given for high power RF application. The simplified lumped element equivalent network model parameters for the spiral inductor are used to obtain the initial dimensions of the spiral inductor for simulation. The spiral inductor is then simulated with planar electromagnetic simulator, Sonnet, using the geometry constructed with the physical dimensions obtained from the network model for the desired inductance value. The parametric study of the spiral inductor is conducted to investigate the variation on its quality factor, self resonance frequency and inductance value. The spiral inductor is implemented on a ceramic substrate and measured. The measurement, simulation, and analytical results are found to be close.

Index Terms — HF, inductor, microstrip, RF, spiral.

I. INTRODUCTION

Spiral type planar inductors are commonly used in communication systems as a component due to several of their benefits and practical implementation. Spiral inductor design at microwave frequencies in the literature [1-11] is extensively investigated and equivalent models have been reported when the spiral inductor is implemented on a silicon material [12-13] or gallium-arsenide (GaAs) [14-16]. However, the lack of literature in the design of spiral inductors at HF (3MHz –30MHz) range for RF applications constitutes an important problem for high power RF applications. HF is commonly used in submarine communication, semiconductor wafer processing, and plasma applications. Spiral

inductors, specifically for these applications, must be able to operate under very high power conditions. Under such high power, spiral inductors should exhibit reliable thermal profile, desired inductance value and low loss. If these characteristics are not demonstrated, changes in the component value can cause catastrophic failures in the RF systems. Accurate design technique, with reliable thermal operation using thermally highly conductive and electrically low loss material, can provide optimum spiral inductor operation.

In this paper, simplified and accurate design method for the spiral inductor is presented using network model for high power RF applications. The model is used to obtain the physical dimensions of the spiral inductor for the desired inductance value. The physical dimensions are then used to construct the geometry in the planar electromagnetic simulator, Sonnet. Planar electromagnetic simulator, Sonnet, is also used to characterize the spiral inductor with the parametric study by varying the trace width and spacing between traces. The parametric study is used to understand the effect of these parameters on the quality factor, inductance value, and self resonance frequency of the inductor. Spiral inductor is then built using alumina substrate and measured. The analytical, simulation, and measurement results are found to be close. The analytical model, proposed in this paper, is, also, used to study the effect of the physical dimensions and number of turns on spiral inductance value, quality factor, and the resonant frequency. Their effects on critical spiral inductor design parameters are detailed.

II. ANALYTICAL FORMULATION

The layout of the general microstrip rectangular spiral inductor is illustrated in Fig. 1. In this layout, w represents the width of the trace, l_1 and l_2 are the length of the outside edges, s is the spacing

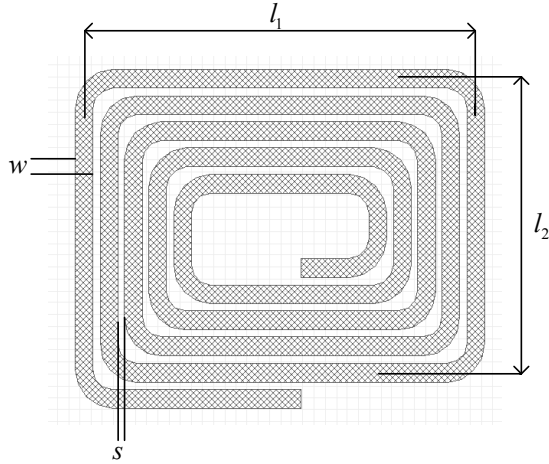


Fig. 1. Microstrip model of the spiral inductor.

between the traces. It is assumed that the substrate material is alumina (Al_2O_3) with thickness h . The accurate modeling of the spiral inductor at HF range can be done using the π network shown in Fig. 2. In the π network, total inductance, coupling capacitances, substrate capacitance, are all taken into account. The capacitance of the spiral inductor is calculated using the effect of odd mode, even modes. This approach gives more realistic results for the physical representation of the spiral inductor.

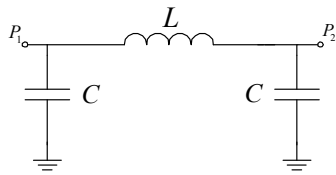


Fig. 2. Lumped-element model for spiral inductor.

In the lumped element model, L represents the total inductance value. The accurate inductance calculation at the HF range can be obtained using Greenhouse's method described in [17]. The total inductance of the spiral inductor including the effect of mutual couplings is given as

$$L = L_0 + \Sigma M \quad (1)$$

L_0 is the sum of the self inductances for each trace.

ΣM takes into account of all mutual inductances in the structure. Equation given in (1) can be written more explicitly for any number of turns for a rectangular spiral inductor as

$$L_i = 0.0002l_i \left[\ln \left(2 \frac{l_i}{GMD} \right) - 1.25 + \frac{AMD}{l_i} + \frac{\mu}{4} T \right] \quad (2)$$

and

$$M_{ij} = 0.0002l_i Q_i \quad (3)$$

AMD is the arithmetic mean distance and GMD is used for the geometric distance. C is the capacitance that include the effect of odd mode, even mode and interline coupling capacitances between coupled lines of the spiral inductor. The detailed calculation of the capacitances is given in [18]. The substrate losses and conductor losses are ignored due to the low operational frequency.

One port measurement network for the spiral inductor using the model proposed in Fig. 2 is shown in Fig. 3 below

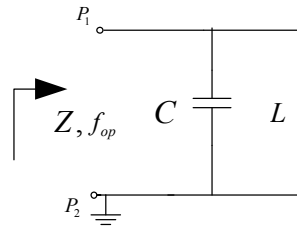


Fig. 3. One port measurement circuit.

The physical dimensions of the microstrip spiral inductor are given in Table 1. All the dimensions are given in mils.

Table 1: Physical dimensions of the spiral inductor

Trace Width w	Spacing s	Horizontal Trace Length l_1	Vertical Trace Length l_2	Copper Thickness t	
80	30	1870	1450	4.2	
Dielectric Material	Dielectric Permittivity ϵ_r	Dielectric Thickness h	Number of Turns n	Bridge Height h_b	Bridge Width w_b
Al_2O_3	9.8	100	6.375	100	350

The inductance value of the spiral inductor using analytical model with the dimensions in Table 1 is calculated to be 590nH with the algorithm developed. In addition to the calculation

of the spiral inductance value, we used our analytical model to study the effect of trace width, spacing, loop area and number of turns on inductance value, quality factor, and resonant frequency. This is accomplished by including the conductor and dielectric losses in the simplified analytical model. The conductor loss is modeled as series resistance R with inductance L and given by

$$R = \frac{2}{w} \sqrt{\frac{\pi f \mu_c}{\sigma}} \quad [\Omega/m], \quad (4)$$

where μ_c and σ are the permeability and conductivity of the conductor used as trace. The substrate loss is modeled as R_p and given by

$$R_p = \frac{\rho l}{wh} \quad [\Omega/m], \quad (5)$$

where h is the thickness of the substrate and ρ is given as $\rho = 0.01 [\Omega \cdot m]$ for Al_2O_3 . Table 2 below illustrates the calculated values of the critical spiral design parameters such as inductance, quality factor, and resonant frequency by varying trace width, outer edge dimensions signifying the change in the loop area, spacing, and number of turns.

Table 2: Study of physical dimensions

	Analytical							
	w	s	I1	I2	Turns	L	Q	Fr
Unit	mils	mils	mils	mils		nH		MHz
Orig. Ind	80	30	1450	1870	6.5	590.05	68.73	29.73
Mod 1	60	30	1450	1870	6.5	958.84	34.21	27.15
Mod 2	80	20	1450	1870	6.5	734.6	47.18	29.48
Mod 3	80	30	1880	2411	6.5	1243	12.87	20.27
Mod 4	80	10	1450	1870	7.5	1075	10.94	19.75

It has been seen that the higher inductance value can be obtained by reducing the width of the trace, reducing the spacing between the traces, increasing the number of turns and reducing the spacing, or increasing the loop area of the inductor by changing the outer edge dimensions. Although each of these changes increases the inductance value of the spiral inductor, it has to be noted that they have several undesired side effects. In every change, unless some other change is implemented for compensation, the quality factor and the resonant frequency of the inductor are reduced. The intensity of the reduction varies based on the change implemented. Specifically, for high power applications, the higher quality factor is needed and it guarantees better thermal management

during operation. Thermally better designed spiral inductors give resonant frequencies at least three times higher than their operational frequencies. The specific spiral inductor designed in this paper is used as part of power amplifier and capable of handling more than 100W. Commercially available spiral inductors can only handle very low power levels and cannot be used for high power applications. In addition, the trace width and spacing should be designed to handle the amount of the current flow and the potential occurring between the traces. As a result, the analytical method proposed in this paper can be used to design and implement spiral inductors for high power RF applications reliably and accurately.

III. MEASUREMENT AND SIMULATION RESULTS

The spiral inductor using the dimensions in Table 1 is simulated with the method of moment based planar electromagnetic simulator Sonnet. The operational frequency is chosen to be 13.56MHz. The 3D layout of the simulated structure is illustrated in Fig. 4. The input port or port 1 is connected via bridge for inductance measurement. The bridge height and width are given in Table 1. The effect of the bridge at the frequency of the operation is minimal due to its increased width.

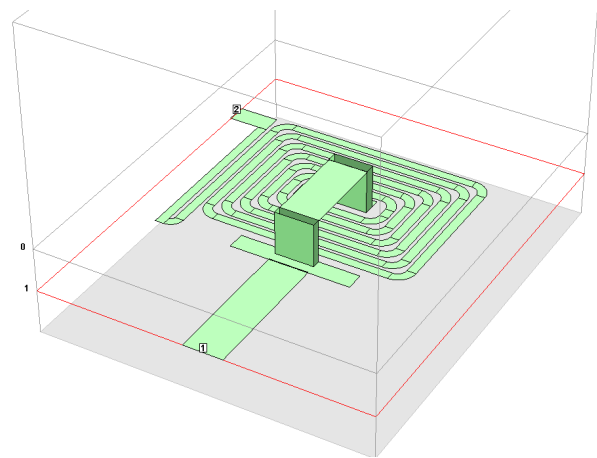


Fig. 4. 3D model of the simulated spiral inductor.

The traces as seen in Fig. 4 are segmented for parametric study to understand the effect of width and spacing on the self resonant frequency and the quality factor of the spiral inductor. One of the unique features of the planar electromagnetic

simulator is the visualization of the current distribution on the spiral structure. This is specifically important for high power applications to adjust the necessary spacing between traces to prevent any possible arcs during the operation. As seen from Fig. 5, the current density on the bridge which is designed to have minimal impact on the device performance and overall inductance is lowest. The current density increases as it gets closer to the edges of each trace. It becomes maximum at the edges. This is why during the implementation of the spiral inductor the corners are rounded to increase the creepage distance to prevent potential arcs.

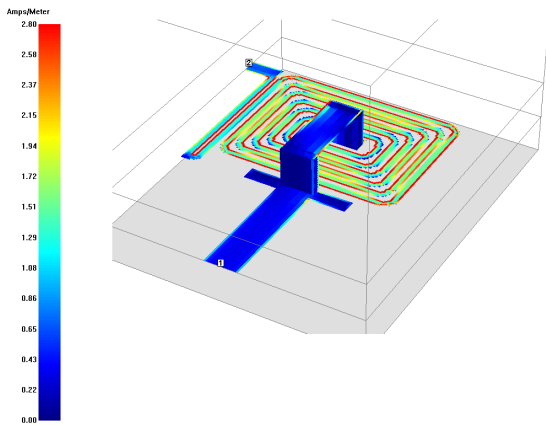


Fig. 5. Current density of the spiral inductor.

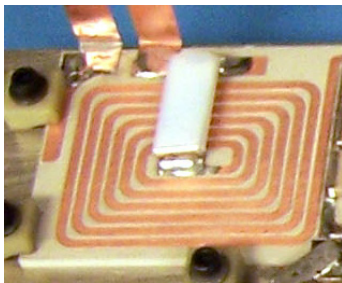


Fig. 6. Spiral inductor is constructed on 100 mil alumina substrate.

The inductance value of the spiral inductor is simulated and obtained as 588.6 nH at the operational frequency which is 13.56 MHz. The measured inductance value at this frequency is found to be 594.91 nH. The spiral inductor that is simulated and illustrated in Fig. 4 is built on 100 mil Al_2O_3 substrate as shown in Fig. 6. The

higher inductance values can be obtained by increasing the number of turns, decreasing the width of the trace. The self-resonant frequency of the spiral inductor is found to be 37.8MHz. In spiral inductor design, rule of thumb is to have self resonant frequency approximately 3 times higher than the operational frequency which guarantees optimal operation. As a result, the self resonant frequency that is obtained is just below the desired value. The simulation results illustrating the inductance value and self resonant frequency is given in Fig. 7.

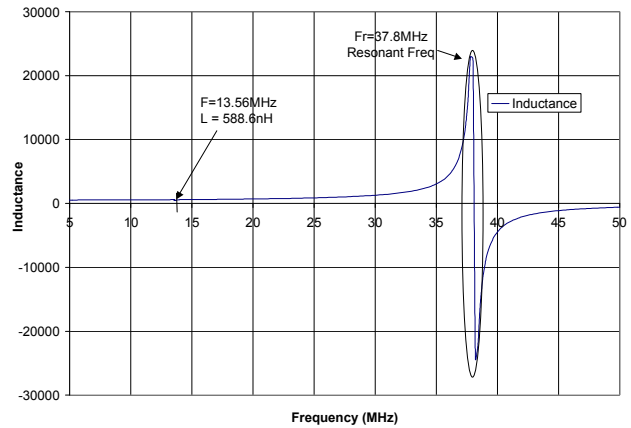


Fig. 7. Simulation results showing inductance value and resonant frequency of the spiral inductor.

The quality factor of the spiral inductor is found to be 72.6 at 13.56 MHz. As illustrated in Fig. 8, the quality factor reaches almost peak value at the operational frequency. At resonance, the quality factor is minimum as expected.

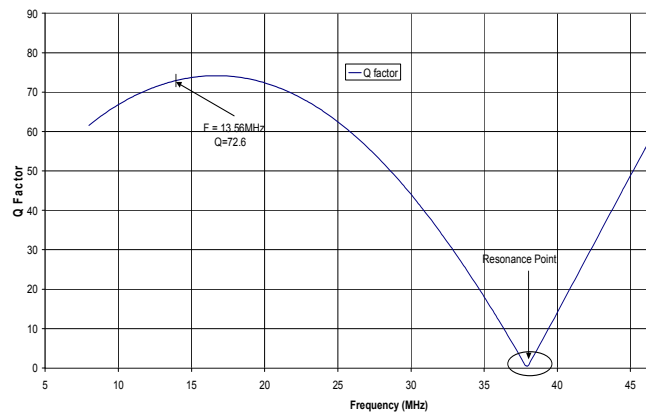


Fig. 8. Simulation results showing the quality factor of the spiral inductor.

Electromagnetic simulator, Sonnet, is used to understand the effects of spacing and width of the traces as mentioned before. It is found out that the self resonant frequency of the spiral inductor can be increased by increasing the trace width and reducing the spacing between each trace. The illustration of this is given in Fig. 9. In Fig. 9, the original width, which is 80mil, is compared with the optimized width, which is 94.32mil. The spacing in the original design is 30mils whereas the spacing in the optimized design is 15.68mil. The original self resonant frequency is increased to be greater than 50MHz with the proposed optimization.

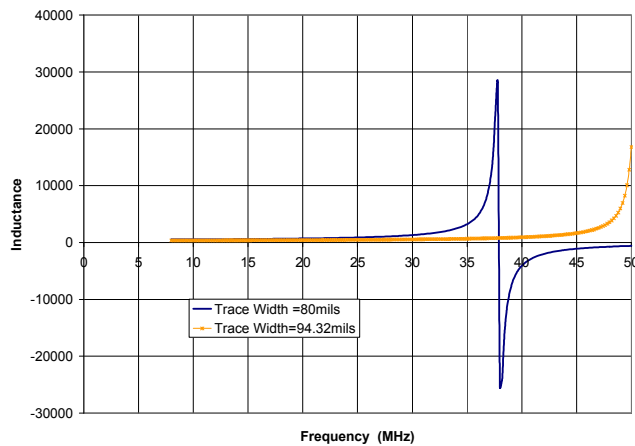


Fig. 9. Comparison of self resonant frequency of the spiral inductor.

Although, the self resonant frequency is increased to be greater than 50MHz, we need to investigate the effect of the changes that are done on the physical dimensions on the quality factor, return loss, insertion loss, and the inductance value of the spiral inductor to minimize the potential problems during operation. Figure 10 shows the comparison of the quality factor of the spiral inductor with original design and optimized design.

As shown in Fig. 10, the quality factor of the inductor is reduced to 68. This corresponds to 6.3% reduction in the quality factor value.

High quality factor is desirable to prevent any thermal problems during the operation of the device. Since, the substrate that is used has very high thermal conductivity with minimal substrate loss; the level of the reduction in the quality factor will not adversely effect the thermal profile of the spiral inductor. The change in the inductance value

versus frequency when the physical dimensions are optimized to increase self resonant frequency is illustrated in Fig. 11.

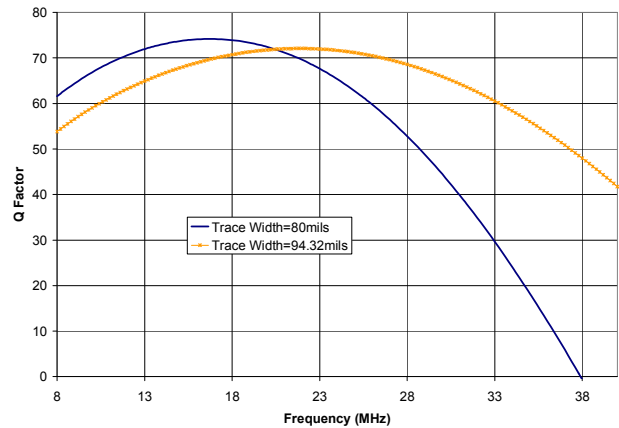


Fig. 10. Comparison of quality factor of the spiral inductor.

The changes that are implemented reduce the inductance value at the frequency of operation from 594.91nH to 390nH. This is approximately 34% reduction and is significant in comparison to the original inductance value. However, this can be compensated by a shunt capacitor that is connected

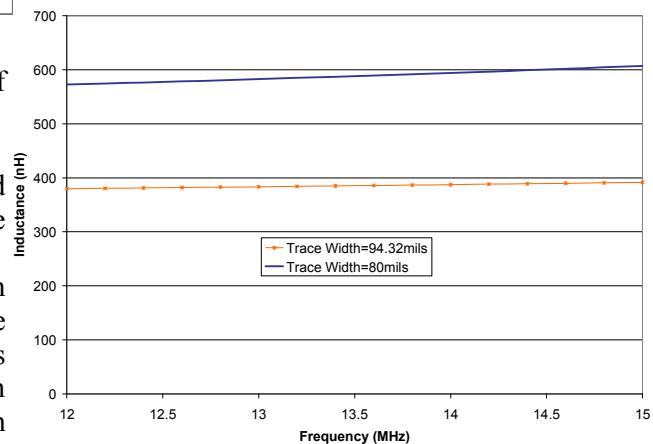


Fig. 11. Comparison of inductance value of the spiral inductor.

by a shunt capacitor that is connected between the ports of the spiral inductor. The capacitor that is required to bring 390nH up to 590.3nH is 120pF. This capacitor value is a standard value that can be easily found.

As a result, it has been shown that the spiral inductor can be optimized for the self resonant

frequency using electromagnetic simulator with the proposed changes in the spacing and width of the traces without effecting the operation of the spiral inductor. The optimization on quality factor is, also, possible using the method outlined. In addition, the analytical model proposed in this paper can be used to accurately and reliably design spiral inductor for the desired inductance value, quality factor and the resonant frequency for high power RF applications at the HF range.

IV. CONCLUSION

Microstrip spiral inductors using the simplified equivalent circuit is designed, simulated, built, and measured at the HF range for high power RF applications. The measured, simulation, and analytical results are found to be very close. The parametric study of the spiral is conducted using planar electromagnetic simulator, Sonnet. It has been shown that the self resonant frequency of the spiral inductor can be increased by increasing the trace width and reducing the spacing between each trace. Increased self-resonant frequency is a very important feature for several RF applications to provide optimal operation like quality factor. The analytical method proposed in this paper is also used to study the effect of physical dimensions of the inductor including trace width, spacing, loop area, and number of turns on critical spiral inductor design parameters such as inductance value, resonant frequency, and quality factor. The results of this work can be used in RF applications at the HF range where high power is needed.

REFERENCES

- [1] C. P. Yue, C. Ryu, J. Lau, T. H. Lee, and S. S. Wong, "A physical model for planar spiral inductors on silicon," *IEDM Tech. Dig.*, pp. 155–158, Dec. 1996.
- [2] R. D. Lutz, Y. Hahm, A. Weisshaar, and V.K. Tripathi, "Modeling of spiral inductors on lossy substrates for RFIC applications," *Proc. 1998 Radio Frequency Integrated Circuits Symp.*, pp. 313–316, June 1998.
- [3] K. B. Ashby, I. A. Koullias, W. C. Finley, J. J. Bastek, and S. Moinian, "High Q inductors for wireless applications in a complementary silicon bipolar process," *IEEE J. Solid-State Circuits*, vol. 31, pp. 4–9, Jan. 1996.
- [4] A. M. Niknejad and R. G. Meyer, "Analysis, design and optimization of spiral inductors and transformers for Si RF IC's," *IEEE J. Solid-State Circuits*, vol. 33, pp. 1470–1481, Oct. 1998.
- [5] S. Jenei, B. Nauwelaers, and S. Decoutere, "Physics-based closed-form inductance expression for compact modeling of integrated spiral inductors," *IEEE J. Solid-State Circuits*, vol. 37, no. 1, pp. 579–586, Jan. 2002.
- [6] Y. Cao, R. Groves, X. Huang, N. Zamdmer, J. Plouchart, R. Wachnik, T. King, and C. Hu, "Frequency-independent equivalent-circuit model for on-chip spiral inductors," *IEEE J. Solid-State Circuits*, vol. 38, no. 3, pp. 419–426, Mar. 2003.
- [7] A. Nieuwoudt, M. S. McCorquodale, R. T. Borno, and Y. Massoud, "Accurate analytical spiral inductor modeling techniques for efficient design space exploration," *IEEE Electron Device Letters*, vol. 27, no. 12, Dec. 2006.
- [8] S. Mohan, M. delMar Hershenson, S. Boyd, and T. Lee, "Simple accurate expressions for planar spiral inductances," *IEEE J. Solid-State Circuits*, vol. 34, no. 10, pp. 1419–1424, Oct. 1999.
- [9] J. Crols, P. Kinget, J. Craninckx, and M. S. J. Steyaert, "An analytical model of planar inductors on lowly doped silicon substrates for high frequency analog design up to 3 GHz," *Symp. VLSI Circuits Dig. Tech. Papers*, pp. 28–29, June 1996.
- [10] F. Freschi and M. Repetto, "A General Framework for Mixed Structured/Unstructured PEEC Modelling," *ACES Journal*, vol. 23, no. 3, pp. 200–206, 2008.
- [11] D. Elsherbeni, L. Jordan, E. Hutchcraft, D. Kajfez, and R. K. Gordon, "The design of a TRL calibration kit for microstrip and its use for measurement and modeling of active and passive RF components," *ACES Journal*, vol. 23, no. 3, pp. 276–285, 2008.
- [12] D. Lovelace, N. Camilleri, and G. Kannell, "Silicon MMIC inductor modeling for high volume, lowcost applications," *Microw. J.*, pp. 60–71, Aug. 1994.
- [13] C. P. Yue and S. S. Wong, "A study on substrate effects of silicon-based RF passive components," *MTT-S Int. Microwave Symp. Dig.*, pp. 1625–1628, June 1999.

- [14]I. J. Bahl, "Improved quality factor spiral inductor on GaAs substrates," *IEEE Microwave Guided Wave Lett.*, vol. 9, pp. 398–400, Oct. 1999.
- [15]R. P. Ribas, J. Lescot, J. L. Leclercq, N. Bernnouri, J. M. Karam, and B. Courtois, "Micromachined planar spiral inductor in standard GaAs HEMT MMIC technology," *IEEE Electron Device Lett.*, vol. 19, pp. 285–287, Aug. 1998.
- [16]H. Takenaka and D. Ueda, "0.15 μ mT-shaped gate fabrication for GaAs MODFET using phase shift lithography," *IEEE Trans. Electron Devices*, vol. 43, pp. 238–244, Feb. 1996.
- [17]H. M. Greenhouse, "Design of planar rectangular microelectronic inductors," *IEEE Transactions on Parts, Hybrids and Packaging*, vol. PHP-10, pp.101-109, June 1974.
- [18]A. Eroglu and J. K. Lee, "The complete design of microstrip directional couplers using the synthesis technique," *IEEE Transactions on Instrumentation and Measurement*, vol. 12, pp. 2756-2761, Dec. 2008.



Abdullah Eroglu received the doctor of philosophy degree (Ph.D.) in 2004 in Electrical Engineering from the Electrical Engineering and Computer Science Department of Syracuse University, Syracuse, NY.

From 2000 to 2008, he worked as Senior RF design engineer at MKS Instruments where he was involved with the design of RF power amplifiers and systems. He is the recipient of an outstanding graduate student award from the Electrical Engineering and Computer Science Department of Syracuse University in 2004. Since 2008, he is assistant professor of electrical engineering at the Engineering Department of Indiana University - Purdue University Fort Wayne (IPFW), IN, USA. He was a faculty fellow at the Fusion Energy Division of Oak Ridge National Laboratory during the summer of 2009 and is the recipient of Excellence in Research Award from Engineering, Technology, and Computer Science (ETCS) College of IPFW in 2010. He has over 40 journal and conference publications and a patent. He is the author of the book: *Wave Propagation and Radiation in Gyrotropic and Anisotropic Media*. He is on the Editorial Board of Journal of Communications and Network and Recent Patents on Electrical Engineering.

Analysis of Dual-Mode Microstrip Patch Filter using Multiscale Wave Concept Iterative Process

Taoufik Ibn Elhaj Brahim¹, Hassen Zairi¹, Ali Gharsallah¹, Abdelhafidh Gharbi¹,
and Henri Baudrand²

¹ Department of Physics
University of Sciences El Manar 2092 Tunisia
ibnelhajt@yahoo.fr, hassen.zairi@gmail.com, ali.gharsallah@gmail.com,
abdel.gharbi@fst.rnu.tn

² LAPLACE-GRE
2 rue Camichel 31000, Toulouse, France
henri.baudrand@yahoo.fr

Abstract — An iterative method based on the multiscale approach named multiscale wave concept iterative process (MWCIP) is introduced in this paper. This new approach is an extension of the known wave concept iterative process (WCIP). The specificity of the MWCIP method is the non-uniform meshing with macropixels used to improve the time delay computations of the classical iterative procedure. The method is applied successfully to a nondegenerate dual-mode microstrip patch filter. Comparison between the new and classical iterative methods shows that with the presented approach the CPU time and memory requirement have been considerably reduced.

Index Terms — Macropixel, microstrip patch filter, multiscale wave concept iterative process (MWCIP), wave concept iterative process (WCIP).

I. INTRODUCTION

Nowadays, the development of the microwaves domain is accompanied by an increase of the complexity of the circuits with requirement of prohibitive computation time and memory storage. In order to solve these problems, the researches, using multiresolution methods, focus on the multiscale concept appearing in different microwave fields since 1981 by Kunz and Simpson [1] with their

"expansion technique" and, also, by Kim and Hofer in 1990 [2].

Recently, these methods have been used to investigate microstrip circuits in order to employ different meshes as function of the complexity of these features. The different numerical approaches (FEM, FDFD, TLM...) are the subject of very significant evolutions in this field using adaptive grids [3, 4].

For instance, in the moment method, an adaptive multiscale moment method (AMMM) was introduced in 1998 by Su and Sarkar and applied to large diffracted structures with small cavities [5].

In addition, multi-grid approaches based on the wave concept iterative process (WCIP) method, developed by H. Baudrand in 1995 [6], were investigated. In [7], the non-uniform cells are substituted by their equivalent impedances and reintroduced into the coarse grid.

In [8], the authors studied separately the refined mesh parts of the whole structure and introduced the spectral connection to reduce the calculation time. This approach presents some difficulties especially with complex circuits.

In this paper, an original multiscale approach is proposed. It consists in introducing a new meshing grid without extracting the studied zones from the structure. The developed technique is based on the WCIP method. A program in FORTRAN has been elaborated to validate our multiscale approach. It was successfully applied to microstrip

transmission line and bandpass filter with a considerable reduction of the computation time.

II. WCIP FORMULATION

The WCIP method was explained in detail in different published articles [9-12]. Therefore, in this section, the general formulation is introduced. This method is a full wave method based on transverse wave formulation. The wave concept is described by writing the transverse electric and current density fields, respectively, E_i and J_i , on the interface Ω , in terms of incident and reflected waves A_i and B_i , respectively. It leads to the following set of equations:

$$\begin{cases} A_i = \frac{1}{2\sqrt{Z_{0i}}} (E_i + Z_{0i}J_i) \\ B_i = \frac{1}{2\sqrt{Z_{0i}}} (E_i - Z_{0i}J_i) \end{cases}, \quad (1)$$

where Z_{0i} is the characteristic impedance of the i th medium ($i=1,2$) [9].

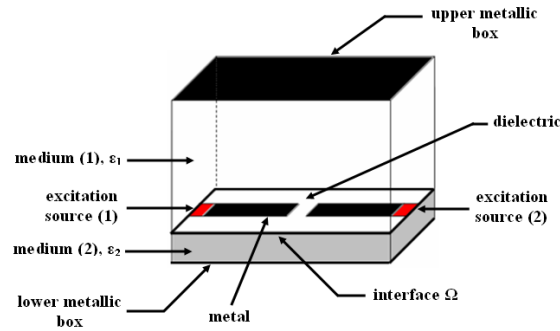


Fig. 1. Configuration of planar circuit structure in the waveguide box.

The air-dielectric interface Ω is divided into pixels and characterized by scattering operation matrix, depending on boundary conditions required on three sub-domains corresponding to metal, dielectric and excitation source shown in Fig. 1. The structure is excited by a planar electric source which generates two waves on both sides of the interface Ω .

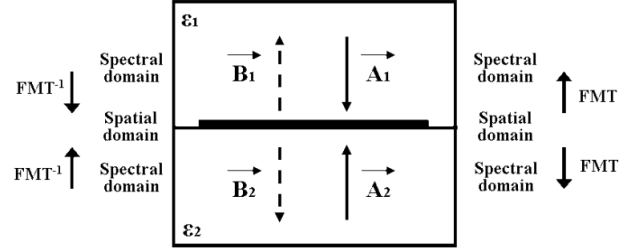


Fig. 2. Illustration of waves on both sides of the interface Ω .

Two operators establish the relations between these waves as follows: the scattering operator \hat{S} , related to the spatial domain, links the waves relative to the two different media separated by the surface Ω as shown in Fig. 2.

$$\vec{A}_i = \hat{S} \vec{B}_i + \vec{A}_{0i} \quad (3)$$

The reflection operator $\hat{\Gamma}$, related to the spectral domain, links the incident and reflected waves relative to the corresponding medium as:

$$\vec{B}_i = \hat{\Gamma} \vec{A}_i \quad (4)$$

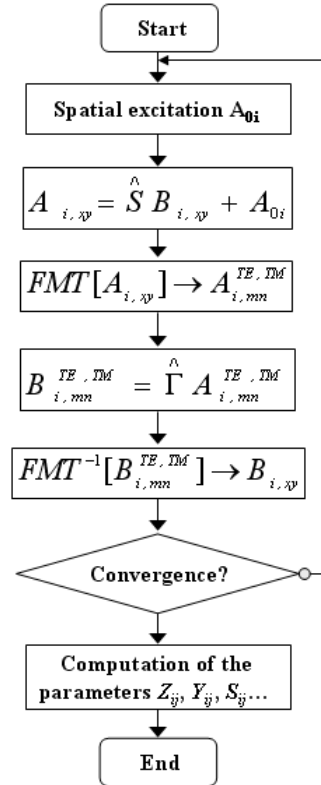


Fig. 3. Schematic description of the classical iterative process.

The implementation of the iterative process consists in establishing a recursive relationship between the waves in both media by using the reflection and scattering operators [9].

A fast modal transform (FMT) and its inverse (FMT⁻¹), based on a fast Fourier transform (FFT), allow the toggling between the spectral and spatial domains given by Fig. 2.

At the n^{th} iteration, the transverse electric and current density fields on the interface Ω are computed. Then, we can calculate the impedance, admittance, and scattering parameters Z_{ij} , Y_{ij} , and S_{ij} respectively, deduced from the following expression:

$$[S] = [1 - [Y]] [1 + [Y]]^{-1}. \quad (5)$$

The successive iterations are established to determine the relationship between $(A_i, B_i)^{n-1}$ and $(A_i, B_i)^n$ corresponding to the $(n-1)^{\text{th}}$ and n^{th} iteration. The iterative process continues until reaching the convergence of E_i and J_i fields calculated from (1) and (2) equations above. A schematic description of the classical WCIP algorithm is illustrated in Fig. 3.

III. MULTISCALE APPROACH

A. Coupling between two macropixels

In this part, the coupling between two consecutive macropixels of the grid is realised only by the “fundamental modes” which are the slightly attenuated modes. So, the high-order modes are localized on their macropixels. The coupling between two high-order modes can be neglected if it is smaller than a ten percent of the coupling between fundamental modes [13]. The fundamental and high-order modes are defined as transverse electric field of a waveguide bounded by periodic walls.

B. Definition of a new meshing grid

The contribution introduced, in this paper, consists in considering non-uniform meshing but with the classical iterative method where all cells have the same surface. In the spatial domain of the improved method, the whole structure is divided

into macropixels which are subdivided into pixels as function of the necessary precision. This new meshing grid is shown in Fig. 4.

The choice of this improved meshing grid should appear a maximum number of uniform macropixels where the scattering operator \hat{S} is constant (-1 for metal and 1 for dielectric). So the computation time is reduced significantly because its calculation became useless.

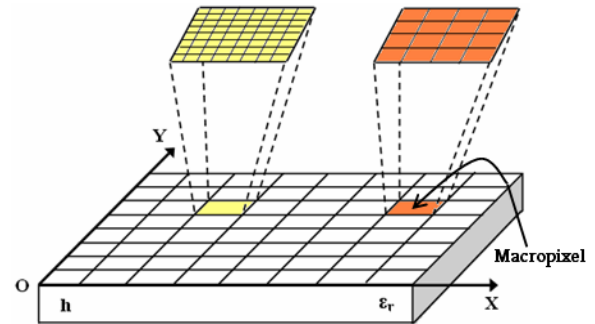


Fig. 4. The new meshing grid.

The whole structure is meshed with $N_1 \times N_2$ pixels in classical iterative method. But, in the improved WCIP method, it is meshed with $N_{01} \times N_{02}$ macropixels where each one is divided into $n_{01}^{\alpha\beta} \times n_{02}^{\alpha\beta}$ pixels as shown in Fig. 5. The indexes α and β represent the position of the considered macropixel in the new meshing grid where:

α is the macropixel position in the X-direction.

β is the macropixel position in the Y-direction.

The number of operations decreases with this new meshing from $[N_1 \times N_2 \times \ln(N_1 \times N_2)]$ to $[N_{01} \times N_{02} \times \ln(N_{01} \times N_{02}) + n_{01}^{\alpha\beta} \times n_{02}^{\alpha\beta} \times \ln(n_{01}^{\alpha\beta} \times n_{02}^{\alpha\beta})]$ and it can be reduced more in the presence of uniform macropixels considering that $(N_1 \times N_2) \gg (N_{01} \times N_{02})$.

This reduction is significant especially when complex structures, requiring an important resolution, are investigated. Therefore, it avoids an excessive computational storage and simulation times for bulky devices.

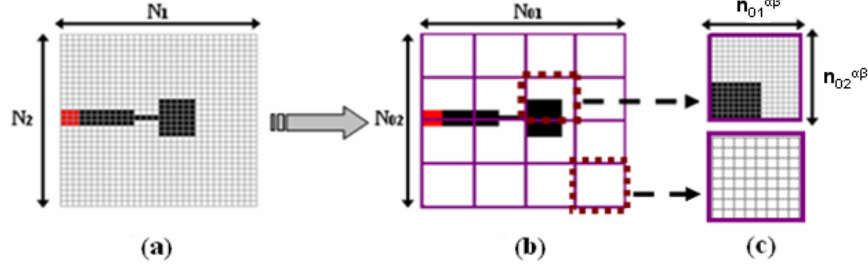


Fig. 5. (a) Classical WCIP meshing, (b) whole structure's meshing in MWCIP, (c) uniform and non-uniform macropixels meshing.

C. Multiscale wave concept iterative process (MWCIP)

In this section, the improved iterative method named multiscale wave concept iterative process (MWCIP) is described.

For each iteration, the fundamental modes $A_{ix,y}^{\alpha\beta}$ relative to the (α,β) macropixel are computed as follows:

$$A_{i,xy}^{\alpha\beta} = \frac{1}{k^{\alpha\beta}} \sum_{M=1}^{k^{\alpha\beta}} a_{i,xy}^{\alpha\beta M} e^{j\left(\frac{2\pi p}{a}x + \frac{2\pi q}{b}y\right)}, \quad (6)$$

where

$$k^{\alpha\beta} = n_{01}^{\alpha\beta} \times n_{02}^{\alpha\beta}.$$

a and b are the (α,β) macropixel's dimensions.

Then, they are extracted from the reflected waves $a_{ix,y}^{\alpha\beta}$ to give the high-order ones $a'_{ix,y}^{\alpha\beta}$.

To toggle to the spectral domain, a FMT is applied either to the fundamental modes or the high-order ones. After multiplying the modes' amplitudes $a'_{i,mn}{}^{TE, TM \alpha\beta}$ by the corresponding reflection operators $\hat{\Gamma}_i^{\alpha\beta}$, a FMT⁻¹ allows to return to the spatial domain where the incident waves $B_{ix,y}$ and $b'_{ix,y}^{\alpha\beta}$ are recombined.

In order to calculate the amplitudes of the reflected waves relative to the next iteration, the scattering operators $\hat{S}^{\alpha\beta}$ relative to each macropixel are introduced.

In the same way, the iterative process of the improved scheme, depicted in Fig. 6, continues until reaching the convergence of the transverse electric E_i and current density J_i fields.

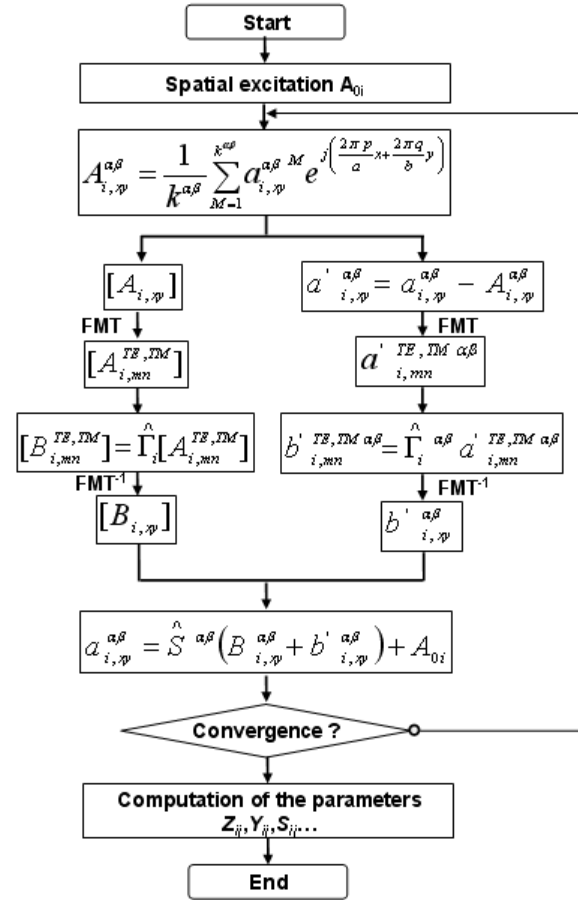


Fig. 6. Schematic description of the MWCIP.

IV. APPLICATIONS

A. Microstrip transmission line

To validate our new multiscale approach, a microstrip transmission line was studied. It is characterized by its length $L=21.0$ mm and its width $w=4.0$ mm. The substrate dielectric parameters are fixed with $h=1.0$ mm and $\epsilon_r=9.6$. The waveguide box parameters are $W=8.0$ mm

and $H=4.0$ mm. Fig. 7 shows the layout of the investigated structure.

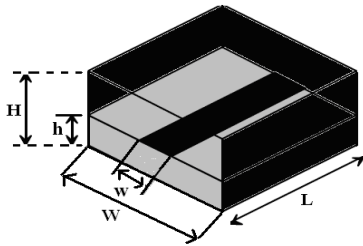


Fig. 7. Layout of the microstrip transmission line.

If the length of this transmission line is $L=\lambda/2$, the corresponding theoretic resonant frequency would be:

$$f_{res} = \frac{C}{2 \times L \times \sqrt{\epsilon_r}} = 2.3\text{GHz} \quad (7)$$

where λ is the wavelength and C is the velocity of electromagnetic wave in free space.

The convergence of the return loss coefficient S_{11} was reached at the 150th iteration as shown in Fig. 8.

The input impedance imaginary part against frequency is simulated. The comparison between the WCIP and the MWCIP results, illustrated by Fig. 9, shows a good agreement. It can also confirm the theoretical resonant frequency calculated.

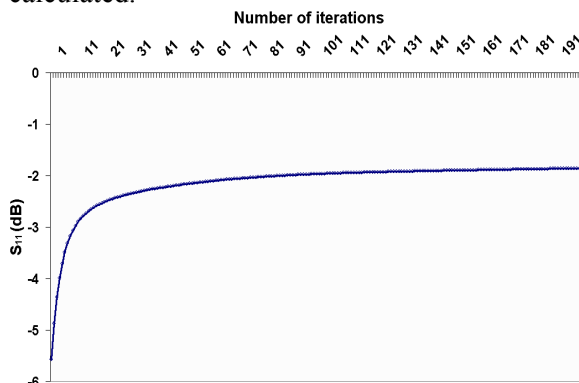


Fig. 8. The convergence of the return loss S_{11} .

In the WCIP method, 64×16 pixels are used corresponding to $N_1 \times N_2$ pixels. However, in our improved method MWCIP, 8×2 macropixels are used corresponding to $N_{01} \times N_{02}$ resolution. Each one is subdivided into 8×8 pixels corresponding to $n_{01}^{ab} \times n_{02}^{ab}$ resolution.

The number of operations is reduced more than three times, from 7100 operations with the classical WCIP method to 2174 operations with the improved one.

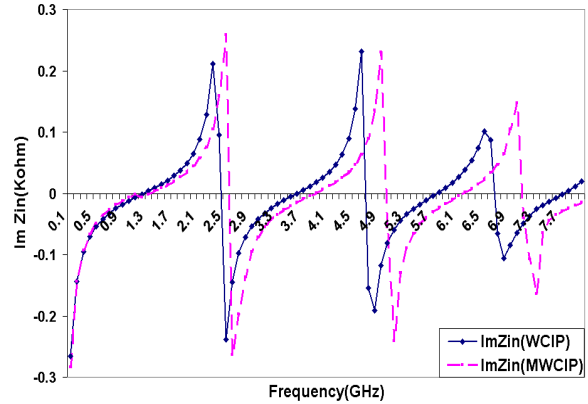


Fig. 9. Simulation of the input impedance imaginary part against frequency.

B. Dual-mode bandpass filter

After validating our new approach for a simple structure, a nondegenerate dual-mode microstrip patch filter is investigated. The proposed filter is based on a square microstrip patch with four symmetrically etched slots as shown in Fig. 10.

The square patch has a length of $W=17.0$ mm, while the slots have equal lengths $L=6.0$ mm and widths $S=1.0$ mm. It is excited with asymmetric direct-feed 50Ω microstrip lines of 1.0 mm length at the corners, as shown in the patch filter's layout. The studied filter is developed on duroid material with $\epsilon_r=10.2$ and 0.635 mm thickness [14].

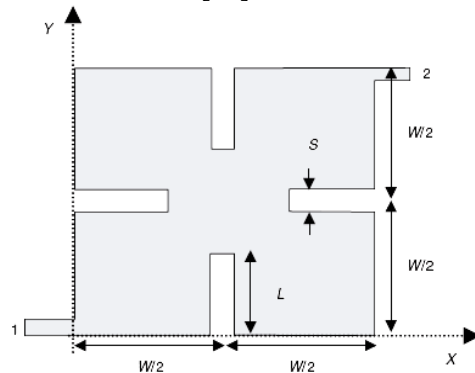


Fig. 10. Layout of the dual-mode bandpass filter.

The MWCIP is applied to this structure in order to simulate the return loss against

frequency for two different values of the slot length ($L=4.0$ mm and $L=6.0$ mm) and the same width $S=1.0$ mm. The results shown in Fig. 11 confirm the effect of the slot length on the investigated filter; when L increases the filter behavior shifts to lower frequencies and the bandwidth becomes narrower [14].

Good agreement between simulated results given by our new approach and the IE3D simulator is observed particularly for $L=6.0$ mm. It confirms the accuracy of the MWCIP method.

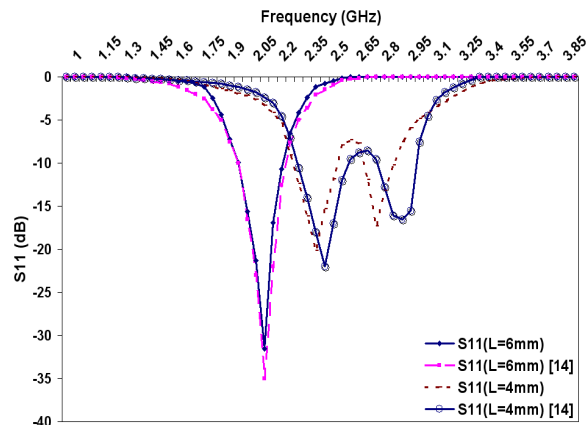


Fig. 11. Comparison of the simulated returns loss against frequency between MWCIP and [14] for two slot lengths.

For this simulation, 4×4 macropixels are subdivided to 16×16 pixels each one as shown in Fig. 12. The total computation time was 17mn 12s for 60 frequency points (17.2s per frequency point).

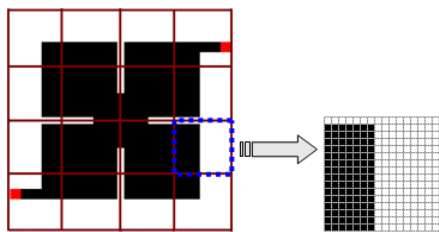


Fig. 12. Meshing applied to the bandpass filter in MWCIP method.

A wider bandwidth is investigated using the WCIP and MWCIP methods in order to compare their results with the simulated and measured ones [14] shown by Fig. 13 that reveals a good agreement. Four resonant

frequencies and a better rejection are observed.

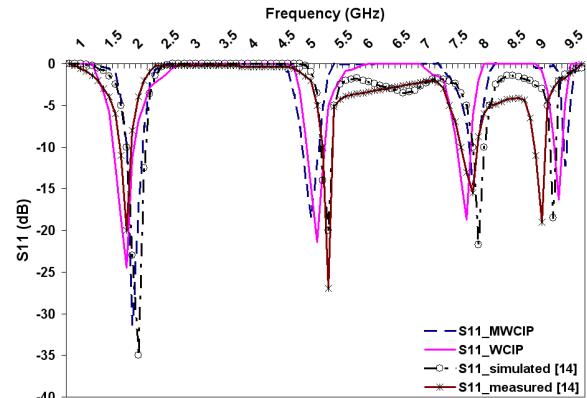


Fig. 13. Simulated return loss against frequency.

Table1: Comparison of the CPU time between WCIP and MWCIP methods

	WCIP	MWCIP
Pixel number	128×128	8×8 macropixels + 16×16 (for each macropixel)
Iteration number	300	300
Computation time	1h 16mn 37s	45mn 33s
1 iteration CPU time	51s	30.48s
Operatio N number	159×10^3	91119

The computation time and the number of operations between the classical iterative method and the improved one are criticized.

The table shows that the CPU time computation is reduced for the same number of iterations. Also, the number of operations decreases from 159×10^3 to 91119 with the MWCIP which gives a ratio of 1.75.

V. CONCLUSION

The formulation of the multiscale iterative method was described. The computation time and the requirements in data-processing memory were considerably reduced in relation to the classical WCIP. The results obtained with the two investigated circuits prove the

efficiency of our approach and its agreement with the published ones.

Consequently, the present approach will be studied for further new applications and its performances will have to be improved.

REFERENCES

- [1] K. S. Kunz and L. Simpson, "A technique for increasing the resolution of finite-difference solution of the Maxwell equation," *IEEE transaction on Electromagnetic Compatibility*, vol. EMC-23, pp. 419-422, Nov. 1981.
- [2] I. S. Kim and W. J. R. Hofer, "A local mesh refinement algorithm for the time-domain finite-difference method using Maxwell's curl equations," *IEEE Trans. Microwave Theory Tech.*, vol. 38, no. 6, pp. 812-815, Jun. 1990.
- [3] M. H. Al Sharkawy, V. Demir, and A. Z. Elsherbeni, "Plane Wave Scattering From Three Dimensional Multiple Objects Using the Iterative Multiregion Technique Based on the FDFD Method," *IEEE Trans.on Ant. And Prop.*, vol. 54, no. 2, pp. 666-673, Feb. 2006.
- [4] P. Sewell, A. Vukovic, TM. Benson, C. Christopoulos, DWP Thomas, and AI. Nosich, "Analytic coupling of spatially distinct unstructured TLM meshes," *11^{eme} Int. Conf on Mathematical Methods in Electromagnetic Theory*, pp. 89-94, Jun. 26-29, 2006.
- [5] C. Su and T. K. Starker, "Electromagnetic Scattering from Two-dimensional Electrically Large Perfectly Conducting Objects with Small Cavities and Humps by Use of Adaptive Multistage Moment Method (AMMM)," *J. Electromagnet. Waves Appl.*, vol. 12, pp 885-906, 1998.
- [6] M. Azizi, H. Aubert, H. Baudrand and M. Boussois, "Une méthode itérative originale pour la résolution des problèmes de diffraction électromagnétique," 13th Meeting Hertzian Optics and Dielectrics - OHD' 95, pp. 228 - 231, Sept. 1995.
- [7] H. Zairi, A. Gharsallah, A. Gharbi, and H. Baudrand, "Analysis of planar circuits using a multi-grid iterative method," *IEE Proceedings - Microwaves, Antennas and Propagation*, vol. 153, no. 3, pp. 231-236, Jun. 2006.
- [8] N. Raveu, O. Pigaglio, G. Prigent, and H. Baudrand, "Improvement in the Wave Concept Iterative Procedure through Spectral connection," *IEEE European Microwave Conference (EuMC)*, Munich, Oct. 2007.
- [9] A. Gharsallah, A. Gharbi, and H. Baudrand, "Efficient Analysis of Multiport Circuits Using the Iterative Technique," *Electromagnetics*, vol. 21, pp. 73-84, 2001.
- [10] M. Titaouine, A. Gomes Neto, H. Baudrand, and F.Djahli, "Analysis of shorted ring slots frequency selective surfaces using WCIP method," *Journal of Microwaves, Optoelectronics and Electromagnetic Applications*, vol. 7, no. 2, Dec. 2008.
- [11] N. Raveu, T. P. Vuong, I. Terrasse, G. Piau, and H. Baudrand, "Analysis of cylindrically conformal microstrip structure using an iterative method," *Progress in Electromagnetics Research*, vol. 87, pp. 215-231, 2008.
- [12] A. Gharsallah, R. Garcia, A. Gharbi, and H. Baudrand, "Wave concept iterative process merges with modal fast Fourier transformation to analyze microstrip filters," *The Applied Computational Electromagnetics Society*, vol. 16, no. 1, 2001.
- [13] F. Surre, L. Cohen, H. Baudrand, and J. C. Peuch, "New approaches for multi-scale circuit analysis," *European Microwave Conference*, Sep. 2001.
- [14] A. F. Sheta, N. Dib, and A. Mohra, "Investigation of new nondegenerate dual-mode microstrip patch filter," *IEE Proc.-Microw. Antennas Propag.*, vol. 153, no. 1, Feb. 2006.



Taoufik Ibn Elhaj Brahim

received his master's degree in electronics from the Faculty of Sciences, Tunis, Tunisia in 2007. He is currently working toward his Ph.D. degree at the faculty of Sciences, Tunis.

His research interests include antenna for wireless communication and microwave integrated circuits.



Hassen Zairi

received his master's degree in physics from the Faculty of Sciences, Tunis, Tunisia in 2002. He is currently working toward his Ph.D. degree at the Faculty of Sciences, Tunis.

His research interests include antenna for wireless communication and microwave integrated circuits.



Ali Gharsallah Professor in the Faculty of Sciences, Tunis. He is responsible for the Circuits and systems Electronics HF unity in the same university. He has received his degrees in radio-

electrical engineering from the Superior Institut of telecommunication, Tunis in 1986 and the Ph.D. degree in 1994 from the Ecole National d'Ingénieurs, Tunis. Since 1991, he was with the department of Physics at the Faculty of Sciences, Tunis. His current research interests include antennas, multilayered structures, and microwave integrated circuits.



Abdelhafidh Gharbi Professor in the Faculty of Sciences, Tunis. He is responsible for the LPMM laboratory in the same university.

His current research interests are in the dielectric and electromagnetic fields.



Henri Baudrand Professor of Electromagnetism and microwave circuits at the Ecole Nationale Supérieure d'Electronique Electrotechnique Informatique of Toulouse,

France. He is specialized in modelization of passive and active circuits and antennas. He is the author and co-author of three books:

- Introduction au calcul des éléments de circuits microondes
- Optimisation des circuits non linéaires
- Calcul des circuits microondes par les schémas équivalents-exercices CEPADUES Editions).

He is a member of the 'Electromagnetism Academy', senior member of IEE societies. President of URSI France commission B for 6 years (1993-1999), member and past president of IEEE-MTT-ED French chapter. He is an awarded officier of Palmes académiques, and Director Honoris causa of Iasi University. He is the Director of GREMO (Groupe de Recherche en Electromagnétisme et Microondes de Toulouse).

2010 INSTITUTIONAL MEMBERS

DTIC-OCP LIBRARY
8725 John J. Kingman Rd, Ste 0944
Fort Belvoir, VA 22060-6218

AUSTRALIAN DEFENCE LIBRARY
Northcott Drive
Canberra, A.C.T. 2600 Australia

BEIJING BOOK CO, INC
701 E Linden Avenue
Linden, NJ 07036-2495

BUCKNELL UNIVERSITY
69 Coleman Hall Road
Lewisburg, PA 17837

ROBERT J. BURKHOLDER
OHIO STATE UNIVERSITY
1320 Kinnear Road
Columbus, OH 43212

DARTMOUTH COLLEGE
6025 Baker/Berry Library
Hanover, NH 03755-3560

DSTO EDINBURGH
AU/33851-AP, PO Box 830470
Birmingham, AL 35283

SIMEON J. EARL – BAE SYSTEMS
W432A, Warton Aerodome
Preston, Lancs., UK PR4 1AX

ELLEDIEMME
Libri Dal Mondo
PO Box 69/Poste S. Silvestro
Rome, Italy 00187

ENGINEERING INFORMATION, INC
PO Box 543
Amsterdam, Netherlands 1000 Am

ETSE TELECOMUNICACION
Biblioteca, Campus Lagoas
Vigo, 36200 Spain

OLA FORSLUND
SAAB MICROWAVE SYSTEMS
Nettovagen 6
Jarfalla, Sweden SE-17588

GEORGIA TECH LIBRARY
225 North Avenue, NW
Atlanta, GA 30332-0001

HRL LABS, RESEARCH LIBRARY
3011 Malibu Canyon
Malibu, CA 90265

IEE INSPEC
Michael Faraday House
6 Hills Way
Stevenage, Herts UK SG1 2AY

IND CANTABRIA
PO Box 830470
Birmingham, AL 35283

INSTITUTE FOR SCIENTIFIC INFO.
Publication Processing Dept.
3501 Market St.
Philadelphia, PA 19104-3302

KUWAIT UNIVERSITY
Postfach/po box 432
Basel, Switzerland 4900

LIBRARY – DRDC OTTAWA
3701 Carling Avenue
Ottawa, Ontario, Canada K1A 0Z4

LIBRARY of CONGRESS
Reg. Of Copyrights
Attn: 407 Deposits
Washington DC, 20559

LINDA HALL LIBRARY
5109 Cherry Street
Kansas City, MO 64110-2498

RAY MCKENZIE – TELESTRA
13/242 Exhibition Street
Melbourne, Vic, Australia 3000

MISSISSIPPI STATE UNIV LIBRARY
PO Box 9570
Mississippi State, MS 39762

MISSOURI S&T
400 W 14th Street
Rolla, MO 64609

MIT LINCOLN LABORATORY
Periodicals Library
244 Wood Street
Lexington, MA 02420

OSAMA MOHAMMED
FLORIDA INTERNATIONAL UNIV
10555 W Flagler Street
Miami, FL 33174

NAVAL POSTGRADUATE SCHOOL
Attn: J. Rozdal/411 Dyer Rd./ Rm 111
Monterey, CA 93943-5101

NDL KAGAKU
C/O KWE-ACCESS
PO Box 300613 (JFK A/P)
Jamaica, NY 11430-0613

OVIEDO LIBRARY
PO BOX 830679
Birmingham, AL 35283

PENN STATE UNIVERSITY
126 Paterno Library
University Park, PA 16802-1808

DAVID J. PINION
1122 E PIKE STREET #1217
SEATTLE, WA 98122

KATHERINE SIAKAVARA -
ARISTOTLE UNIV OF
THESSALONIKI
Gymnasiou 8
Thessaloniki, Greece 55236

SWETS INFORMATION SERVICES
160 Ninth Avenue, Suite A
Runnemede, NJ 08078

TIB & UNIV. BIB. HANNOVER
DE/5100/G1/0001
Welfengarten 1B
Hannover, Germany 30167

UNIV OF CENTRAL FLORIDA
4000 Central Florida Boulevard
Orlando, FL 32816-8005

UNIVERSITY OF COLORADO
1720 Pleasant Street, 184 UCB
Boulder, CO 80309-0184

UNIVERSITY OF KANSAS –
WATSON
1425 Jayhawk Blvd 210S
Lawrence, KS 66045-7594

UNIVERSITY OF MISSISSIPPI
JD Williams Library
University, MS 38677-1848

UNIVERSITY LIBRARY/HKUST
CLEAR WATER BAY ROAD
KOWLOON, HONG KONG

UNIV POLIT CARTAGENA
Serv Btca Univ,
Paseo Alfonso XIII, 48
Cartagena, Spain 30203

THOMAS WEILAND
TU DARMSTADT
Schlossgartenstrasse 8
Darmstadt, Hessen, Germany 64289

STEVEN WEISS
US ARMY RESEARCH LAB
2800 Powder Mill Road
Adelphi, MD 20783

YOSHIHIDE YAMADA
NATIONAL DEFENSE ACADEMY
1-10-20 Hashirimizu
Yokosuka, Kanagawa,
Japan 239-8686

ACES COPYRIGHT FORM

This form is intended for original, previously unpublished manuscripts submitted to ACES periodicals and conference publications. The signed form, appropriately completed, MUST ACCOMPANY any paper in order to be published by ACES. PLEASE READ REVERSE SIDE OF THIS FORM FOR FURTHER DETAILS.

TITLE OF PAPER:

RETURN FORM TO:

Dr. Atef Z. Elsherbeni
University of Mississippi
Dept. of Electrical Engineering
Anderson Hall Box 13
University, MS 38677 USA

AUTHORS(S)

PUBLICATION TITLE/DATE:

PART A - COPYRIGHT TRANSFER FORM

(NOTE: Company or other forms may not be substituted for this form. U.S. Government employees whose work is not subject to copyright may so certify by signing Part B below. Authors whose work is subject to Crown Copyright may sign Part C overleaf).

The undersigned, desiring to publish the above paper in a publication of ACES, hereby transfer their copyrights in the above paper to The Applied Computational Electromagnetics Society (ACES). The undersigned hereby represents and warrants that the paper is original and that he/she is the author of the paper or otherwise has the power and authority to make and execute this assignment.

Returned Rights: In return for these rights, ACES hereby grants to the above authors, and the employers for whom the work was performed, royalty-free permission to:

1. Retain all proprietary rights other than copyright, such as patent rights.
2. Reuse all or portions of the above paper in other works.

3. Reproduce, or have reproduced, the above paper for the author's personal use or for internal company use provided that (a) the source and ACES copyright are indicated, (b) the copies are not used in a way that implies ACES endorsement of a product or service of an employer, and (c) the copies per se are not offered for sale.

4. Make limited distribution of all or portions of the above paper prior to publication.

5. In the case of work performed under U.S. Government contract, ACES grants the U.S. Government royalty-free permission to reproduce all or portions of the above paper, and to authorize others to do so, for U.S. Government purposes only.

ACES Obligations: In exercising its rights under copyright, ACES will make all reasonable efforts to act in the interests of the authors and employers as well as in its own interest. In particular, ACES REQUIRES that:

1. The consent of the first-named author be sought as a condition in granting re-publication permission to others.
2. The consent of the undersigned employer be obtained as a condition in granting permission to others to reuse all or portions of the paper for promotion or marketing purposes.

In the event the above paper is not accepted and published by ACES or is withdrawn by the author(s) before acceptance by ACES, this agreement becomes null and void.

AUTHORIZED SIGNATURE

TITLE (IF NOT AUTHOR)

EMPLOYER FOR WHOM WORK WAS PERFORMED

DATE FORM SIGNED

Part B - U.S. GOVERNMENT EMPLOYEE CERTIFICATION

(NOTE: if your work was performed under Government contract but you are not a Government employee, sign transfer form above and see item 5 under Returned Rights).

This certifies that all authors of the above paper are employees of the U.S. Government and performed this work as part of their employment and that the paper is therefor not subject to U.S. copyright protection.

AUTHORIZED SIGNATURE

TITLE (IF NOT AUTHOR)

NAME OF GOVERNMENT ORGANIZATION

DATE FORM SIGNED

PART C - CROWN COPYRIGHT

(NOTE: ACES recognizes and will honor Crown Copyright as it does U.S. Copyright. It is understood that, in asserting Crown Copyright, ACES in no way diminishes its rights as publisher. Sign only if *ALL* authors are subject to Crown Copyright).

This certifies that all authors of the above Paper are subject to Crown Copyright. (Appropriate documentation and instructions regarding form of Crown Copyright notice may be attached).

AUTHORIZED SIGNATURE

TITLE OF SIGNEE

NAME OF GOVERNMENT BRANCH

DATE FORM SIGNED

Information to Authors

ACES POLICY

ACES distributes its technical publications throughout the world, and it may be necessary to translate and abstract its publications, and articles contained therein, for inclusion in various compendiums and similar publications, etc. When an article is submitted for publication by ACES, acceptance of the article implies that ACES has the rights to do all of the things it normally does with such an article.

In connection with its publishing activities, it is the policy of ACES to own the copyrights in its technical publications, and to the contributions contained therein, in order to protect the interests of ACES, its authors and their employers, and at the same time to facilitate the appropriate re-use of this material by others.

The new United States copyright law requires that the transfer of copyrights in each contribution from the author to ACES be confirmed in writing. It is therefore necessary that you execute either Part A-Copyright Transfer Form or Part B-U.S. Government Employee Certification or Part C-Crown Copyright on this sheet and return it to the Managing Editor (or person who supplied this sheet) as promptly as possible.

CLEARANCE OF PAPERS

ACES must of necessity assume that materials presented at its meetings or submitted to its publications is properly available for general dissemination to the audiences these activities are organized to serve. It is the responsibility of the authors, not ACES, to determine whether disclosure of their material requires the prior consent of other parties and if so, to obtain it. Furthermore, ACES must assume that, if an author uses within his/her article previously published and/or copyrighted material that permission has been obtained for such use and that any required credit lines, copyright notices, etc. are duly noted.

AUTHOR/COMPANY RIGHTS

If you are employed and you prepared your paper as a part of your job, the rights to your paper initially rest with your employer. In that case, when you sign the copyright form, we assume you are authorized to do so by your employer and that your employer has consented to all of the terms and conditions of this form. If not, it should be signed by someone so authorized.

NOTE RE RETURNED RIGHTS: Just as ACES now requires a signed copyright transfer form in order to do "business as usual", it is the intent of this form to return rights to the author and employer so that they too may do "business as usual". If further clarification is required, please contact: The Managing Editor, R. W. Adler, Naval Postgraduate School, Code EC/AB, Monterey, CA, 93943, USA (408)656-2352.

Please note that, although authors are permitted to re-use all or portions of their ACES copyrighted material in other works, this does not include granting third party requests for reprinting, republishing, or other types of re-use.

JOINT AUTHORSHIP

For jointly authored papers, only one signature is required, but we assume all authors have been advised and have consented to the terms of this form.

U.S. GOVERNMENT EMPLOYEES

Authors who are U.S. Government employees are not required to sign the Copyright Transfer Form (Part A), but any co-authors outside the Government are.

Part B of the form is to be used instead of Part A only if all authors are U.S. Government employees and prepared the paper as part of their job.

NOTE RE GOVERNMENT CONTRACT WORK: Authors whose work was performed under a U.S. Government contract but who are not Government employees are required so sign Part A-Copyright Transfer Form. However, item 5 of the form returns reproduction rights to the U. S. Government when required, even though ACES copyright policy is in effect with respect to the reuse of material by the general public.

January 2002

INFORMATION FOR AUTHORS

PUBLICATION CRITERIA

Each paper is required to manifest some relation to applied computational electromagnetics. **Papers may address general issues in applied computational electromagnetics, or they may focus on specific applications, techniques, codes, or computational issues.** While the following list is not exhaustive, each paper will generally relate to at least one of these areas:

- 1. Code validation.** This is done using internal checks or experimental, analytical or other computational data. Measured data of potential utility to code validation efforts will also be considered for publication.
- 2. Code performance analysis.** This usually involves identification of numerical accuracy or other limitations, solution convergence, numerical and physical modeling error, and parameter tradeoffs. However, it is also permissible to address issues such as ease-of-use, set-up time, run time, special outputs, or other special features.
- 3. Computational studies of basic physics.** This involves using a code, algorithm, or computational technique to simulate reality in such a way that better, or new physical insight or understanding, is achieved.
- 4. New computational techniques** or new applications for existing computational techniques or codes.
- 5. “Tricks of the trade”** in selecting and applying codes and techniques.
- 6. New codes, algorithms, code enhancement, and code fixes.** This category is self-explanatory, but includes significant changes to existing codes, such as applicability extensions, algorithm optimization, problem correction, limitation removal, or other performance improvement. **Note: Code (or algorithm) capability descriptions are not acceptable, unless they contain sufficient technical material to justify consideration.**
- 7. Code input/output issues.** This normally involves innovations in input (such as input geometry standardization, automatic mesh generation, or computer-aided design) or in output (whether it be tabular, graphical, statistical, Fourier-transformed, or otherwise signal-processed). Material dealing with input/output database management, output interpretation, or other input/output issues will also be considered for publication.
- 8. Computer hardware issues.** This is the category for analysis of hardware capabilities and limitations of various types of electromagnetics computational requirements. Vector and parallel computational techniques and implementation are of particular interest.

Applications of interest include, but are not limited to, antennas (and their electromagnetic environments), networks, static fields, radar cross section, inverse scattering, shielding, radiation hazards, biological effects, biomedical applications, electromagnetic pulse (EMP), electromagnetic interference (EMI), electromagnetic compatibility (EMC), power transmission, charge transport, dielectric, magnetic and nonlinear materials, microwave components, MEMS, RFID, and MMIC technologies, remote sensing and geometrical and physical optics, radar and communications systems, sensors, fiber optics, plasmas, particle accelerators, generators and motors, electromagnetic wave propagation, non-destructive evaluation, eddy currents, and inverse scattering.

Techniques of interest include but not limited to frequency-domain and time-domain techniques, integral equation and differential equation techniques, diffraction theories, physical and geometrical optics, method of moments, finite differences and finite element techniques, transmission line method, modal expansions, perturbation methods, and hybrid methods.

Where possible and appropriate, authors are required to provide statements of quantitative accuracy for measured and/or computed data. This issue is discussed in “Accuracy & Publication: Requiring, quantitative accuracy statements to accompany data,” by E. K. Miller, *ACES Newsletter*, Vol. 9, No. 3, pp. 23-29, 1994, ISBN 1056-9170.

SUBMITTAL PROCEDURE

All submissions should be uploaded to ACES server through ACES web site (<http://aces.ee.olemiss.edu>) by using the upload button, journal section. Only pdf files are accepted for submission. The file size should not be larger than 5MB, otherwise permission from the Editor-in-Chief should be obtained first. Automated acknowledgment of the electronic submission, after the upload process is successfully completed, will be sent to the corresponding author only. It is the responsibility of the corresponding author to keep the remaining authors, if applicable, informed. Email submission is not accepted and will not be processed.

PAPER FORMAT (INITIAL SUBMISSION)

The preferred format for initial submission manuscripts is 12 point Times Roman font, single line spacing and single column format, with 1 inch for top, bottom, left, and right margins. Manuscripts should be prepared for standard 8.5x11 inch paper.

EDITORIAL REVIEW

In order to ensure an appropriate level of quality control, papers are peer reviewed. They are reviewed both for

technical correctness and for adherence to the listed guidelines regarding information content and format.

PAPER FORMAT (FINAL SUBMISSION)

Only camera-ready electronic files are accepted for publication. The term “**camera-ready**” means that the material is neat, legible, reproducible, and in accordance with the final version format listed below.

The following requirements are in effect for the final version of an ACES Journal paper:

1. The paper title should not be placed on a separate page. The title, author(s), abstract, and (space permitting) beginning of the paper itself should all be on the first page. The title, author(s), and author affiliations should be centered (center-justified) on the first page. The title should be of font size 16 and bolded, the author names should be of font size 12 and bolded, and the author affiliation should be of font size 12 (regular font, neither italic nor bolded).
2. An abstract is required. The abstract should be a brief summary of the work described in the paper. It should state the computer codes, computational techniques, and applications discussed in the paper (as applicable) and should otherwise be usable by technical abstracting and indexing services. The word “Abstract” has to be placed at the left margin of the paper, and should be bolded and italic. It also should be followed by a hyphen (–) with the main text of the abstract starting on the same line.
3. All section titles have to be centered and all the title letters should be written in caps. The section titles need to be numbered using roman numbering (I. II.)
4. Either British English or American English spellings may be used, provided that each word is spelled consistently throughout the paper.
5. Internal consistency of references format should be maintained. As a guideline for authors, we recommend that references be given using numerical numbering in the body of the paper (with numerical listing of all references at the end of the paper). The first letter of the authors’ first name should be listed followed by a period, which in turn, followed by the authors’ complete last name. Use a coma (,) to separate between the authors’ names. Titles of papers or articles should be in quotation marks (“ ”), followed by the title of journal, which should be in italic font. The journal volume (vol.), issue number (no.), page numbering (pp.), month and year of publication should come after the journal title in the sequence listed here.
6. Internal consistency shall also be maintained for other elements of style, such as equation numbering. As a guideline for authors who have no other preference, we suggest that equation numbers be placed in parentheses at the right column margin.

7. The intent and meaning of all text must be clear. For authors who are not masters of the English language, the ACES Editorial Staff will provide assistance with grammar (subject to clarity of intent and meaning). However, this may delay the scheduled publication date.
8. Unused space should be minimized. Sections and subsections should not normally begin on a new page.

ACES reserves the right to edit any uploaded material, however, this is not generally done. It is the author(s) responsibility to provide acceptable camera-ready pdf files. Incompatible or incomplete pdf files will not be processed for publication, and authors will be requested to re-upload a revised acceptable version.

COPYRIGHTS AND RELEASES

Each primary author must sign a copyright form and obtain a release from his/her organization vesting the copyright with ACES. Copyright forms are available at ACES, web site (<http://aces.ee.olemiss.edu>). To shorten the review process time, the executed copyright form should be forwarded to the Editor-in-Chief immediately after the completion of the upload (electronic submission) process. Both the author and his/her organization are allowed to use the copyrighted material freely for their own private purposes.

Permission is granted to quote short passages and reproduce figures and tables from an ACES Journal issue provided the source is cited. Copies of ACES Journal articles may be made in accordance with usage permitted by Sections 107 or 108 of the U.S. Copyright Law. This consent does not extend to other kinds of copying, such as for general distribution, for advertising or promotional purposes, for creating new collective works, or for resale. The reproduction of multiple copies and the use of articles or extracts for commercial purposes require the consent of the author and specific permission from ACES. Institutional members are allowed to copy any ACES Journal issue for their internal distribution only.

PUBLICATION CHARGES

All authors are allowed for 8 printed pages per paper without charge. Mandatory page charges of \$75 a page apply to all pages in excess of 8 printed pages. Authors are entitled to one, free of charge, copy of the journal issue in which their paper was published. Additional reprints are available for a nominal fee by submitting a request to the managing editor or ACES Secretary.

Authors are subject to fill out a one page over-page charge form and submit it online along with the copyright form before publication of their manuscript.

ACES Journal is abstracted in INSPEC, in Engineering Index, DTIC, Science Citation Index Expanded, the Research Alert, and to Current Contents/Engineering, Computing & Technology.